Evaluation of HVAF Thermal Sprayed NiCrMoW

Effect of HVAF thermal sprayed NiCrMoW coating thickness on HIC resistance of carbon steel in sour environment

TU Delft

Koen Winters

Effect of HVAF thermal sprayed NiCrMoW coating thickness on HIC resistance of carbon steels in sour environment

Thesis report

by

Koen Winters

to obtain the degree of Master of Science
at the Delft University of Technology
to be defended publicly on 25 September, 2023 at 13:00

Thesis committee:	
Supervisors:	Prof. Dr. Ir. J.M.C. Mol
	Dr. Ir. M.E Wilms
	Ir. F. van der Klift
External examiners:	Dr. Ir. V. Popovich
	Dr. Ir. P. Taheri
Place:	Faculty of Materials Science & Engineering, Delft
Project Duration:	September 2022 - September, 2023
Student number:	4475151

An electronic version of this thesis is available at `http://repository.tudelft.nl/`.

Faculty of Materials Science & Engineering · Delft University of Technology

Acknowledgements

This thesis is the final part of the master's programme in Materials Science & Engineering at the Delft University of Technology. This thesis not only marks the end of a journey towards becoming an independent academic, but it is also the start of a new journey.

First I would like to thank the thesis committee; Arjan Mol, thank you for supporting me to become a better researcher, your feedback on my work was always sharp and insightful. The meetings we had often provided me with new ideas and different perspectives on the thesis. I want to thank Marc Wilms for always making time to discuss the progress of my thesis. Your knowledge of the topic was invaluable during this year and provided me with new ways to approach my research. At last, I would like to thank Frank van der Klift, not only for introducing me to the beautiful world of corrosion in the oil % gas industry, but also for his support and feedback during the entire process.

My sincere gratitude also goes to my materials and corrosion engineering colleagues in Rotterdam, who participated in stimulating discussions and shared their expertise, creating a stimulating research environment. Furthermore, I would like to thank the RWTH Aachen for their support and patience during the collaboration. A special thanks goes to Richard Sterkman, for his assistance, collaborative input and for providing the Polyglass coatings.

At last, I would like to thank my family for their unconditional support throughout my time in Delft. I would like to especially show gratitude to my father, Jan Winters, for helping me prepare my samples, passing on his passion for technology, and always making time to talk about my progression and thoughts. Thank you to my friends for providing distraction during stressful times, and Pam for her constant support during this year.

Koen Winters
Rotterdam, September 2023

Abstract

The exposure of certain carbon steels to sour environments can result in severe hydrogen induced cracking (HIC) damage in the oil and gas industry. Current mitigation techniques in this field have low reliability or are not able to provide long-term protection against such damage. Recent advancements in thermal spray technology have resulted in a promising and cost-effective solution. Improvements in particle velocity and deposition efficiency have enabled coatings to achieve higher density and uniformity. High-velocity air fuel (HVAF) thermal sprayed NiCrMoW coatings are particularly interesting due to their outstanding corrosion resistance and mechanical properties. To ensure that equipment is sufficiently protected against the harsh environment of this industry, a thick coating is desired. However, as coating thickness increases, the performance of thermal sprayed coatings is frequently affected by residual stresses and unfavourable microstructural features.

To identify this effect, three NiCrMoW coatings with thicknesses of 250, 375, and 500 µm were applied with HVAF thermal spray technology on S235JR carbon steel. Samples were analyzed in order to evaluate differences in terms of microstructure, mechanical behaviour, HIC resistance, and corrosion resistance. An AK07 HVAF instrument in a controlled setting at the IOT research centre of the University of Aachen was used to ensure consistency among the coatings during the spraying process. Experiments to evaluate HIC resistance and corrosion resistance involved prolonged immersion in a sour environment, cathodic charging, open circuit potential measurements, and potentiodynamic polarization tests. Microstructural variation was examined with the use of SEM-EDS and optical microscopy. Additionally, subsurface microhardness measurements of the coating and underlying substrate were used to evaluate hardness and give an indication of the presence of residual stresses.

Findings indicate that the coatings exhibit excellent corrosion resistance. A small but noticeable decrease in resistance was however observed with increasing coating thickness. This decline can be attributed to two factors: an increase in the degree of oxidation and accumulation of residual stresses within the thicker coatings. Additionally, it is noteworthy that while the degree of oxidation and residual stresses increased with coating thickness, the porosity fraction decreased. Microstructural features in the coatings varied as a result of differences in thermal input, cooling passes and the influence of shot peening effects. Resistance to HIC of carbon steel in a sour environment was significantly improved by the application of the coatings in comparison with uncoated samples. This can be attributed to the excellent corrosion resistance, uniformity and absence of through-coating porosity in the coatings, the thickness did not have an influence. Furthermore, it was found that the galvanic interaction between the NiCrMoW coating and the S235JR carbon steel significantly accelerates the corrosion of the underlying substrate. Thicker coatings might be able to provide a greater physical defect-free barrier which can resist breaking, damage and erosion to prevent this galvanic effect.

Contents

Nomenclature

List of Abbreviations

AIDE Adsorption-induced Dislocation Emission

API American Petroleum Institute

APS Atmospheric Plasma Spray

BCC Body Centered Cubic

CLR Crack Length Ratio

CRA Corrosion Resistant Alloy

CSR Crack Sensitivity Ratio

CTE Coefficient of Thermal Expansion

CTR Crack Thickness Ratio

CVD Chemical Vapor Deposition

EDS Energy Dispersive X-ray

FCC Face Centered Cubic

FSS Fit-for-service

HAZ Heat Affected Zones

HCP Hexagonal Close Packed

HE Hydrogen Embrittlement

HEDE Hydrogen Enhanced Decohesion

HELP Hydrogen Enhanced Localized Plasticity

HIC Hydrogen Induced Cracking

HRC Hardness Rockwell C

HVAF High Velocity Air Fuel

HVOF High Velocity Oxygen Fuel

LPM Liter Per Minute

NACE National Association of Corrosion Engineers

ND Normal Direction

OCP Open Circuit Potential

PDP Potendiodynamic Polarization

PREN Pitting Resistance Equivalent Number

RD Rolling Direction

SEM Scanning Electron Microscope

SOHIC Stress Oriented Hydrogen Induced Cracking

SSC Sulfide Stress Cracking

TD Transverse Direction

TSA Thermal Sprayed Aluminium

XPS X-ray Photoelectron Spectroscopy

Constants

D_0 Diffusion constant

R Gas constant (8.3144 $\frac{J}{K \cdot mol}$)

Chemical Abbreviations

CO_2 Carbon Dioxide

FeS Iron Sulfide

H_2CO_3 Carbonic Acid

H_2S Hydrogen Sulfide

MnS Manganese Sulfide

WC Tungsten Carbide

List of Symbols

k Hydrogen solubility

K_I Stress intensity factor

Q_d Activation energy

List of Figures

List of Tables

1 Introduction

Corrosion in the oil and gas industry is a major concern, the harsh and corrosive operating environment can lead to various corrosion mechanisms, which frequently lead to equipment and infrastructure failures [1]. Such failures can result in significant downtime and possibly be a risk to health, safety, and the environment. A frequently encountered corrosion mechanism in the industry is hydrogen induced cracking (HIC). HIC occurs when susceptible carbon steels are exposed to hydrogen sulfide (H_2S) containing environments [2]. Corrosion reactions lead to the formation and consequent absorption of hydrogen atoms into the steel. Once the hydrogen atoms are present in the lattice, they can become trapped at defects in the microstructure and recombine into hydrogen gas (H_2). When sufficient hydrogen gas has accumulated, internal blisters can form, this usually occurs at the interface between nonmetallic inclusions and the steel matrix. HIC failure occurs when cracks initiate and propagate from these blisters [3–5].

Mitigating and preventing HIC involves the use of organic coatings, post-weld heat treatment, selection of HIC resistant materials, and periodic repairs. These have however been proven to lack the desired reliability, long-term viability, and cost-effectiveness [6–8]. Therefore, the demand for an alternative solution is desired. Thermal sprayed coatings in particular have regained attention in the oil and gas industry in recent years. While the technology has been implemented in the industry for a century, recent advancements in optimization have enabled researchers to produce dense, uniform coatings with less oxidation and residual stress [9–13]. As current application instruments are capable of producing thick corrosion resistant coatings it has the potential be used as a long-term solution.

The high velocity air fuel (HVAF) spraying technique is particularly of interest due to its ability to spray high-quality coatings at high deposition rates. The capability to spray large surface areas quickly and effectively makes it an attractive technique in terms of cost-effectiveness [9, 11]. HVAF technology is capable of spraying a wide variety of materials, one of which is exceptionally suitable for use in a sour environment.

$Ni_{57}Cr_{15}Mo_{16}W_4$, better known in the industry as Hastelloy C276, is known as a corrosion resistant alloy (CRA), in addition to its superior corrosion resistance it has a high abrasion resistance and good mechanical properties [14]. There is however a significant downside associated with the use of Ni-based coatings, which is their higher corrosion potential compared to carbon steels. This means that in the case of defects or impairment to the coating, galvanic interaction may accelerate the corrosion of the substrate. A thick, uniform and defect-free coating is thus crucial. Although a thick coating provides a greater physical

barrier, it is important to consider that with increasing coating thickness, residual stresses and a greater tendency for unfavourable microstructures increase [15, 16]. This research project is therefore focused on the effects of increasing coating thickness on microstructural features and properties, resistance to HIC, corrosion resistance, and galvanic interaction.

1.1 Background and industrial relevance

The oil and gas industry can be categorized into two different segments: upstream, and downstream. Upstream includes the activities which are related to exploration, while the downstream sector covers refining and purification into usable products. The downstream industry, which is the focus of this study, involves many processes and unit operations in which the oil and gas are transformed in order to extract products such as diesel, kerosene, and naphtha. Processes to obtain these products can involve for example desalting, distillation, and reforming, for which specific operation conditions are required [17].

Transformation units are prone to many different corrosion mechanisms which can lead to damage or failure. Repairs and removal of possible contaminants are time-consuming activities that can lead to interruptions of refinery operations with serious financial consequences. Preventing such failures is thus an important part of the industry. Many failures can be avoided by applying materials that are not susceptible to corrosive environments, periodic maintenance, inspection, and application of protective coatings and inhibitors. Nevertheless, it may occur that these measures are not sufficient or are not executed properly. Conditions may also change and lead to unintended exposure of equipment to more aggressive environments [18].

While crude oil and gas are not inherently corrosive, contaminants that these inherently contain in combination with environmental factors can lead to severe corrosion. Important factors and contaminants have been identified as the presence of a water phase, dissolved oxygen, HCl, mercaptans, nitrogen (N) compounds, CO_2, H_2S, O_2, abrasives, microorganisms, temperature, pressure, pH and organic acids and product flow [19, 20]. As a result of these factors, a large variety of corrosion phenomena are encountered such as environmentally induced cracking, atmospheric corrosion, pitting corrosion, crevice corrosion, galvanic corrosion, intergranular corrosion, erosion corrosion, cavitation corrosion, sour and sweet corrosion, corrosion under isolation, high-temperature corrosion and microbiologically induced corrosion [17].

The main cause of corrosion in the oil and gas industry is corrosion induced by CO_2, often denoted as sweet corrosion. In an article written by M. B. Kermani and D. Harrop [2] it was estimated that sweet corrosion accounts for about 28% of all failures. CO_2 dissolved in water forms the compound H_2CO_3, which usually leads to general, highly localized pitting corrosion or Mesa attack. Mesa attack is a form of localized corrosion and occurs when an iron carbonate film precipitates, but with a rate that is not high enough to form a dense protective film [21]. The severity of this corrosion mechanism is mostly related to the partial pressure of CO_2, flow rate, pH, and the temperature of the environment [17].

A second frequently encountered type of corrosion and the focus of this study is sour corrosion. Sour corrosion is the designation for corrosion originating from environments containing H_2S such as sour water or sour crude. Specifically, this type of corrosion is

encountered when metals are exposed to H_2S dissolved in water. Corrosion originating from this "wet" H_2S was approximated by the same article to be responsible for about 18% of total failures in the oil & gas industry [2]. When H_2S is dissolved in water it can react with iron to form iron sulfide scales and cause hydrogen absorption in metals. Common corrosion mechanisms which originate from sour service are hydrogen embrittlement (HE), HIC, sulfide stress cracking (SSC) and pitting. These mechanisms are especially corrosive for susceptible carbon steels which are often used in the refinery industry [17, 22].

1.1.1 Cost of corrosion

The annual global revenue of the oil and gas industry was estimated to be 1.5 trillion US$ in recent years [23], with an associated cost of corrosion reaching 60 billion US$ [24]. Even though these are estimates, the cost of corrosion would amount to 4% of the total revenue. These numbers highlight the economic significance of corrosion prevention [18]. The design of certain units and equipment, repairs, maintenance, inspection, replacements, use of coatings, and indirect costs from the loss of products or reduced productivity included, would even further increase global losses due to corrosion [2]. To reduce these costs, there is a continuous demand for new materials and technologies which can withstand the extreme environments to which equipment is exposed. Improving the lifetime of equipment for 5 to 10 years can already significantly reduce the total costs.

1.1.2 Effect on health, safety and environment

It is equally important that corrosion is avoided to prevent harm to health, safety and the environment. Leakage of fluids and gasses can result in pollution of soil, water and air, which can negatively impact the health of people living near refineries or harm local wildlife and coastal ecosystems. The contamination of groundwater can for instance have a serious consequence on the food chain as it may be used as a source of drinking water or for irrigation of crops. Pollution of air may lead to respiratory issues, illness or cancer [25].

Additionally, the carbon footprint of corrosion should be considered. In a recent article [26] it was estimated that the CO_2 emissions to replace corroded steels will be between 4.1% to 9.1% of the total global CO_2 emissions by 2030 if no actions are taken. The use of coatings can significantly increase the service life of steel and is thus an important aspect of reducing global emissions.

1.2 Reading guide

This report contains a total of six parts focussing on different parts of the study, this reading guide provides a short introduction.

Chapter 1 provides the objective and subject of this study to the reader and it provides background information about corrosion in the oil and gas industry.
Chapter 2 contains the theoretical background in the form of a literature review with an analysis of the mechanism of hydrogen embrittlement, hydrogen induced cracking and an evaluation of thermal sprayed coatings. Additionally, consideration is given to the requirements of thermal spraying for HIC prevention, focussing on HVAF and NiCrMoW coatings. Finally, the chapter provides the knowledge gaps from which four research questions are formulated with a subsequent introduction on how these should be answered in the experimental part of the study.
Chapter 3 evaluates the materials and methods which are used in this thesis, including the thermal spraying process at the RTWH Aachen, sample preparation and set-up of experiments. At the end of the chapter, the knowledge gaps are summarized and four research questions for the experimental part of this study are discussed.
Chapter 4 contains the results of the conducted experiments and a thorough discussion of how to interpret these.
Chapter 5 aims to answer the research question in the form of a conclusion, referring to the results and discussions.
Chapter 6, the final part of the report, suggests recommendations for future work.

2

Theoretical background

2.1 Hydrogen Embrittlement (HE)

It is well known that the absorption of hydrogen in metals can have a negative influence on their mechanical and corrosion properties. A reduction in properties can cause a material to fail at a point below its envisioned design. The phenomenon where hydrogen is absorbed in a metal diffuses through the microstructure and eventually causes a deterioration of properties is called hydrogen embrittlement (HE). When a significant quantity of hydrogen is absorbed in a metal, this combination of a reduction of mechanical properties and a high hydrogen gas pressure can lead to hydrogen induced cracking (HIC). A schematic of the most crucial steps is also shown in Appendix A. Before the mechanism of HIC can be introduced, it is important to understand what causes this deterioration of properties and how hydrogen is absorbed. The exact mechanism of the effect of hydrogen on the properties of steel is however still under debate. Three mechanisms of hydrogen embrittlement which are all theoretical and experimentally supported are Hydrogen Enhanced Localized Plasticity (HELP), Hydrogen Enhanced Decohesion (HEDE) and Adsorption-induced Dislocation Emission (AIDE), the mechanisms are schematically displayed in figure 2.1, 2.2 and 2.3 [27].

HELP is based on the formation of hydrogen atmospheres around mobile dislocations and dislocation obstacles near a crack tip. Such atmospheres enhance dislocation mobility

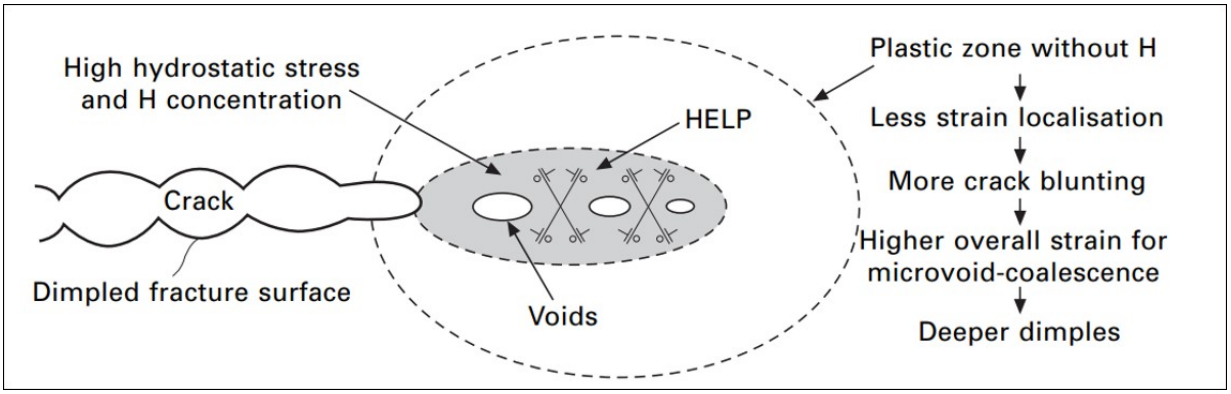

Figure 2.1: Schematic diagram of HELP, showing plasticity in localised high hydrogen concentrations [28]

and reduce dislocation-dislocation interactions [29]. Increased mobility means that lower stress is necessary to move dislocations and thus leads to enhanced localized plasticity or softening of the material. Furthermore, a reduction in dislocation-dislocation interactions leads to planar slip and a pile-up of dislocations in one slip plane [30]. This pile-up is then pushed against the particle-matrix interface which results in the nucleation of a void and failure at the interface [31]. This mechanism is schematically displayed in 2.1.

The hypothesis of HEDE as depicted in figure 2.2 proposes that areas with high concentrations of localised hydrogen atoms reduce the cohesive force of metal-to-metal bonds at crack tip locations. A study by Troiano in 2016 [32] suggested that the electron charge density in such bonds decreases due to the presence of hydrogen. The theory is that hydrogen can donate an electron to the partially filled 3d iron band which ultimately leads to repulsion of the metal atom cores. As a result, bonds are weakened in regions with high hydrogen concentrations which ultimately leads to hydrogen embrittlement.

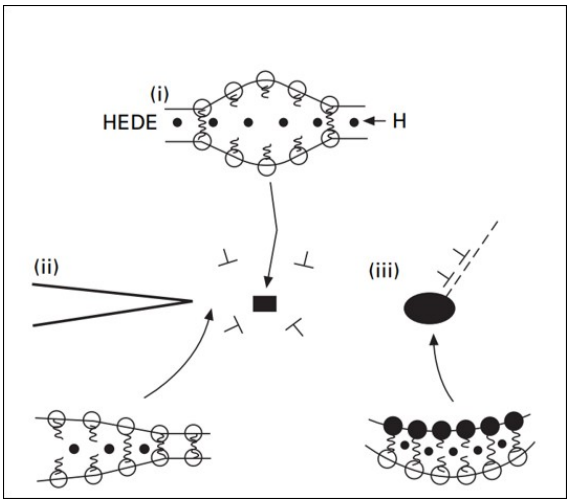

Figure 2.2: Diagram of HEDE, hydrogen weakening bonds (i) in the lattice, (ii) via hydrogen absorption, (iii) at the particle-matrix interface [33]

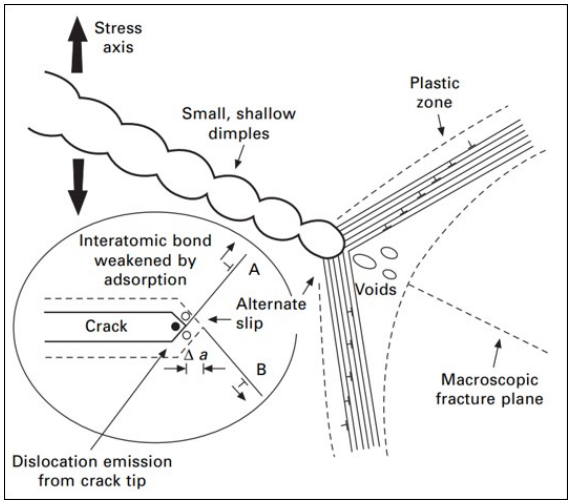

Figure 2.3: Diagram showing AIDE crack propagation through the coalescence of micro-voids in the plastic zone ahead of the crack [34]

The hypothesis of AIDE is displayed in figure 2.3 and describes that hydrogen absorption at the crack tip facilitates dislocation nucleation and subsequent movement of these dislocations into the material. The movement of these dislocations away from the crack tip results in a ductile to brittle transition. The effect of this mechanism can be better understood by describing the difference between brittle and ductile crack growth [35]. In ductile fracture, dislocations around a crack are generated in the plastic zone and contribute to blunting of the crack, coalescence and formation of micro-voids. A stable crack growth then occurs through the coalescence of such micro-voids under applied stress [31, 36]. In brittle fracture through hydrogen embrittlement, dislocation activity moving away from the crack tip results in minimal plastic deformation. This leads to unstable crack growth and thus brittle fracture [35].

Combined interactions of these three mechanisms can also occur. The degradation which is induced is different from each other but can simultaneously result in embrittlement.

The origin of hydrogen atoms leading to embrittlement can come from different sources. In the case of HIC, the source of hydrogen originates from the hydrogen reduction reaction in presence of H_2S, water and carbon steel. In the previous section, where sour corrosion was introduced, it was explained that water is also a necessary factor for such a corrosion reaction. When H_2S gas is dissolved in water it results in dissociation reactions 2.1 and 2.2 [37]. HS^- formation starts at a pH of 4, while S^{2-} dissociation starts at a pH of 10 [38]

$$H_2S_{(aq)} \rightleftharpoons HS^- + H^+ \tag{2.1}$$
$$HS^- \rightleftharpoons S^{2-} + H^+ \tag{2.2}$$

The anodic reaction of iron dissolution and cathodic hydrogen reduction are respectively:

$$Fe \longrightarrow Fe^{2+} + 2\,e^- \tag{2.3}$$
$$2\,H^+ + 2\,e^- \longrightarrow H_2 \tag{2.4}$$

Carbon steel can react with both products from this dissociation reaction of H_2S which in turn produces $FeS_{(1-x)}$ (iron sulfide) and atomic hydrogen. Depending on the conditions of the environment a variety of different iron sulfide compounds may form on the surface of steel when it is exposed to H_2S. The formation of these compounds depends on the temperature, pH, hydrogen sulfide activity and the ionic strength of the solution [39]. One of those compounds is mackinawite (FeS). Due to fast formation kinetics and high stability, it is often the initial corrosion product which forms [5, 40]. In the initial phase just after exposure, an ultra-thin layer of mackinawite below 1 µm is uniformly formed on the metal surface. Due to its high density, this solid film provides protection against corrosion. When the precipitation rate exceeds the corrosion rate, a second layer can rapidly grow on the initial film. Contrary to the solid and protective initial film, this second layer is brittle and porous. Additionally, the rate of growth is determined by the dissolution of the FeS film. High dissolution rates as a result of changes in the conditions of the environment can lead to shrinkage or stabilization of the second layer. In the latter situation, the dissolution of iron sulfides has then become equal to the rate of iron sulfide formation. A significant factor which determines these dynamics is associated when solutions reach a pH in the range of 2 to 3 [41]. The reactions of iron with bisulfide and sulfide ions are:

$$Fe^{2+} + S^{2-} \rightleftharpoons FeS_{(s)} \tag{2.5}$$
$$Fe^{2+} + HS^- \rightleftharpoons FeS_{(s)} + H^+ \tag{2.6}$$

Both iron sulfide and hydrogen produced from this reaction are adsorbed to the surface of the metal [40]. The final reaction can then be written as:

$$H_2S_{(aq)} + Fe \xrightarrow{H_2O} FeS + 2\,H^0 \tag{2.7}$$

The two adsorbed hydrogen atoms can either recombine and form molecular hydrogen gas with reactions:

$$H^0 + H^0 \longrightarrow H_2 \tag{2.8}$$

$$H^0 + H^+ + e^- \longrightarrow H_2 \tag{2.9}$$

Or alternatively, the adsorbed hydrogen atoms diffuse into the metal (H_{abs})[42]:

$$H^0 \longrightarrow H_{abs} \tag{2.10}$$

Recombined hydrogen molecules are too large to move into the metal and therefore return back into the process stream. The rate of recombination to hydrogen gas is however retarded by the presence of H_2S which acts as a so-called recombination 'poison' [43]. Besides H_2S, HCN can also act as a poison. HCN is a contaminant which is often present in crude oils [44]. Due to these poisons, hydrogen absorption in the metal lattice is promoted. Due to its small size, atomic hydrogen can easily move through the lattice by interstitial diffusion or along high diffusivity paths. Hydrogen diffusion through interstitial sites in the lattice can occur through octahedral or tetrahedral sites. As the required activation energy for tetrahedral interstitial sites is lower, it is a preferred sites for diffusion. As a result of heating, octahedral sites can become thermally activated to overcome this difference in activation energy and thus lead to accelerated diffusion rates [45, 46].

Hydrogen atoms can diffuse freely through the lattice, but once trapped, their movement is limited to exchange with other hydrogen atoms in the lattice [47]. Traps can be classified as reversible or irreversible and saturable or non-saturable. Hydrogen in reversible traps can diffuse back in the lattice with enough energy to overcome the lattice migration energy while for irreversible traps this energy is substantially higher with a negligible probability of hydrogen diffusing back into the lattice [48]. Examples of reversible traps include dislocation cores, vacancies, carbide interfaces and grain boundaries, while examples of irreversible traps include incoherent particles such as non-metallic inclusions, impurities, carbide precipitates and hydrides. Saturable and non-saturable traps have a distinct difference in the rate at which hydrogen diffuses take place [3, 4]. For saturable traps, the rate of hydrogen diffusion decreases after it is filled with a certain amount of hydrogen whereas for non-saturable traps this rate does not decrease. Saturable traps can thus only hold a limited amount of hydrogen while the capacity for non-saturable traps is infinite. In such cases, the blister can grow until the pressure is high enough to cause cracking of the metal [22]. Sieverts' law (2.11) can be used to explain how hydrogen concentration is controlled in traps, the law is denoted as:

$$C_L = k\sqrt{p_{H2}} \tag{2.11}$$

Where C_L is the hydrogen concentration in the lattice sites, k is the hydrogen solubility, and $\sqrt{p_{H2}}$ is the pressure of the hydrogen molecules in the trap. The law describes the concentration of hydrogen in traps as a function of the rate of hydrogen entry. The law is specifically used to understand how the concentration of hydrogen in traps is controlled and to make predictions of hydrogen concentration in traps as an effect of different conditions [49].

2.2 Hydrogen induced cracking (HIC)

As described in the previous section, hydrogen induced cracking (HIC) is a type of failure which is closely related to the embrittlement of metals through the introduction of hydrogen atoms in the lattice. A characteristic of such cracks is that these expand parallel to the surface [3], in figure 2.4b this hydrogen-filled void is schematically depicted. An exception is a situation where step-wise cracking or stress-oriented hydrogen induced cracking (SOHIC) occurs, individual HIC cracks connect to form one large crack from the effect of tri-axial stress conditions (figure 2.6b) [5, 50]. The first step of HIC occurs through the accumulation

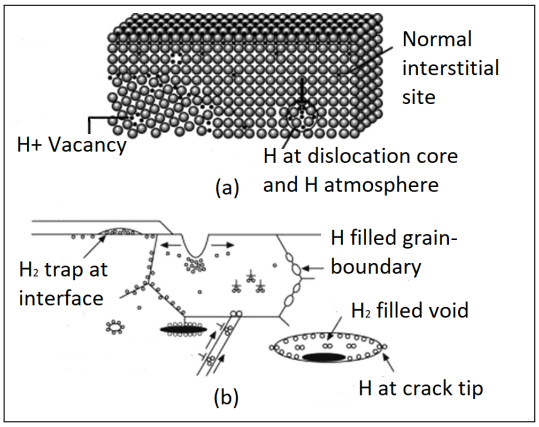

Figure 2.4: Schematic diagram of (a) hydrogen embrittlement and diffusion at atomic scale (b) trapping of hydrogen in the lattice [51]

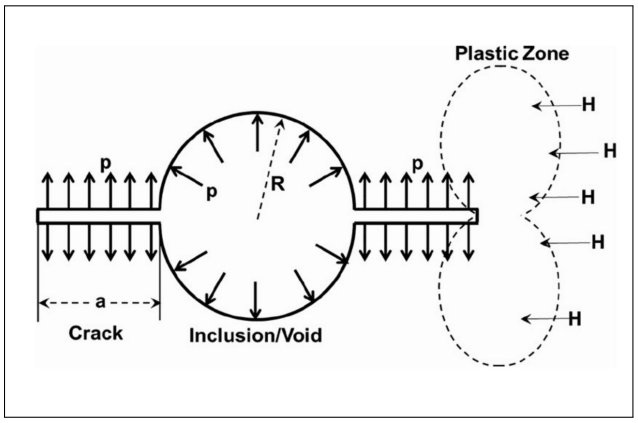

Figure 2.5: Schematic showing internal hydrogen pressure leading to cracking in embrittled areas and preferential diffusion of hydrogen to a plastic zone [52]

of hydrogen atoms in traps, which recombine into hydrogen gas molecules according to reaction 2.8. Hydrogen accumulation in irreversible and non-saturable traps can lead to a build-up of pressure. Through the combined effect of high internal pressure in traps and embrittlement of the steel, cracks can start to propagate (fig 2.5). Before such cracks appear, a phenomenon known as blistering is often observed [53]. Figure 2.6a shows a surface which is heavily affected by hydrogen induced blistering.

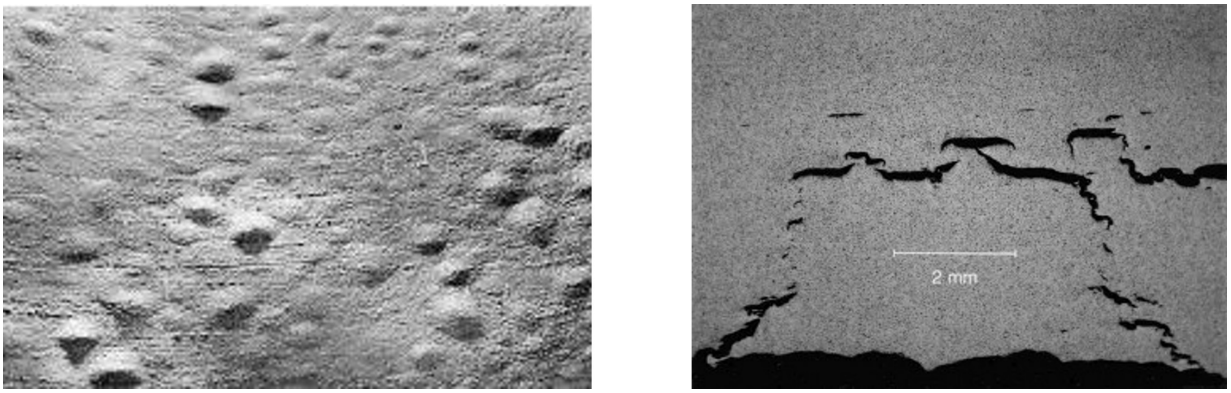

Figure 2.6: (a) Hydrogen induced blistering [54] and (b) Cracking from SOHIC [50]

Crack propagation in HIC is usually not continuous, cracks 'pause' when an unembrittled area of material is encountered. Hydrogen then quickly relocates and crack tip embrittlement once again allows the material to tear further [55]. In the crack tip, the hydrogen concentration tends to be higher than the hydrogen concentration in the bulk as stresses and strains provide more room for hydrogen diffusion. An expression for these concentrations is given by:

$$C_H = C_L \, exp\left(\frac{V_H \sigma_m}{RT}\right) \tag{2.12}$$

Where C_L is the hydrogen concentration in the lattice (as obtained from Sieverts' law), C_H is the hydrogen concentration at the stress tip, V_H is the partial molar volume of hydrogen in the metal, σ_m the hydrostatic stress at the crack tip, T the temperature in Kelvin and R the gas constant [56]. Additionally, an expression for these concentrations can be described with:

$$\frac{C_H}{C_0} = exp\left(\frac{\sigma_h}{\beta}\right) \tag{2.13}$$

Where C_0 is the hydrogen concentrations in the bulk, β is a factor dependent on elastic modulus and molar volume of the metal, and σ_h is the hydrostatic stress [57]. Fracture mechanics is often used to predict when a material yields. When the stress intensity factor K_I exceeds the toughness K_{IC} of a material, cracks start to propagate.

For HIC the stress intensity factor is given by $K_{IP}(H_2)$ and the fracture toughness as $K_{IC}(H)$. To derive the stress intensity factor $K_{IP}(H_2)$ a standard model for a center through crack in an infinite plate can be used. This model describes that the stress intensity is given by:

$$K_I = \sigma\sqrt{\pi a} \tag{2.14}$$

Where σ is the stress which is exerted and a the size of the void, which is also illustrated in figure 2.7 on the next page.

The difference between K_I in this model and ($K_{IP}(H_2)$) is the load, where σ should be replaced by the internal hydrogen pressure. Fu and Fang describe that $K_{IP}(H_2)$ can be easily produced from K_I in the linear elastic range by using a correction factor of 0.6313, which results in equation [56]:

$$K_I P(H_2) = 0.6313 \cdot P_H \cdot \sqrt{\pi a} \tag{2.15}$$

In which the hydrogen pressure is described by P_H. The fracture toughness can be easily obtained from Sieverts' law from equation 2.11, the hydrogen concentration at the crack tip from equation 2.13, and the equations from the three stress components at the crack tip of a loaded plate. These stress components, which were developed by Irwin in the stress intensity approach are given by [31]:

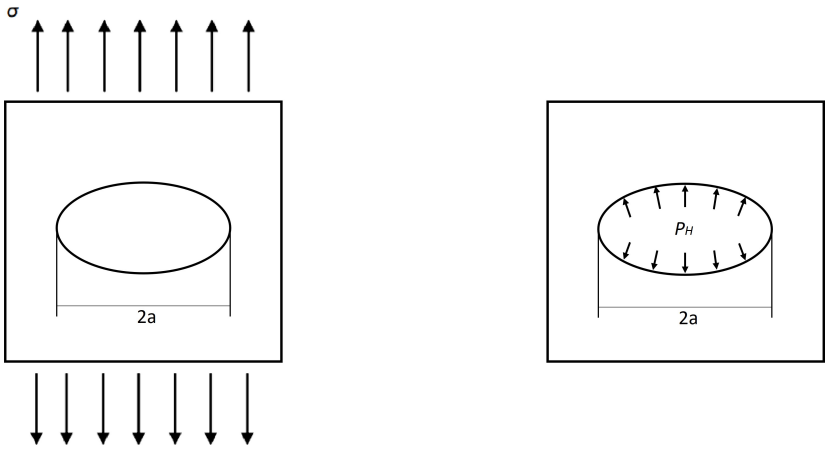

Figure 2.7: Fracture mechanics for an infinite plate with a centre crack and crack length 2a and (b) for a HIC crack with hydrogen pressure P_H (adapted from [31])

$$\begin{aligned} \sigma_x &= \frac{\sigma\sqrt{\pi a}}{\sqrt{2\pi r}}\, f_{ij}(\theta), \\ \sigma_y &= \frac{\sigma\sqrt{\pi a}}{\sqrt{2\pi r}}\, f_{ij}(\theta), \\ \tau_{xy} &= \frac{\sigma\sqrt{\pi a}}{\sqrt{2\pi r}}\, f_{ij}(\theta) \end{aligned} \tag{2.16}$$

In these equations r is the distance from the crack tip, $f_{ij}(\theta)$ a function which depends on load conditions and crack geometry. Additionally, $\sigma\sqrt{\pi a}$ can also simply be described by K_I such as derived from equation 2.14.

The hydrostatic stress, which was described by σ_m in equation 2.13 can now be written from equation 2.16 as:

$$\sigma_m = -\frac{2K_I(1+v)}{3\sqrt{2\pi r}}\, f_{ij}(\theta) \tag{2.17}$$

with v the Poisson's ratio. Equation 2.17 and equation 2.11 can now both be inserted into equation 2.13 to obtain:

$$ln\left(\frac{C_H}{\sqrt{P_H}}\right) = K_I \left[\frac{\sqrt{2}\,(1+v)V_H}{3\sqrt{\pi r}\,R\,T}\right] \tag{2.18}$$

from which the fracture toughness as a function of critical hydrogen pressure at the crack tip and temperature can be derived [58]:

$$K_{IC}(H) = \sqrt{rc}\cdot ln\left(\frac{C_H}{\sqrt{P_H}}\right)\cdot T\cdot\left[\frac{3\sqrt{\pi}\,R}{\sqrt{2\,(1+v)\,V_H}}\right] \tag{2.19}$$

Additionally, since hydrogen can be adsorbed and desorbed from the crack tip, an equation for thermodynamic equilibrium is required.

By combining the Abel-Noble gas equation and Sieverts' law, the following equation is derived:

$$C_0 = P_H \cdot exp\Big(\frac{P_H B}{RT}\Big) \tag{2.20}$$

Where B is the molar co-volume of hydrogen with a value of $1.584 \cdot 10^{-5} \mathrm{m}^3/\mathrm{mol}$ and P_H the hydrogen pressure [59].

With the formulation of the fracture toughness $K_{IC}(H)$ and the stress intensity factor $K_{IP}(H_2)$ a prediction can now be made about HIC. When $K_{IP}(H_2) > K_{IC}(H)$ is satisfied, cracks will propagate. Crack growth may continue until the material fails or until the the relationship has reached $K_{IP}(H_2) < K_{IC}(H)$, for example when it has reached an area with a lower P_H, upon which growth stops.

2.3 Susceptibility to HIC

Exposure of metals to wet H_2S environments does not necessarily always lead to HIC. The susceptibility of a metal depends on several factors. These include the type of metal, its microstructure, composition and texture and the severity of the environment where it is exposed to. The microstructure is an important factor which influences susceptibility to HIC as the amount of inclusions and the processing history directly determinate the amount and type of traps which are present in the material. In addition, contaminants in the environment and specifically the pH and concentration of H_2S are important properties that control whether an environment is severe enough to cause HIC.

2.3.1 Microstructure

The microstructure of a metal has a significant influence on the vulnerability to HIC. There is a complicated concurrence of factors linked to the microstructure that may eventually lead to susceptibility. The processing history and composition of the metal are particularly important since it can influence the occurrence of certain non-metallic inclusions and the ability of the metal to accommodate hydrogen. On the other side, fine precipitates and fine carbines decrease the mobility of dislocations as this increases strength and may therefore be desirable in reducing the susceptibility. It is generally accepted that steels with a sulfur content higher than 0.002 wt% in combination with a high content of manganese ($> 1\%$) have low resistance to HIC. Hot rolling such steels leads to the formation of large elongated manganese sulfides (MnS) which serve as hydrogen traps and primary initiation sites of cracks [60]. In addition, the hardness of a metal can have a significant contribution to the susceptibility to HIC as it affects crack initiation. When hardness increases, low plasticity increases the stress concentration at crack notches and thus allows failure at a lower hydrogen gas pressure in the blisters [61]. Steels with a hardness lower than HRC 22 (248HV10) are generally considered to be resistant to HIC [4].

Besides composition, unfavourable crystal structures can be caused by processes or certain alloy elements. Metals with a BCC type lattice have a higher diffusivity for hydrogen than FCC and HCP-type structures. BCC lattices have a low atomic packing fraction, which means that there is relatively more space for interstitial atoms to move through the lattice

[22]. Numerous studies have been conducted on the effect of crystal structure and texture on susceptibility and resistance to HIC. A preferred phase was found to be austenite as it effectively and reversibly traps hydrogen, which retards embrittlement. Austenite is however not a stable phase for carbon steels at ambient temperatures. Martensite can be formed in steels by quenching from the austenite phase, this however creates a brittle steel with high hardness and is thus highly susceptible to HIC [62]. Most studies concluded that for carbon steels acicular ferrite and lower bainite have the highest resistance to HIC. Park et al. [4] compared ferrite/degenerated pearlite (DP), ferrite/acicular ferrite (AF) and ferrite/bainite (B) for their effect on hydrogen trapping, hydrogen induced cracking and sulfide stress cracking. AF and B were found to have respectively the lowest apparent diffusivity by a factor of two with respect to the DP microstructures, furthermore, nucleation of cracks in these steels was found at martensite-austenite (MA) constituents which are formed during cooling.

Forero et al. [63] tested the susceptibility of heat-affected zones to HIC and SSC with slow strain rate testing (SSR) and hydrogen permeation tests. For these tests, two types of carbon steel, X80 and X56 with both dissimilar (X56/X80) and similar joints (X80/X80) were used. It was found from the SSR test that ferrite-pearlite and ferrite with MA in respectively X56 and X80 were most susceptible to hydrogen embrittlement. The least susceptible microstructure was acicular ferrite, grain boundary ferrite in the weld metal and lower bainite in the HAZ. According to the authors, this resistance in the HAZ had occurred due to coarsening of the grains and MA decomposition.

More recent studies [64–66] were focused on the role of crystallographic texture on hydrogen induced cracking, authors found that textures dominated in the {1 1 1} ND, normal direction fibre improved resistance to HIC, while samples with similar microstructures and fibres {0 0 1} in ND and close to random textures made steels more prone to HIC. The reason behind it is that a reduction of transgranular, intergranular and low resistance cleavage paths was achieved by reducing 0 0 1 oriented grains while increasing {1 1 1} fibres improved the number of high resistance intergranular crack paths. These low and high-resistance crack paths associated with the textures were found to be respectively high-angle boundaries and low-angle boundaries.

2.3.2 In-service environmental conditions

The environment has a significant role in the degree of hydrogen charging and permeation. An important distinction should be made with respect to the environment in upstream and downstream which is often overlooked. NACE has two different international standards for resistance to environmental cracking, MR0175 [67] and MR0103 [68] which are respectively defined for upstream and downstream. Parameters which influence the behaviour of carbon steels in upstream sour environments are partial pressure H_2S, cyanides, presence of water, pH of the solution, chloride concentration in the water phase, temperature, exposure time, presence of sulfur, oxidants and the presence of non-production chemicals. For downstream these parameters are partial pressure H_2S, cyanides, presence of water, pH of the solution, temperature, exposure time and bisulfide ion concentration [68]. Of which the most critical factors are considered to be the pH, concentration H_2S, temperature, concentration of cyanides and the presence of water.

Conditions which are both accepted by the American Petroleum Institute and NACE at which blistering and HIC can occur are:

- $>$ 50 ppmw H_2S in aqueous phase
- $\geq$ 1 ppmw H_2S in aqueous phase at pH $<$ 4
- $\geq$ 1 ppmw H_2S in aqueous phase at pH $>$ 7.6
- $>$ 0.3 kPa partial pressure H_2S in combination with the aqueous phase

Cyanide only affects the process at pH values above 7.6, at values $\geq$ 20 parts per million by weight (ppmw). A low potential for HIC is therefore considered to be an environment where the pH is between 4 and 7.6, with cyanide content $<$ 20 ppmw, and H_2S $<$ 0.3 kPa in the gas phase or $<$ 50 ppmw H_2S in aqueous phase. An aggressive environment or high potential is considered when cyanides in aqueous phase are $>$ 20 ppmw, at pH $>$ 7.6 and H_2S in aqueous phase are $>$ 2000 ppmw or when the pH is $<$ 4 with H_2S $>$ 50 ppmw in aqueous phase [68, 69]. With increasing temperatures, H_2S dissociation and hydrogen diffusion rates increase hydrogen uptake in the metal. Most fractures occur at temperatures between ambient and 150 °C. More importantly, however, is that cracking often occurs when susceptible metals are first charged with hydrogen at high temperatures and then cooled. A phenomenon caused by a temperature-induced ductile to brittle transition [68, 70].

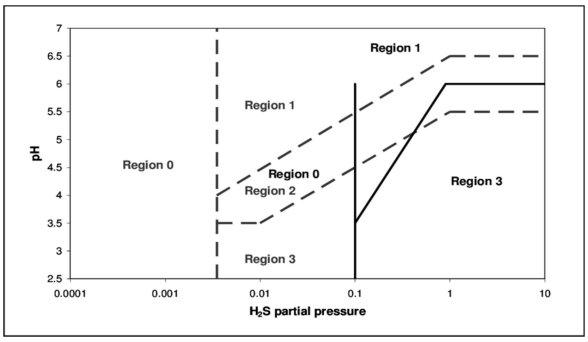

Figure 2.8: Fit-for-purpose diagram based on HIC severity regions [71]

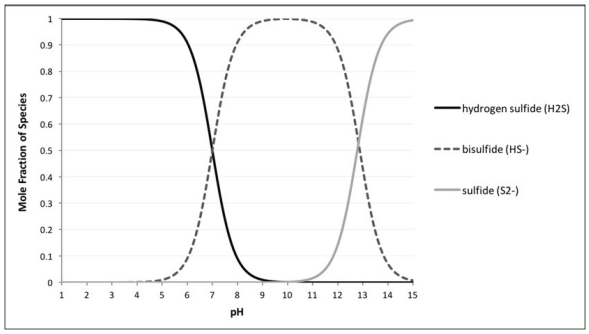

Figure 2.9: Dissociation of H_2S into HS^- and S^{2-} as function of pH

MR0103 [68] furthermore provides a graph with severity regions based on pH and concentration of H_2S, from this graph the risk of sulfide stress cracking can be predicted but can not directly be used for risk of hydrogen induced cracking. Two alternative models for HIC have been proposed in the literature as an addition to the model proposed by NACE, one of these is developed by Kittel et al. [72] and is based on measurements with the NACE TM0284 standard test method for determining HIC susceptibility. As with the model of NACE, pH and H_2S partial pressures are used to predict the severity of an environment. The diagram is designed to be used as a 'fit-for-purpose' model to determine whether a certain metal can be used for the intended sour service [72]. The second more recent model by Schröder et al. [71] which can be seen in figure 2.8 is built upon the model by Kittel. While the Kittel model is widely used it is limited to partial pressures of H_2S between 1 to 10 mbar. In this figure, four regions are depicted, in which region 0 is represented as an environment with negligible severity, and region 3 is an environment with high severity.

Note that this diagram only includes the pH range from 2.5 to 7, this means that this diagram is based on the reactions of HS^-, as explained previously dissociation of S^{2-} starts at a pH of 10 (fig 2.9). While this diagram does not include pH regions above 7, many refining process environments operate in alkaline environments. Sulfide corrosion can still occur from the active HS^- and S^{2-} species, forming sulfide corrosion products as in acidic environments. A limitation of existing literature is that test environments are solely based on pH and H_2S concentration while environments in the oil and gas industry are more complex. An example when HIC can occur at high pH is in the presence of cyanides. A reaction which can cause formation of atomic hydrogen is:

$$Fe + 2\,H^+ + 6\,{CN_6}^{4-} \longrightarrow {Fe(CN)_6}^{4-} + 2\,H^0 \tag{2.21}$$

It can furthermore result in the formation of a complex ion ($Fe(SCN)4^{2-}$). Which results in the destruction of the initial solid FeS film [44].

2.4 HIC mitigation and prevention

Prevention of HIC in the oil and gas industry involves a mixture of procedures to mitigate, control or eliminate such types of corrosion. Measures can be taken in the form of repairs, reducing the severity of the corrosive environment, use of CRA or the application of linings and coatings. Repairs can involve removing old damaged material and replacing it with new material, post-weld treatments of HAZ or embrittlement relief. [6, 7].

A preventative procedure to protect equipment from sour environments can be by replacing material with CRA. Although it is an expensive measure it is very effective. Certain CRA are specifically designed to have a high resistivity against corrosion such as HIC [67]. A cost assessment is usually made to determine whether it is economically reasonable to replace certain materials that have not reached their expected lifetime or if it is cheaper to use other mitigation methods [73].

Coatings to prevent HIC are usually applied after hydrogen embrittlement has been detected or when there is a high chance that HIC will occur. The objective of these coatings is thus to extent the lifetime of equipment. A Fit-For-Service (FFS) procedure can be used to assess the HIC damage, API article 571 section 7 describes what acceptance criteria should be handled and the remediation that can be applied to prevent further damage. Specifically, subsections 7.6.1 and 7.6.2 specify that hydrogen charging can be controlled by applying a barrier coating (organic, metal spray, weld overlay etc.) or lining to the inside surface of the equipment [74].

Coatings which are frequently used in the oil and gas industry are fusion bonded epoxy, glass flake vinyl ester acrylic co-polymers, amine-cured novolac phenolic epoxy coatings and epoxy novolak vinyl-ester glassflake coatings [75, 76]. These coatings each have certain advantages in terms of resistance to chemicals, environment, abrasion and properties such as strength, flexibility and durability. Fusion bonded epoxy is a thermoset coating which is typically used in temperatures ranging from 180 °C to 250 °C. It is applied in powder form and heated to a liquid after it has been distributed evenly over the substrate it solidifies as a result of chemical cross-linking [77]. Glass flake vinyl ester acrylic co-polymers is a two-component coating and is known for its resistivity in environments with reactive

chemicals, solvents and high acidity or alkalinity. Glass flakes are added to further increase this resistivity but also to improve abrasion resistance and hardness [78]. Amine-cured novolac phenolic epoxy are hard coatings with high substrate adhesion often used for harsh corrosion environments and epoxy novolak vinyl-ester glassflake coatings are characterized by their high corrosion resistance at high temperatures and mechanical properties. Such coatings are often used for storage tanks, gas cleaning units and piping [78, 79].

Although these coatings have proven to protect equipment from coming into contact with harsh environments, there are certain downsides. Most importantly, such coatings are often characterized by their relatively short lifetime when exposed to H_2S [80]. It is often found that the lifetime is shorter than the time between turnarounds. Such turnarounds are planned every 3-6 years and are used to regenerate the plant. Recoating equipment with these coatings is a time-consuming process, and curing the coatings may take a long time before it is fully hardened. Studies have also shown that the effect of elevated temperature and pressure in corrosive environments can lead to significant degradation and that adhesion may decrease when used in H_2S environments [80, 81]. A new type of coating which has a 20+ year lifetime and meets the requirements to be used in the harsh corrosive environment of the refinery industry should therefore be adopted [77, 80]. Recent research is devoted to investigating the use of coatings with longer life expectancy and stability. Thermal sprayed coatings in particular have regained attention in recent years. While it has been used for over a century, recent innovations have enabled researchers to achieve dense uniform coatings with less porosity and oxidation. Application of this improved technology in combination with corrosion-resistant materials could be a promising solution for the prevention of HIC.

The general concept of thermal spraying is that a coating material, often called feedstock, is heated in a spray torch by electrical discharge or chemical combustion and then launched from a nozzle with compressed gas at high velocity and temperature. This stream of combustion gasses and semi-molten material is then propelled towards a substrate where the particles are merged together by kinetic energy and thermal energy to form a coating. Coatings can be metallic or non-metallic and are consumed in the process in the form of a solution, powder, rod or wires. Thermal sprayed coatings are characterized by their high performance, resistance to erosion and wear, resistivity in corrosive environments and durability [16].

Thermal spraying has undergone significant advancements in recent years and therefore remains a relevant subject for research in many industries. In recent years, a considerable amount of publications featured new application techniques and coating materials for the oil and gas industry with promising results [8, 10, 13, 82]. A significant benefit of thermal sprayed coatings is that it is very fast and relatively simple. It has furthermore proven to provide a cost-effective solution to extend the lifetime of equipment in the refining industry and in applications to protect equipment from H_2S environments [8, 12, 83].

2.5 Introduction to thermal spray technology

As introduced in the previous section, thermal sprayed coatings pose as a promising solution to protect carbon steels in hydrogen sulfide environments. These coatings are proven to be highly corrosion resistant, have excellent mechanical properties, and are safe to use but most importantly are cost-effective and fast.

Thermal spraying is the general term for a group of processes which are used to deposit heated materials as coatings. The first basic technology originates from the 1900's and since then a number of sophisticated different thermal spray techniques have been introduced for various applications [84].

Thermal spray technology is most commonly classified in terms of combustion-, electrical and cold spraying processes, where the most important properties in which the process varies are their operating temperature and particle velocity. Both of these also have the most significant effect on coating quality [85]. This variety of techniques provides a wide range of options for spraying materials with different coating properties [86]. A common representation of the various thermal spray processes is depicted in figure 2.10.

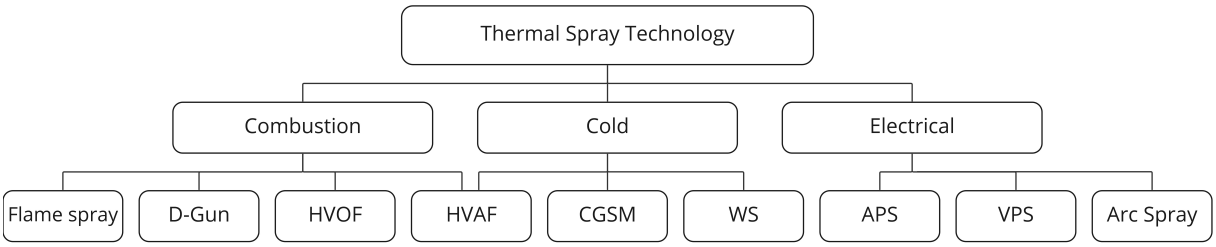

Figure 2.10: Thermal spray technologies are categorized in different classes (adapted from: [53])

	HVOF	HVAF	Detonation gun	Air plasma spray	Vacuum plasma spray	Electric Arc
Particle temperature (°C)	2800	<1600	3000	>3800	>3800	>3800
Particle Velocity m/s	600-1000	800-1200	600-1000	200-600	400 - 600	50-200
Spray rate (kg/h)	20-100	50-500	65-150	50-150	65-150	150-200
Adhesion (MPa)	70-100	100-200	>70	50-150	>70	10-40
Porosity (%)	Low	Extremely Low	Low	Moderate	Moderate	High
Oxidation (%)	Moderate/Low	Low	Moderate/Low	Moderate/Coarse	Low	Moderate/High

Table 2.1: Comparison between different techniques, data from different sources may vary depending on equipment and material use. This overview gives an indication of the performance of the application methods [53, 86, 87]

Electrical spraying can be divided into two types of technologies, both have in common that an electrical discharge is used as an energy source. The first technique, wire arc

spraying, is a process where feedstock in the form of two solid wires or rods are brought together and consumed as electrodes. Upon contact, a high voltage melts the electrodes into small particles of different sizes. The particles are then propelled towards the substrate with compressed air or an inert gas. The second electrical spraying technology is plasma spraying, where an electric arc is generated to create a high-temperature ionized plasma from a mixture of inert gases such as Argon, Helium, Hydrogen or Nitrogen. Particles are propelled into the plasma with an inert gas which heats them. Although plasma spraying is generally more expensive, it has an important advantage over wire arc techniques as different types of materials can be used and the particle size can be controlled [5, 16, 53]. Both spray guns are schematically represented in figure 2.11a and 2.11b.

In combustion spraying a mixture of oxygen and fuels are used as energy sources. This mixture is injected into a combustion chamber where a high temperature flame is produced upon ignition. As with plasma spraying, the feedstock is propelled through this flame to bring particles into a molten or semi-molten state. Combustion processes can further be divided into high- and low-particle velocity processes. A low particle velocity process is flame spraying, which is based on the first invented thermal spraying technique. It generally produces flames with temperatures ranging from 3000 to 3300 °C and velocities of 80 to 100 m/s. While flame spraying is a cheap technique, it produces low-quality coatings with high porosity (10-15%). Such coatings are therefore considered to be not useful as corrosion coatings since these are significantly permeable. High-velocity processes on the other side such as HVOF which is depicted in figure 2.11c can achieve particle velocities between 500 to 2000 m/s at temperatures of 2500 to 3000 °C. Coatings produced with HVOF generate high-quality coatings with porosity below 2% [86].

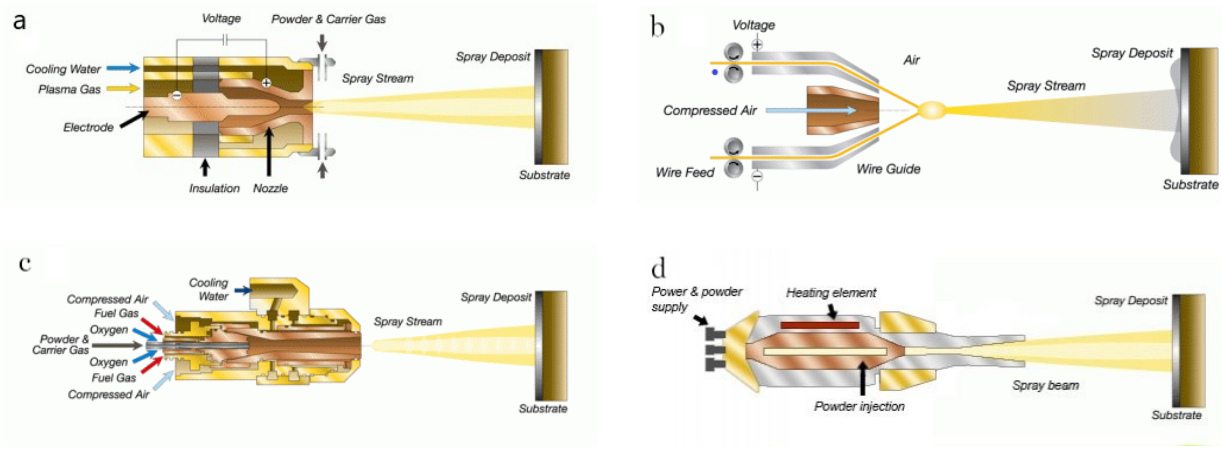

Figure 2.11: (a) plasma- and (b) wire arc spraying process (c) HVOF process and (d) Cold spraying process [88]

Cold spraying is a unique solid-state process which obtains high kinetic energy from high particle velocities rather than from thermal energy. The benefit of lower operating temperatures is that it allows a certain degree of control over the microstructure. Furthermore, cold spraying has the advantage of having low oxidation, absence of grain growth, phase change and decomposition [86]. As the technique operates below the melting temperature

of the feedstock it is necessary that the particles can deform plastically solely from the kinetic energy while in solid state [53].

Certain materials are therefore not compatible with cold spraying. A schematic representation of a cold spraying gun can be seen in figure 2.11d. A high-pressure jet is first heated in the combustion chamber in the middle of the gun. Powder is injected in this chamber by means of a carrier gas which is often a combination of air, nitrogen or helium. The gas jet with the powder leaves the gun through the nozzle as a supersonic jet [89].

At last, high-velocity air-fuel (HVAF) is an important piece of technology which has gained much attention in recent years. HVAF is a technique which is derived from HVOF, in which pure oxygen is substituted by compressed air. The compressed air functions as a coolant but also increases pressure in the combustion chamber [90]. The benefits of this modification are that it reduces the operating temperature and increases the particle velocity, the combination of these two factors can significantly improve coating quality. It additionally reduces operating costs as compressed air is a lot less expensive than pure oxygen and due to the higher velocities, the deposition rate is relatively high [91]. As with cold spraying, the coating quality is high from the elimination of oxidation and porosity. While it is displayed in figure 2.10 as cold spray it is often referred to as a 'warm spray' since it operates around temperatures of 1900-1950 °C while cold spraying is typically performed below 800 °C. The greatest benefit of HVAF over other spray techniques is that the quality remains excellent while spraying at high deposition rates [92].

2.6 High velocity air fuel (HVAF) coatings

Due to the exceptional capabilities of the HVAF thermal spraying technique, especially in terms of low probability of coating defects and cost-effectiveness, it will be the focus of this thesis. This section is divided into three parts, the first part (2.6.1) is a more general explanation of thermal sprayed coating microstructure and properties. The second part (2.6.2) introduces the HVAF instrument and the third part from subsection 2.6.3 and onwards starts with an introduction to the HVAF instrument and explains how these coating properties are influenced by spray parameters and instrument configurations.

2.6.1 Coating microstructure

Coatings applied with thermal spraying are composed of a large amount of different particles. When the stream of gas, liquid-, solid- and semi-molten particles exit the thermal spray instrument and impinge the substrate, the droplets flatten out due to the high kinetic energy and solidify into disk-shaped splats [93–95]. Optimally, these splats are tightly stacked on top and next to each other. The particles adhere to the substrate primarily by mechanical interlocking and to a small extent through metallurgical bonding [16]. A schematic representation of thermal sprayed coatings can be seen in figure 2.12, where imperfections are shown such as porosity, oxides and unmelted particles. Figure 2.13 displays the cross-section of an actual thermal sprayed coating.

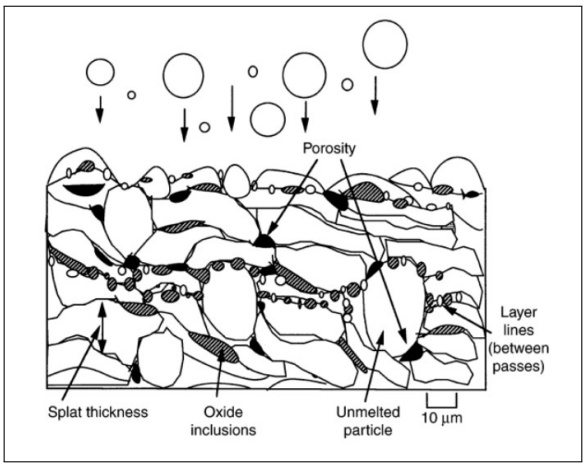

Figure 2.12: Schematic of thermal sprayed coating structure [96]

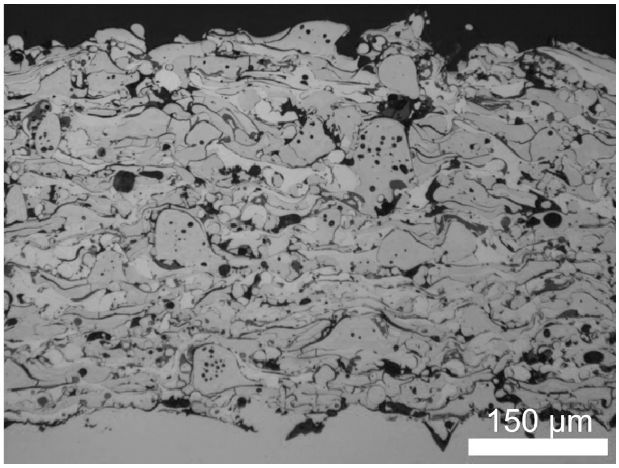

Figure 2.13: Cross-section of a thermal sprayed coating [97]

In order to obtain a uniform coating it is desirable that there is little space in between the overlap of these disks. To achieve this, factors during the process such as the temperature and particle velocity at impact, the angle of application relative to the substrate surface, oxidation of the particle and temperature gradient are crucial. Furthermore, the properties of the substrate can influence splat stacking due to inconsistent surface roughness and temperature. Splats may fragment at impact as a result of sub-optimal spraying conditions [93], the difference between splat fragmentation and optimal splat formation is shown in figure 2.14. It is important that splats do not fragment as it results in poor stacking, loss of adhesion, an increase of oxidation and formation of pores [98].

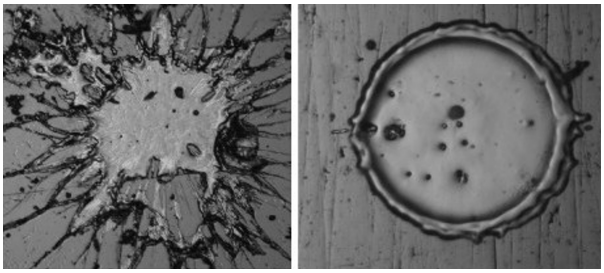

Figure 2.14: Aluminium splats showing fragmentation of splats [93]

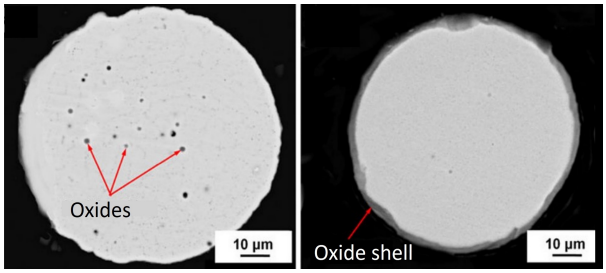

Figure 2.15: Oxidation of droplet showing formation of oxide shell [99]

Several studies [16, 93, 100] on the formation of splat types have shown that fragmentation occurs due to local pressure under the molten droplet after impact. There are two primary causes for this. The first is the presence of condensates and adsorbates on the surface, this can easily be avoided by proper surface preparation. The second is more challenging as it requires the right spray properties for the corresponding material, disk formation requires wetting on the surface, and such wetting is obtained when the substrate has contact with the whole surface area of the splat. Bad wetting is characterized by space underneath the edge or centre of splats, these spaces are susceptible spots for void formation, the splat should not be completely molten but it does need to have enough kinetic energy to deform at impact [16].

Thermal spraying at high particle velocity and relatively low temperature has a crucial advantage over other techniques in obtaining high-quality coatings. The temperature is generally below the temperature at which particles become fully molten but high enough to lower critical velocity which is needed to form a coating. Since the particles at impact are in a semi-liquid or solid state rather than a liquid state, will greatly reduce fragmentation [101].

Oxidized particles

Oxidation has a negative influence on the mechanical properties of the coating. Oxidized particles can for instance disrupt the microstructure and ductility. The latter is especially important in metal coatings as metal oxides are generally brittle and have different thermal expansion coefficients compared to 'normal' metals [102]. The coating can become oxidized from in-flight oxidation or during post-impact cooling on the substrate. In-flight oxidation is strongly influenced by the particle stream temperature, -turbulence and the type of carrier gas. Furthermore, the amount of oxygen which is entrained depends on the velocity of the jet. Deshpande et al. [103] found that entrainment is lower for HVOF than plasma processes, while for wire arc and APS entrainment of air was even higher. High entrainment in combination with a high particle temperature was found to generally give rise to a high chance of oxidation. Oxidation in a coating can be avoided by using a technique with low jet temperature and high velocity, table 2.1 reflects this as well. HVAF is thus a technique with a low chance of oxidation while for wire arc it is relatively high.

In-flight oxidation is characterized by a layer of oxide that forms as a shell around molten droplets in the particle stream, figure 2.15 shows deposition of particles with and without an oxide shell. High turbulence can destroy this layer and distribute the oxides evenly in the bulk of the droplet. Recent research on Ni and Ni20Cr splat formation found that these oxide scales may also break up and form a cap on one side of the droplet, resulting in thick oxide chunks between the splat interface after impingement [104]. Post-impact oxidation occurs when splats are cooling, and forms as a thin film in between successively sprayed layers.

Finally, the role of alloying elements is a key aspect in the oxidation of particles in splats [105]. Besides the oxidation of a whole particle, it can also be possible for particles in an alloy to oxidise separately from each other. Mathews et al. [106] found that oxidation of NiCr splats first occurred by fast nickel oxide nucleation and was then followed by encapsulation of a slower growing Cr_2O_3 phase. It is desirable to choose elements which reduce oxidation in order to limit oxidized scales in the lay-up. In certain scenarios, there is some benefit to oxidation of thermal sprayed coatings. Cr_2O_3 and α-Al_2O_3 for example are both stable oxides which can provide protection at high temperatures when it is formed on the surface of coatings [86].

Porosity

Uneven stacking, fragmentation of splats and bad wetting can all be a cause of void formation. The term for such voids is typically porosity, which is often one of the most negative aspects of thermal sprayed coatings. Microcracks are a special type of porosity due to the a-typical shape and the fact that formation is not necessarily the result of a stacking

error. Formation of such cracks can occur due to a build-up of stresses in brittle material during the cooling of splats. Ceramic coatings are especially prone to the formation of microcracks due to their brittle nature [107].

A distinction should furthermore be made between interconnected porosity and closed porosity. While both are harmful to the performance of a coating, interconnected porosity should especially be prevented. Such porosity is a network of voids and cracks which serve as a path for the diffusion of corrosion species. Even in mild cases, corrosion products can collect through interconnected paths and collect under the coating. this leads to a loss and adhesion and may cause delamination. In severe situations, it leads to corrosion reactions and causes HIC. Closed porosity in a coating reduces the resistance to wear and erosion.[83, 86, 108, 109].

Residual stresses

Residual stresses are generated in thermal sprayed coatings. The intensity depends on the conditions and the material of the coating and substrate. High residual stress has a negative impact on the quality of the coating as it can result in a loss of interfacial adhesion. The origin of these stresses comes from quenching and cooling stresses. Quenching stresses occur in the first stage when particles are deposited and solidified [110]. As the splats are tightly bound between other splats and the underlying layer, it is impossible that these completely contract during solidification and therefore result in quenching stresses. Cooling stresses originate from a mismatch in the thermal expansion of splats and the underlying substrate. The formation of either tensile or compressive stresses depends on the relative expansion coefficient [111].

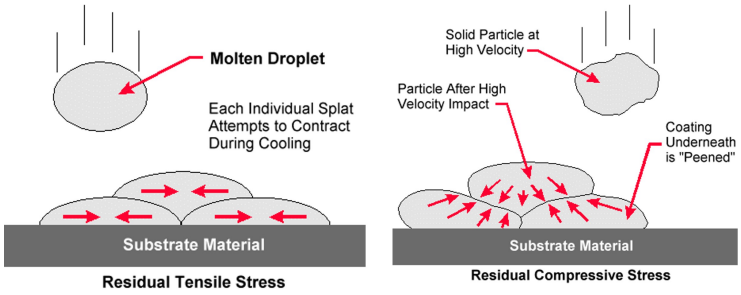

Figure 2.16: Tensile quenching stress and peening effect of high-velocity impact on residual stress in the coating [112]

The thickness of the coating can also result in lower residual stresses due to shot peening effects. Shot peening counteracts residual stresses with compressive stress such as seen in figure 2.16 [112]. A recent study performed measurements on cold sprayed Inconel 718 coatings ranging from 216 to 1173 µm thickness and found that the thickness significantly influenced residual stress. The study also found that the bond strength increased while the average residual stresses declined for the thicker coating [113]. Another study however found an opposite effect when spraying thicker coatings, due to higher moments from residual stresses in thicker coatings and edge effects from peeling forces it was concluded that thicker coatings lead to lower adhesion [15]. This difference in results is most likely

the result of process parameters and material properties, the exact origin however is not reported in the literature.

Surface roughness

The surface roughness of coatings is often associated with aesthetic properties but can also affect their performance. Mechanical properties such as wear resistance and friction coefficient are influenced by surface roughness but also corrosion properties such as pitting resistance and hydrogen permeation can be affected [114, 115]. There are several factors which have an effect on the degree of roughness such as splat formation, spray parameters and conditions, the particle size of the feedstock and substrate properties [116]. Spray parameters which have been found to influence the roughness were the angle of application due to unfavourable splat formation [117], the spraying distance, pattern and powder feed rate. The conditions which have been found to mostly influence roughness are related to temperature and velocity [118]. If a specific roughness is desired, changes can be made with post-treatment processes such as polishing, etching or heating [16].

2.6.2 HVAF instrument

There are two suppliers which offer HVAF instruments, named Kermetico and UniqueCoat. As UniqueCoat mainly operates in the United States, the AK07 system by Kermetico will be used as a reference. The instrument consists of several essential components which are schematically displayed in figure 2.17.

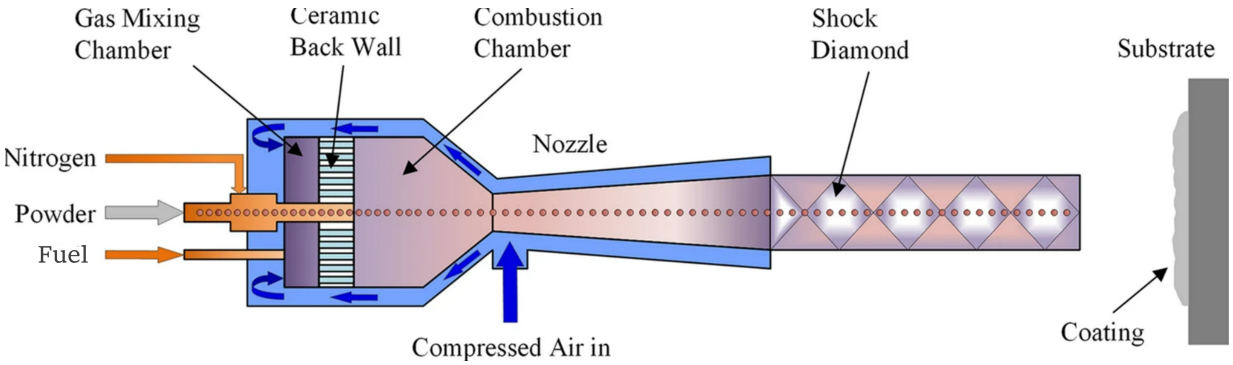

Figure 2.17: Schematic overview of the Kermetico AK07 HVAF instrument [119]

The instrument has four inlets from which compressed air, fuel, feedstock powder and nitrogen are fed into the instrument. Nitrogen is used as a carrier gas to transport feedstock, in the schematic it can be seen that the two inlets join before being introduced in the gun. The powder and gas are then fed coaxially with the cylindrical axis of the gun, which is different from for example the plasma and cold spraying instruments in figure 2.11 in which the powders are radially injected. Most new thermal spray techniques have adopted axial injection. Two significant benefits are that the particles are more effectively centred in the flame of the gun which enhances heat transfer, and secondly, particles are less affected by turbulence as they don't have to pass through the outer flanks of the flames. Both attributes ensure a higher deposition rate and efficiency [120].

One or a combination of fuel gasses and compressed air are brought together in a gas mixing chamber. Compressed air first flows around the combustion chamber in order to cool the gun nozzle and chamber. Propane is commonly used as fuel but other gasses such as hydrogen, propylene or natural gas have also been reported. The gas mixing chamber is separated from the combustion chamber with a ceramic insert. The insert has holes from which the mixed gasses can enter the combustion chamber. After initial ignition (usually with a startup sparkplug) in the combustion chamber, the ceramic insert heats up to auto-ignition temperature. Gasses flowing through the holes are thus automatically re-ignited when introduced in the combustion chamber [9]. Re-ignition through this method allows for stable operation of the process and is often referred to as activated combustion or AC-HVAF.

The axially injected nitrogen and powder mixture is heated in the combustion chamber by the combustion products of the ignited gasses. Uniform velocity and temperature in the chamber from activated combustion and high pressure allow gradual heating of the feedstock powder [121]. The pressure depends on combustion chamber dimensions, nozzle and process parameters. Typically a combustion chamber pressure of 0.45 to 0.56 MPa is obtained [9]. The mixture of gasses and heated particles then enters the nozzle from the combustion chamber. The nozzle, which is usually converging/diverging (De Laval design) is capable of reaching supersonic speeds and can be used to control the pressure and particle speed [122]. The mixture is accelerated to a sonic gas flow in the converging section and reaches a super-sonic flow in the diverging section from which it exits the nozzle [123]. The schematic in figure 2.17 does not correctly show this De Laval design, a more accurate illustration is shown in figure 2.20. A typical phenomenon which occurs when a supersonic flow exits a nozzle is the formation of shock diamonds. Upon exiting the nozzle, shock waves are formed due to an abrupt change in pressure [124]. The pattern is a result of a series of compression and expansion waves. The temperature and pressure increase in compression while it decreases in expansion. The waves dissipate due to turbulent shear at a certain distance from the nozzle at which the temperature and velocity rapidly decrease [125].

2.6.3 Spray parameters and instrument configuration

Adjustments in the process are an important part of the thermal spraying process. The parameters and gun can be configured for the intended application. Optimizations are often made to obtain desirable coating properties but also to increase efficiency or deposition rates. These adjustments have a complex relation with each other and nonlinear effects and therefore parameter studies are often conducted to identify whether desired properties are attained [16, 119]. For many applications, desirable parameters and configurations are known from previous research. Regardless it remains an important aspect of thermal spraying research and thus their effects are described in the following section.

Feedstock and particle size

Before feedstock can be ejected from the nozzle it has to be fed through and heated in the thermal spray gun. These feedstocks are used primarily in the form of wires, rods and powders. As was concluded in the previous chapter, wire arc techniques exclusively use

wires or rods while the feedstock for HVAF is predominantly in the form of powder. This study will therefore focus on the use and effects of powdered coating material.

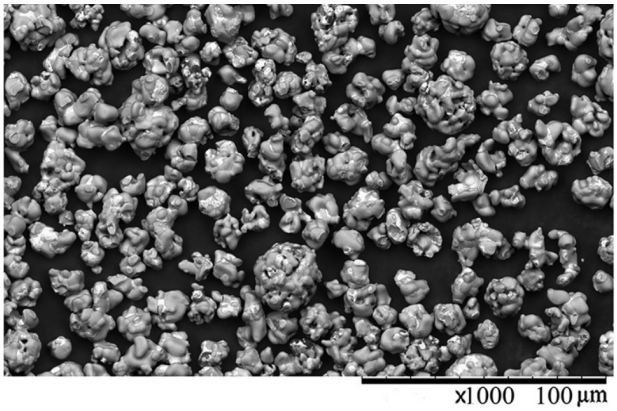

Figure 2.18: SEM micrograph of powder feedstock Cr_2C_3–NiCr with a variation of particle size [126]

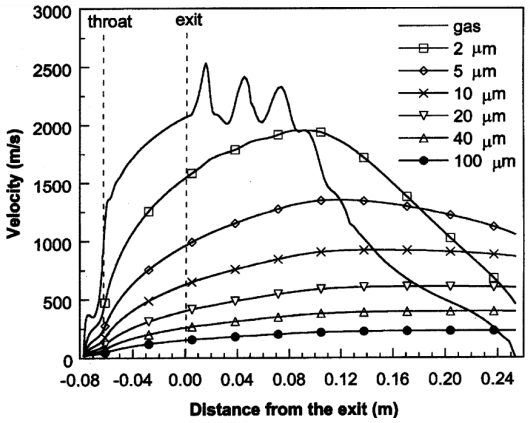

Figure 2.19: Powder size and velocity relation at various distances from the nozzle [127]

The size of these powders is usually in the range of 10 µm to 110 µm, manufactures offer size ranges where the smallest and largest particles typically differ 30 to 40 µm in size. These differences are well visible in SEM micrographs, as can be seen in figure 2.18 for Cr_2C_3–NiCr powder [126].

The size of the particles has a significant effect on the process in terms of particle heating and velocity. Longer heating times are required before larger particles are fully molten which can result in a particle stream with a mixture of molten, semi-molten and solid particles. Smaller particles are heated quickly but also solidify faster. A similar trend occurs for velocity as larger particles require a longer time to reach high velocities due to their respectively higher mass. Smaller particles accelerate quicker but have a faster decline in speed at high stand-off distance [127]. This relation is evident from figure 2.19 [127]. As explained in section 2.6.1 the particle temperature and speed are two of the most important properties which influence coating quality. Additionally, the size of the particles has a direct effect on the formation of coatings. Finer particles with a small diameter produce coatings with low surface roughness and generally lower porosity from microstructures with smaller splats [128].

Gas flow rate

As explained, fuel gasses are injected into the combustion chamber to be used as the source of power. The amount of gas which passes a certain point in a certain time is referred to as the gas flow rate, usually this is measured in litres per minute (LPM) or cubic meters per hour (CMPH) [16]. It is an important parameter as it influences not only the energy input but also particle velocity. High gas flow rates generate more power for thermal spraying [129]. A recent study found that the H_2 flow rate in air plasma sprayed Metco 16C (a type of Ni-based superalloy) could be used to optimize coating quality for sour environments. It was furthermore found that with increasing flow rate the hardness and wear resistance increased and the polarisation resistance and unmelted fraction decreased [77]. Gao et

al. found that the flow rate of carrier gasses can also affect the heating of the powders. Reducing carrier flow rates increases the time for heat to transfer to the particles. A high carrier gas ratio compared to combustion gasses decreases the flame temperature. A significant effect of the carrier flow rate on the particle velocity was however not found [130].

Powder feed rate

The powder feed rate can be controlled to increase or decrease the amount of particles which are injected in the thermal spraying device and is controlled by the carrier gas flow rate and particle size distribution. The minimum rate is dependent on stability as low rates can cause oscillations, the highest rates possible rely on the maximum amount of particles which can physically be fed through the transporting pipe. A high spray rate should be avoided as it can cause the nozzle to become blocked and lead to damage to the instrument [16].

logically, a high powder feed rate increases the amount of particles which are simultaneously released from the gun and thus increases the deposition rate and efficiency. As explained in subsection 2.6, HVAF is capable of maintaining a high quality at high deposition rates. A negative impact of high rates is however that fast successive impingements of the particles can result in excessive residual stresses in the coating [53]. This is caused by a rise in the temperature of the substrate when too much material is deposited on the substrate in a certain given time [131]. Additionally, high deposition rates may have a negative influence on splat formation, particles that don't have enough time to solidify may not provide a sufficient layer for successive impingement, which may thus result in unfavourable formation of the coating structure [132].

Nozzle design

As explained in the previous section, the nozzle is the part of the instrument where particles are accelerated and from which a supersonic flow is ejected. An important aspect of the nozzle design is the ratio between the exit and throat diameter, the length and shape. A longer nozzle is often used to obtain long dwell times while a smaller sized nozzle exits are used to increase the temperature of the molten jet [86]. A typical 'De Laval' nozzle design for HVAF equipment can be seen in figure 2.20.

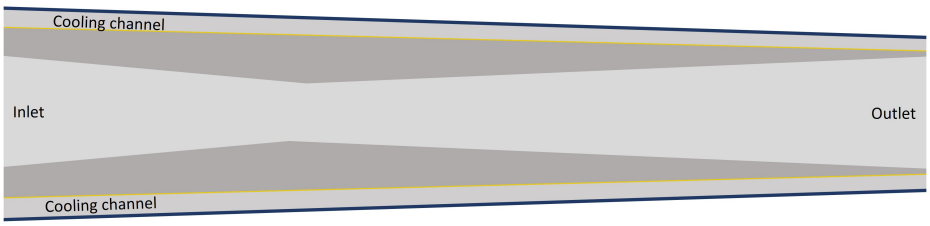

Figure 2.20: Typical nozzle design which is used for HVAF equipment (adapted from [86])

Cooling channels on the nozzle are used to effectively transfer the heat in the nozzle wall. Insufficient cooling of the nozzle can cause a reduced life time of the equipment and most importantly result in local turbulent flow in the jet. A laminar flow of the jet is desired to reduce drag. By using the ideal water velocity of the cooling water, the efficiency and lifetime of the nozzle can be improved [133].

Orientation, position and movement

The orientation, position and movement of the spraying gun can have a significant effect on several aspects of the coating. Research on coatings is often conducted on small metal samples which are sprayed in optimal conditions. Spraying guns attached to robots are optimized to achieve a constant spray distance, angle, cycle number and velocity relative to the substrate. This ensures that a constant thickness and uniform coating quality is obtained [134]. When spraying in confined spaces or on uneven surfaces it may be difficult for the operator to maintain a constant angle and distance from the substrate. It is therefore important to consider what the effect would be with respect to coatings applied under optimized environments. Important effects to consider are the distance at which the coating is applied, this can affect the velocity and temperature at which the particles arrive at the surface[135]. Leigh et al. [136] found that off-angle thermal spraying at angles which varied between 50 and 90 negatively influenced the performance of the coatings. As the angle increased, the micro-hardness, adhesion strength and fracture toughness decreased while porosity increased.

The lateral movement speed of the gun may influence oxidation between the sprayed layers. A coating consists of multiple layers which are sprayed on top of each other until the desired thickness is achieved. Before a successive layer is sprayed there is time for the surface to oxidize. A high lateral movement results in thinner individual layers than when it is sprayed with a slow lateral movement. Obtaining the desired coating thickness with high lateral movements thus requires more layers with surface oxidation [137].

Surface preparation

Proper preparation of the surface is crucial as it can influence adhesion, mechanical properties, corrosion behaviour and coating morphology. To enhance adhesion through mechanical interlocking, which was described as the adhesion mechanism between thermal sprayed coatings and substrate, it is necessary to increase the surface area through roughening of the substrate [138].

Certain steps should therefore be performed, the first of which is cleaning the surface of a substrate. This procedure should be conducted according to EN 13507, which is the European standard for pre-treatment of metal surfaces for thermal spraying. It is important that the surface is free of oxides, oils and other contaminants as this affects the adhesion and corrosion performance of the coating. The EN standard describes that the surface should be degreased with a washing solution and cleaned with a mild alkaline phosphate with high surfactant content.

After the substrate is decontaminated and cleaned, it can be roughened by grinding or grit blasting. A purity grade Sa3 should be obtained as described in ISO 8501-1 and roughness as described in EN22063. There are several types of abrasives which can be

used to roughen the surface. Examples are SiC and quartz sand, it is especially important that the abrasives are clean and unused, care must also be taken that abrasives and dust must be removed after with e.g. compressed air. A post-check according to ISO 12944-4 and EN 22063 should make sure that the purity and roughness of the surface are sufficient.

2.7 Thermal sprayed coatings for HIC prevention

In order to protect carbon steels in a sour environment against corrosion and most importantly HIC, it is essential to understand what coating properties are desired and which materials are most compatible with the environmental conditions and environments [139–141]. Furthermore, there are general requirements which should be considered such as economical feasibility, health and safety standards [85, 142]. This section will discuss these requirements and thoroughly explain how these properties are related to the performance of the coating.

2.7.1 Corrosion protection

The principle function of a coating is to form a barrier which is capable of protecting a substrate from a medium containing corrosive substances. For the purpose of protecting against HIC, the coating should thus function as a physical barrier which is impermeable to hydrogen sulfide and dissociation products, but also to other corrosive contaminants which were discussed in section 1.1 [139, 143]. Generally, this means that a coating should be made of a corrosion-resistant material but it should also be produced so that it is uniform and free of defects. In order to produce such a coating, careful consideration must be given to the influences of the coating material and application method. As was explained in the previous section, thermal sprayed coatings are often characterised by their non-uniformity but also by voids, pores and diffusivity paths. It is important that a thermal spray technique is used which is capable of eliminating these defects as much as possible. Furthermore, the choice of material is important as certain materials may be more porous than others by nature or have a higher tendency to oxidize [144].

Diffusion and permeation

To understand the functionality of a corrosion barrier is important to explain the mechanism of permeation and diffusion. Diffusion of hydrogen as interstitial through the metal lattice was already described in section 2.2, where the atoms move primarily through tetrahedral sites to move in the body of the material. A quantification can be made for diffusion. Fick's law can be used to approximate the speed at which molecules or atoms migrate through the medium. The equation is based on Fick's second diffusion law and written as [145]:

$$\frac{\delta c}{\delta t} = D \frac{\delta^2 c}{\delta x^2} \tag{2.22}$$

Here the concentration is given by c(x,t) and the coefficient for diffusion by D.

The diffusion coefficient can be approximated with the equation:

$$D = D_0 \, exp(-\frac{Q_d}{RT}) \tag{2.23}$$

In which D_0 is the diffusion constant, Q is the activation energy for diffusion, T is the temperature in Kelvin and R is the gas constant (8.134 J/mol K) [145]. While the equations are convenient for comparing diffusion rates for different materials, it is important to realize that the diffusion coefficient is not always constant throughout a body of a material, especially in thermal sprayed coatings. Diffusion often takes place in high-diffusivity paths such as grain boundaries, voids, porosities, dislocations and microcracks, where rates are higher than in the lattice [146]. This is due to the fact that the mean jump frequency is higher in these regions [145].

Besides diffusion, it is important to consider the mechanism of permeation. The difference is that diffusion describes the internal movement of molecules or atoms within a material and permeation represents the overall process of molecules or atoms passing through one side of a membrane (or in this case a coating) to the opposite side. This means that diffusion through a material only takes the internal process into account while permeation also considers the effect of recombination on the surface, desorption, adsorption, dissociation and solubility [147]. Permeation may therefore also include the effect of for example surface roughness of a coating. A rough surface has a larger surface area for adsorption and absorption of hydrogen and thus results in higher permeation [148, 149]. Furthermore, it is also important to consider the diffusion and permeation of different types of species. Not only permeability to hydrogen should be considered but also for H_2S, HS^- or S^{2-}. A study from 2020 by Wu et al. [150] showed that HS^- ions easily diffuse through coatings in sour gas environments and lead to blistering due to hydrogen formation between the iron substrate and coating.

2.7.2 Erosion and wear resistance

Erosion corrosion and wear of coatings is caused by the interaction of solid, liquid and gas particles in a flowing liquid or vapour. This type of corrosion is especially harmful to the integrity of metals if the medium is corrosive. Erosion through solids occurs when small hard particles which are abrasive to the coating cause solid particle impingement. Sand or particles which have come loose from equipment may for example be present in the process stream. Additionally, two special types of erosion corrosion are liquid impingement corrosion and cavitation erosion. Although the origin of these two is different, the damage they cause is identical [151]. Liquid impingement occurs when small liquid drops are accelerated towards the coating and cause high contact pressures, damage is caused by the initial load to the surface from the impact of the droplet and the shear force which is exerted on the surface when the liquid rapidly flows away from the point of impact [152]. This lateral flowing water can achieve speeds which are ten times higher than the initial impact and cause pitting when it encounters asperities on the surface, this process is schematically shown in figure 2.21. Cavitation occurs in low-pressure zones when a liquid transforms into vapour and implodes when a high-pressure region is reached. The imploded bubbles cause micro-jets similar to liquid impingement jets at the solid surface which then again cause erosion damage [151]. The degree of damage is related to the

properties of the eroding particles in terms of size, shape, density, composition, angle of impact and velocity, but also on the properties of the material which is being eroded [153]. An example where erosion results in a material loss in the form of pitting can be seen in figure 2.22.

Due to the continuous impingement of solid particles, drops or jets, local strain hardening at the surface causes an increase in yield strength up to a point where further deformation is no longer possible. This means that the material becomes brittle and may fail from pitting or cracking. In environments where impingement is a problem, it is therefore necessary that a material has the ability to absorb the energy of such impacts [153]. Most existing theories concentrate on the hardness and Young's modulus of materials to define their resistance to impingement, as they can be used to predict their resistance to plastic deformation [154]. High-hardness materials are thus often chosen for equipment which should resist erosion.

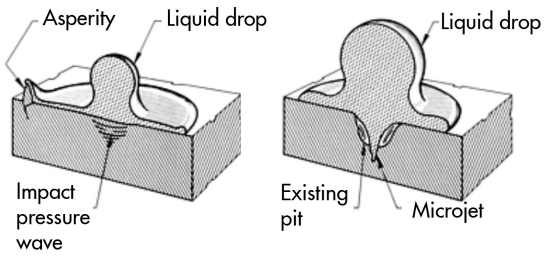

Figure 2.21: Liquid impingement and lateral jetting after impact [155]

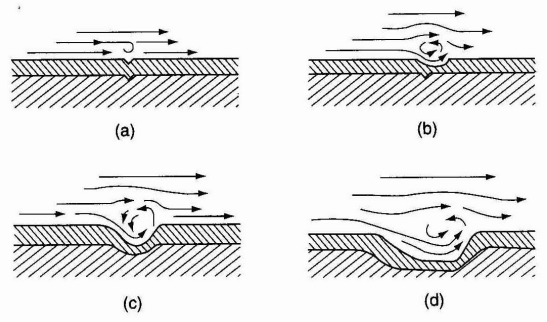

Figure 2.22: Mechanism of erosion-corrosion on a coated surface, reulting in pits [156]

Besides the obvious requirement that coatings do not exhibit loss of material through erosion, it is essential that such coatings remain intact to prevent galvanic corrosion through the coating and underlying substrate, as explained in the previous subsection.

2.7.3 Adhesion

Adhesion refers to the bonding between a coating and a substrate. When such a bond fails the coating can delaminate and expose the metal surface or result in voids at the interface where corrosive products can accumulate [157]. Good adhesion is thus necessary, it can be achieved through various adhesion mechanisms such as adsorption, chemical bonding, electrostatic attraction, interdiffusion and mechanical interlocking. Adhesion can often be enhanced by adding substances such as primers, surface preparation or by considering in advance how the substrate reacts with certain coatings. Thermal sprayed coatings mainly adhere to the substrate through mechanical adhesion, this type of adhesion is established by physical interaction of the coating and the substrate through interlocking. The coating must flow in between the surface irregularities and pores of the substrate which function as anchoring points. To obtain strong adhesion it is therefore required that the substrate has a high and favourable contact area, usually achieved from a high surface roughness with proper contact angles (figure 2.23)[158–160]. Additionally, adhesion is improved by

the combination of other adhesion or bonding principles. Although mechanical bonding is the main adhesion mechanism in thermal sprayed coatings, metallurgical bonding and diffusion bonding can have a small but positive effect on adhesion strength [100, 161]. A clean surface with low oxygen and contamination is therefore desired [160].

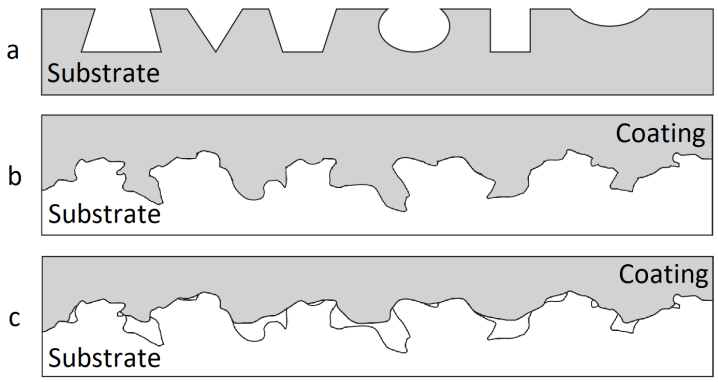

Figure 2.23: (a) Various geometries of surface roughness (b) optimal contact between substrate and coating (c) insufficient flow leading to cavities (adapted from [162])

2.7.4 Temperature and pressure cycles

Internal coatings may be prone to high strain levels due to thermo-mechanical stresses and a mismatch in the thermal expansion coefficient between the substrate and applied coating. An example for which this is especially relevant is the use of coatings in high-pressure vessels [163]. When a coating can not resist thermal cycles and/or combinations of mechanical loading, the coating could easily fail from disbonding or cracking. An indication of applicability can often be obtained from the difference in thermal expansion of the substrate and coating, which is the reason why ceramics are not always suitable [164, 165].

2.7.5 Coating thickness

The thickness of coatings is an important property, it is necessary that enough surface is covered and that it offers protection. Thin coatings have the benefit that application requires less time and reduces material costs. Thicker coatings have the advantage of better corrosion protection properties due to reduced through-coating porosities and in the case of sacrificial coatings a longer lifetime [16]. There are however problems that can arise as the thickness of coatings increases. One significant property which has been found to decrease is the bond strength. In thermal sprayed coatings this effect arises from residual stresses which are introduced when the coating contracts from cooling. Such stresses create moments on the interface of the substrate and coating which thus increase in thicker coatings. Additionally, shear and peeling stresses near edges of coatings increase from thicker coatings as the area which is subjected to stress, is enlarged [15]. This may however be resolved in certain cases by the effect of shot peening. Thermal spraying techniques can obtain high particle velocities, which causes compressive stresses to counter tensile cooling stresses [113].

It is important to note that variations in these effects exist due to variations in the properties of coating materials. Ceramic coatings for instance have other thermal expansion coefficients than metal coatings. Variation also exists in application methods. A technique such as chemical vapour deposition is able to achieve more uniform coatings with less residual stresses than coatings applied with thermal spraying [53].

2.7.6 Health, safety and environment

The risks of using certain materials should not be underestimated, coatings can have hazardous side effects. Such hazards may include the release of harmful primary or secondary substances during and/or after application, they may for example be released in the air or in the process stream. A coating type which has attracted a lot of attention in recent years is hexavalent chromium. Although it has excellent performance to protect against corrosion, many studies are focused on replacing it. Workers who have frequently come in contact with the material developed lung cancer at higher than normal rates. Eventually, this has led to research dedicated to the potential health hazards of using hexavalent chromium [166]. Despite the known danger of inhaling chromium compounds, it was unknown that ingesting it would also be carcinogenic. Contaminated drinking water in the United States where the concentration was regulated at 50 µm g/L resulted in excessive risk of cancer in a community in California [167].

As these examples prove, safe handling and ensuring that substances are not released where it should not be intended is important. Hazardous substances may in certain situations still be used if personal protective equipment during application is used, and threats to the environment are removed. The takeaway should be that selecting a coating comes with a certain responsibility which should not be taken lightly.

2.7.7 Financial feasibility

As was explained in section 1.1 the financial damage of corrosion is an incentive to make use of coatings. Coatings are mostly chosen on the basis of payback time and their return on investment. It is therefore important to make trade-offs in terms of feasibility and reliability. An excellent but costly coating may not have the financial advantage over replacing equipment with corrosion-resistant alloys [168]. In order to make such trade-offs it is necessary to consider materials costs, the speed at which the coating can be applied, the required passes, loss of production time, material costs and equipment costs but also the lifetime of a coating and its functionality [169].

2.7.8 Resistance to cleaning

Equipment requires mandatory periodic cleaning and inspection. During these so-called plant turnarounds, the operating environment is different than normal, equipments are decontaminated and cleaned to perform necessary maintenance. A manual for these activities is provided by the company which thoroughly describes these processes for each category of units in refinery plants. Heavy oil equipment requires different decontamination and cleaning than lighter hydrocarbon vessels. For this study, it is important to consider general requirements and requirements for vessels which contain H_2S. Typical agents and

methods for cleaning equipment include the use of mechanical-, chemical-, detergent-, hot water-, emulsion- and solvent cleaning. Additionally, general guidelines state that cleaning fluids need to be hot (approximately 80 to 120 °C).

H_2S-containing vessels require a special decontamination process where organic materials are first removed by steaming, alkaline washing or detergent washing to clean the surface of vessel walls, trays and deposits. The remaining contaminants are then washed away with acid or chemical oxidation, and at last, H_2S is removed by rinsing or steaming. For metal coatings especially these alkaline and acidic washes are important to consider as they are usually very corrosive. Besides the processes described above there are many other maintenance, cleaning and inspection steps, it is however not in the scope of this study to discuss all of these [170].

Table 2.2: Requirements for coating, compatibility with the environment and possible damage which may be induced

Service environment	Coating requirements	Possible damage
Chemical exposure	Permeation resistance	Embrittlement
Pressure and stresses	Good adhesion	Local defects
Temperature cycles	Temperature resistance	Delamination
High fluid velocity	Low friction coefficient	Wear and erosion
High and low pH	Corrosion resistance	Leaching or Depletion

2.7.9 Coating Material

While a variety of different materials can be used for thermal spraying, the scope of this study is on metallic and cermet-type coatings due to their excellent lifetime, corrosion protection and mechanical properties. A distinction can be made for these coatings between sacrificial and non-sacrificial coatings. Respectively, these materials have a higher electrode potential or lower potential than the substrate [22]. Essentially the primary function of both coatings is identical as they form a barrier between the corrosive environment and the substrate. However, in the case that the coatings are breached there is a significant difference in corrosion behavior. Metals can form a galvanic couple in a corrosive environment which causes galvanic corrosion [171]. Galvanic corrosion is a type of corrosion which occurs due to the electrochemical potential difference between a metal and another conducting material. When two dissimilar materials are brought together in an electrolyte a corrosion reaction occurs. The material with a low potential acts as the cathode and the material with a high potential as the anode, the corrosion rate of this reaction depends on the potential difference between the two materials, environmental effects, electrolyte properties, metallurgical factors, surface conditions and geometric factors. Since the least noble material behaves as a cathode it will preferentially corrode, this property can be used to protect the substrate [172].

For coatings which are nobler than the substrate the opposite happens, in the case of a breach the coating will promote corrosion of the metal on which it is applied, schematically this is portrayed in figure 2.24.

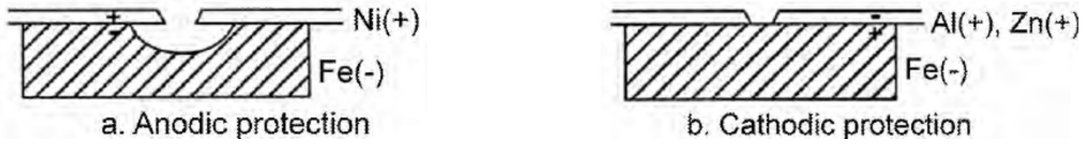

Figure 2.24: (a) Anodic protection with non-sacrificial coating (b) Cathodic protection with sacrificial coating [85]

While this is a serious disadvantage of non-sacrificial coatings, there is also a serious shortcoming of using sacrificial coatings to prevent HIC. Galvanic corrosion of sacrificial coatings is paired with the formation of hydrogen and a high flux of hydrogen at the substrate, especially with large potential differences between the protective film and substrate. Cathodic protection is therefore associated with an increased risk of hydrogen embrittlement [173]. The selection of either sacrificial or non-sacrificial coating should therefore principally be based on their ability to act as a barrier and corrosion resistance since both have a significant effect on the corrosion of the underlying substrate.

Sacrificial coatings

Aluminium and zinc are two materials which are frequently used as sacrificial anodes to protect metal structures and equipment. Zinc is however very susceptible to corrosion in acid environments and forms porous and brittle sulfide compounds in H_2S which do not passivate the coating [68]. A recent study showed that thermal sprayed zinc coatings are not fit for use in H_2S environments while aluminium has shown better results [174].

Thermal sprayed aluminium (TSA) coatings are often applied in off-shore steel structures as they offer long-term protection and can act as a sacrificial anode. Aluminium alloys may also protect steel in sour environments as they are less susceptible to embrittlement [68]. Furthermore, it is not reactive with H_2S, meaning that no metal sulfides form, and has a low permeability to hydrogen. Aluminium has excellent corrosion resistance in pH intervals of 4.0 and 8.5 due to its passive oxide layer, outside this range the corrosive processes are dependent on constituents of the environment [175].

A recent study [10] tested the effect of TSA coatings on SSC and HIC resistance of high-strength steels in a sour environment with the TM 0177 NACE four-point bend loading test, the industry standard for testing susceptibility to SSC. Coatings with a thickness of 250 µm and porosity which ranged between 5 to 8% without interconnected pores or through thickness flaws were applied on steel wire samples. Tests were performed on a sample without coating, fully coated and coating with an intentional defect of 2 mm. The uncoated sample failed, and internal cracks were found with ultrasonic imaging in the loaded and unloaded samples and therefore were identified as HIC. Both the coated samples showed clear signs of corrosion, however cracking and pitting were both absent. Protection against sulfide stress cracking was attributed to the protection of the substrate

from pitting and the barrier effect. Furthermore, the study stated that HIC was hindered by the TSA coatings, however, there was uncertainty about the impact of the high surface roughness and porosity arguing that they might boost hydrogen diffusion. Furthermore, it was unclear if the test was long enough to concentrate enough hydrogen in trapping sites. The author also concluded that due to cathodic reactions hydrogen accumulation and diffusion into the substrate will eventually lead to HIC and thus the use of TSA might not be an optimal solution for long time usage. Another study conducted by Kane et al. [176] reviewed the performance of TSA in environments with H_2S, ammonia, chloride, cyanide and variations in alkalinity and acidity to protect steel equipment from HIC. Aluminium showed excellent corrosion resistance in pH intervals of 4.0 and 8.5 due to its passive oxide layer. The study found that the coating corroded severely in environments with a high pH while in acidic sour environments at pH 2.7 the corrosion rate was much lower. Furthermore, the presence of cyanides increased the corrosion rate.

Non-sacrificial coatings

Because non-sacrificial coatings can lead to an accelerated corrosion reaction of the underlying substrate they are often avoided in engineering applications. They can however still be a great solution in certain cases as they have excellent corrosion resistant properties in various corrosive environments. A difference is made between severe applications and critical applications in which respectively high alloyed steels and Ni-based alloys should be applied. Nickel alloys are characterized by their high performance and corrosion resistance. Cr, N, Mo and W are frequently alloying elements, NACE describes in the MR0175 standard [67] that the resistance to pitting can be predicted with pitting resistance equivalent number (PREN) for CRA. The equation, where the mass fractions of the elements w_{Cr}, w_{Mo}, w_W, w_{Cr}, w_N are presented as a fraction of the total mass composition is given by [13]:

$$PREN = w_{Cr} + 3.3(w_{Mo} + 0.5w_W) + 16w_N \tag{2.24}$$

Especially molybdenum and chromium are often added to Ni-base alloys to improve their properties. As explained in subsection 2.6.1, the stable passive oxide layer which forms on Cr can provide additional resistance in corrosive environments. Additionally, Mo is often added to increase the resistance to pitting and crevice corrosion [177]. Even though there is only a limited amount of research on the resistance of these thermal sprayed alloys in sour environments, results from several recent articles are promising [12, 13, 83, 178, 179].

Besides coatings with predominantly nickel, coatings with a high content of chrome have been extensively studied for severe environments in the petroleum industry. One excellent material, 316L stainless steel, has been proven to be a good corrosion barrier when applied with HVOF spraying in applications such as pressure vessels, valve components and tubing for gas wells. Moskowitz found that ultracoat HVOF sprayed 316L applied on carbon steel sulfur condenser heads after 18 months of service were still in excellent condition [83]. Stainless steels in sour environments have good corrosion resistance due to their passive film. Cheng et al. [180] found that acid solutions which contained H_2S almost had no influence on the passive state of chromium. Wang et al. [180] found that this passive film exists due to the formation of Cr_2O_3 and CrO_3. Besides Cr, 316L consists of other

alloying elements such as Mo and N. Besides 316L, other stainless steels such as Duplex 2205 are mentioned in the literature. Type 2205 is a CRA with mixed austenite and ferrite crystals and a high content of chrome, nickel and molybdenum. A study by Shah et al. [181] compared 316L and duplex 2205 in the presence of high partial pressures of H_2S. The study found that type 2205 showed higher resistance to both pitting and general corrosion owing to its higher content of chrome and nickel, with chrome passivating the surface and nickel forming protective oxide and sulphide compounds. Furthermore, the study found that both steels had the highest corrosion rate and pit penetration rates at 3 bar of partial pressure H_2S.

Hydrogen diffusion in HVOF thermal sprayed 316L steel was investigated by Moshref-javadi et al. [148]. In this article, the author explains that due to an increased amount of reversible and irreversible traps due to the nature of the ferritic phases in the thermal sprayed coating, the hydrogen diffusion coefficient was found to be close to that of ferritic steels. As explained in section 2.1, austenitic steels offer a lot more resistance against hydrogen diffusion. It was concluded that the type 316L coating is capable of resisting hydrogen diffusion and permeation but had a low efficacy compared to normal dense stainless steel layers.

A study by Shiladitya [12] in 2015 compared 316L and two Ni-based alloys (C-276 and 625) applied with HVOF. The three alloys were all capable of protecting the steel from CO_2 and H_2S corrosion, providing a cost-effective and excellent coating against corrosion. The condition is however that through-coating porosities are eliminated or avoided to prevent galvanic corrosion with the underlying substrate. These galvanic effects were studied with an artificial holiday in the three coatings, the effect of which can be seen in figure 2.25. The author concluded that the 316L coating showed more porosity and furthermore questioned its long-term performance at 40 °C as it showed local delamination on the surface. Figure 2.26 shows that C276 has a higher density than 316L HVOF sprayed coatings.

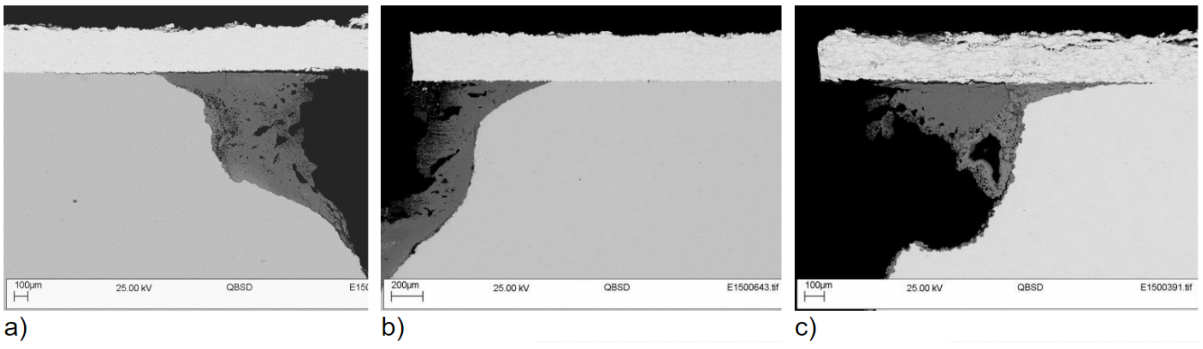

Figure 2.25: Three coatings in H_2S and CO_2 environment with holiday, from left to right alloy C276, 625 and 316L [12]

From the studies mentioned in this section, it can be concluded that Fe-based coatings which contain a high amount of chrome can be used as a corrosion corrosion-resistant coating and provide a barrier to prevent HIC and SSC. Studies which have been performed are however mainly focused on type 316L stainless steel [12, 83, 148]. There might therefore be other stainless steel which are more fit for long-term use.

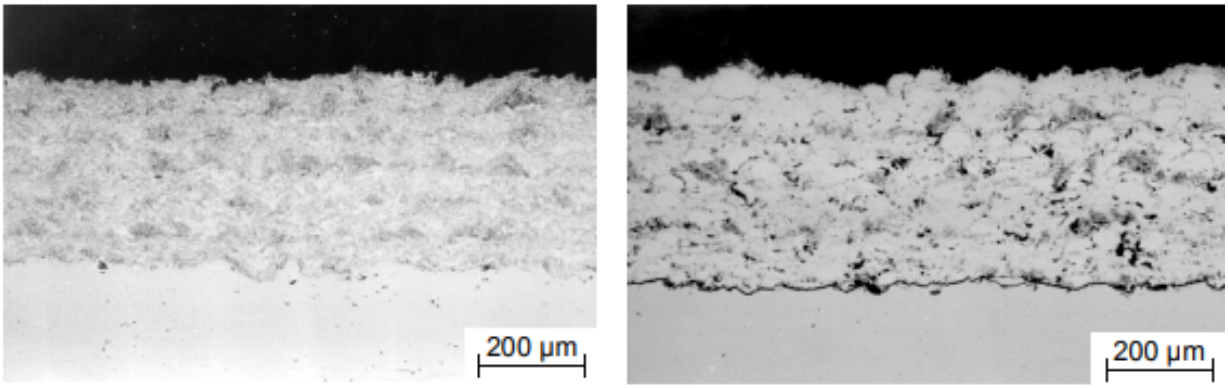

Figure 2.26: Coatings sprayed with HVOF, left is Hastelloy C276 and right stainless steel 316L [182]

Another class of materials that can be thermally sprayed are cermet coatings, which are a blend of hard ceramic (metal-oxides) and soft metal matrix [183]. Tungsten carbide (WC) based coatings are a commonly used alternative for hard chrome plating. They have excellent properties in terms of abrasion resistance, corrosion resistance and durability in high-temperature environments [184]. A binder is however necessary since pure tungsten carbide does not offer enough corrosion resistance to be used as is, additional elements such as Co, Cr, Ni or C are therefore introduced. Galvanic corrosion of micro constituents in the coating is however commonly detected, introducing Cr_2O_3 helps passivate this micro galvanic corrosion mechanism [180]. Tungsten carbide-based coatings are used in the oil and gas industry for equipment which is subjected to severe wear as it is extremely hard. This is also one of the downsides of using these coatings, due to their brittleness they are relatively prone to breaking or cracking when subjected to impact. Furthermore, due to the limited thermal conductivity, it is not suitable to use these coatings in high-temperature or thermal cycling applications. The greatest disadvantage is that the corrosion resistance is lower compared to Fe-based and Ni-based coatings [185].

2.7.10 Conclusion

As is evident from section 2.7.9 there is a variety of coating materials which are eligible for use in sour environments and for the prevention of HIC. From the articles which were discussed, it became clear that sacrificial coatings are not fit as they have a high probability of promoting HIC due to hydrogen charging. Furthermore, non-sacrificial CRA coatings thermal sprayed coatings were shown to have promising results due to their exceptional corrosion resistance and properties. Iron and nickel-based coatings are particularly of interest. Additionally, it was shown that both types are compatible with HVAF, which is crucial for obtaining high-quality coatings [12, 13, 67, 77, 83]. Table 2.3 displays potential materials for this study and is used to compare their advantages and disadvantages. Two materials stand out from this analysis, C276 and 316L. While 316L scored least on corrosion resistance, it has a cost-effective over the other coatings [14, 100, 186]. C276 has the advantage over the other coatings in terms of superior resistance in H_2S environments and low probability of coating defects. Two articles mention that there are doubts about the long-term corrosion resistance of 316L in H_2S environments [12, 83]. While this would be

an excellent topic for further research, it is not within the scope of this thesis. Therefore, the coating material which will be used in this thesis is C276.

Material	Hastelloy C276	Inconel 625	316L	22Cr	Metco 505/ Metco 16C
Corrosion Resistivity (H_2S)	++	+	+/-	+	+
Erosion Resistance	+	+	+/-	+	+
Compatibility with HVAF	Yes	Yes	Yes	Yes	Yes
Cost-effectiveness	+/-	+/-	++	+/-	+/-
Effect on HSE	Minimal	Minimal	Minimal	Minimal	Minimal
Chance of Defects	++	+	+/-	+	+

Table 2.3: Material selection for use as spray material in the sour environment against HIC

2.8 Summary and Knowledge Gaps

The theoretical background reviewed the most important aspects of HIC by describing the mechanisms of hydrogen embrittlement, sour corrosion, trapping of hydrogen atoms, and subsequent fracture. Additionally, the susceptibility of certain carbon steel materials, the effect of environmental factors, and associated severity were discussed. Furthermore, the requirements of coatings in refinery applications in sour environments were explored in terms of chemical resistance, mechanical properties, and environmental resistance, from which the key demands could be established. Essential requirements were found to be related to corrosion, erosion, and wear restiance, bonding with the substrate, and cost-effectiveness.

Coatings sprayed with thermal spray techniques emerged as an alternative to current mitigation methods. These coatings have been proven to be cost-effective and practical while possessing outstanding mechanical properties and corrosion resistance. A wide range of techniques and materials were subsequently discussed. It was found that high velocity air fuel (HVAF) coatings exhibit extremely low porosity and particle oxidation, both crucial properties to obtain corrosion-resistant and defect-free coatings [9–13]. $Ni_{57}Cr_{15}Mo_{16}W_4$, better known in the industry as Hastelloy C276, emerged as the most suitable material due to its excellent resistance to sour environment, mechanical properties and compatibility with HVAF [12, 13, 67, 77, 83]. Despite the great potential of HVAF thermal sprayed NiCrMoW coatings, the capability to prevent HIC in carbon steels and the exact behaviour in sour environments has not been investigated.

It is not clear from the literature what the optimal thickness of HVAF-sprayed corrosion coatings should be. There is a consensus that thicker coatings have a negative impact on the microstructure of the coatings, and most importantly that residual stresses increase. Additionally, the application of thinner coatings has financial benefits as application times

and material costs are reduced. Thicker coatings have the advantage that, from higher thermal input and shot peening effects, porosities are better-closed [15, 16, 113]. Additionally, thicker coatings act as a more substantial physical barrier, reducing the chance of impact fracture and erosion. These last two properties are especially important to prevent galvanic interaction. Due to the difference in corrosion potential, galvanic corrosion poses a risk. It is therefore essential that the coatings prevent exposure of the underlying substrate.

2.9 Research questions

The primary objective of this study is to establish the effect of HVAF thermal sprayed NiCrMoW coating thickness on HIC resistance of carbon steel in sour environment. Four research questions are formulated to be investigated in this thesis:

1. What impact does the thickness of HVAF thermal sprayed NiCrMoW coatings have on its microstructure, defects, and properties?
2. Can HVAF thermal sprayed NiCrMoW coatings effectively protect carbon steel against HIC in sour environments?
3. What is the effect of coating thickness on the electrochemical behaviour of HVAF thermal sprayed NiCrMoW?
4. What is the impact of galvanic interaction between the NiCrMoW coating and the carbon steel substrate in a sour environment, and how is this influenced by coating thickness?

To answer these questions, the experimental part of this thesis should include an analysis of the microstructural properties, primarily from cross-sections of coatings with different thicknesses. This analysis should include assessments of porosity, residual stresses, oxidation and through-coating porosity. Immersion tests, to simulate real conditions in sour environments, should be conducted to determine the susceptibility to HIC and investigate galvanic interactions between the coating and the substrate. Furthermore, to gain a deeper understanding of the corrosion behaviour and relative differences of coatings with varying thicknesses, the electrochemical behaviour should be examined within sour environments or conditions that closely mimic them. The following chapters cover the experimental part of this thesis.

3

Materials and Methods

In this chapter, the preparatory steps are discussed which were required before testing and analyzing the coating. The first part discusses the materials which were used and the application of the thermal sprayed coatings. The second part describes the test methods, experimental set-ups and procedures which were used to prepare the samples.

3.1 Materials

The materials which were used in this thesis were obtained from different sources, as shown in table 3.1.

Material	Product designation	Supplier
NiCrMoW	Amperit 409.074	Flame Spray Technology
Carbon Steel	S235-JR	NLMK Clabeq
Glass flake vinyl ester acrylic co-polymer	PAKOR-Polyglass VEF	Pakor B.V.

Table 3.1: Materials which were used and obtained from external suppliers

The coating material for this study was Amperit 409.074 (Hastelloy C276 equivalent) NiCrMoW powder, it was obtained from Flame Spray Technology and manufactured by Amperit. The composition of the coating powder is described in table 3.2, the size distribution of the material was identified as 15 to 45 µm, which is the finest size commercially available for this type of coating powder. A fine size was chosen to obtain the highest possible density and coating quality, as explained in section 2.6.3.

	Ni	Mo	Cr	Fe	W	Mn	Co	V	S	C
wt. %	57	15-17	14.5- 16.5	4-7	3-4.5	1 [a]	2.5 [a]	.35 [a]	.03 [a]	.03 [a]

Table 3.2: Composition of Amperit 409.074, a = maximum amount

The carbon steel substrates of type EN 1.0038 Steel S235JR+AR were provided by K. en W.A. Van Rooijen B.V., and manufactured by NLMK Clabeq. In section 2.3 it was described that carbon steels with high sulfur content (>0.001 wt%) are susceptible to HIC. Specifically, when these are hot rolled with a high combined wt% of manganese and sulfur. For this study, hot-rolled S235JR+AR steel was selected as it contained the highest quantity of sulfur. The metal was delivered as-rolled.

The chemical composition as displayed in table 3.3 is obtained from the inspection certificate in Appendix B. The yield and tensile strength of this type of steel were established to be respectively 300 MPa and 465 MPa. A total of 25 carbon steel samples were cut from the S235JR+AR plate in sections of 100x20x10 mm, 100x50x10 mm and 50x50x10 mm with the longest side in the rolling direction.

	Mn	P	S	C	Si	Al	Cu	Nb	Ni	Cr	V	Mo	Ti	N	Fe
wt. %	1.082	0.008	0.006	0.152	0.176	0.043	0.031	0.002	0.020	0.034	0.001	0.002	0.001	0.004	Bal.

Table 3.3: Composition of EN 1.0038 S235JR+AR carbon steel

For immersion testing, it was necessary to use a masking agent in order to protect the exposed uncoated sides of the carbon steel substrates with a polyglass coating. This masking agent was chosen as it has proven to be an excellent organic coating in sour environments. Application and necessary preparation before applying the agent on the sample were conducted at Pakor B.V. in Ridderkerk, which made these coatings available for the thesis.

3.2 Thermal spraying

A total of fifteen samples were sprayed in three batches of five samples in order to obtain three sets of samples with a coating thickness of 250, 375 and 500 µm. Each batch contained three samples of 100x20x10, one of 100x50x10 and one of 50x50x10 mm each. A clamping mount was used in order to hold five specimens simultaneously (figure 3.3). Before spraying, the substrates were grit blasted with F-20 silicon carbide (SiC) particles to obtain a cleanliness and roughness of at least SA2 to ensure mechanical interlocking. After gritblasting and just before thermal spraying the substrate surface was rinsed with isopropanol.

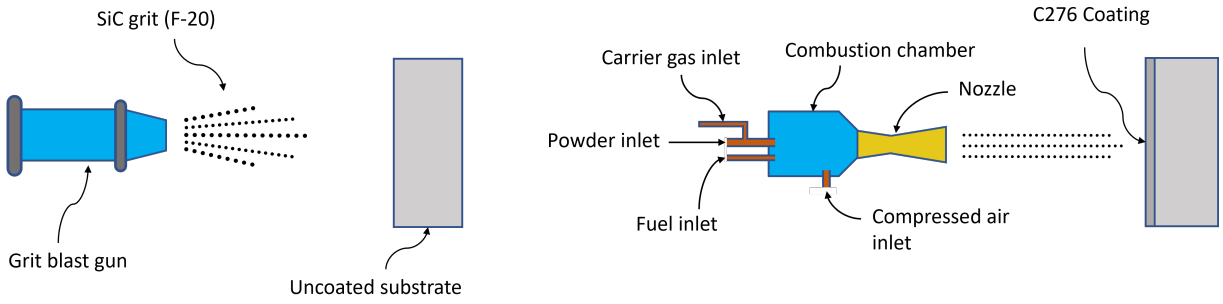

Figure 3.1: Thermal spraying and grit blasting process of the substrate

The HVAF instrument (AK07 from Kermetico) was used at the RWTH IOT research centre of the Technical University of Aachen (figure 3.2). The gun was mounted on an ABB IRB4600 robotic arm to ensure consistency for each coating run. Prior to spraying, a preliminary test was performed with the Amperit 409.074 spraying powder on a similar carbon steel substrate to obtain optimal parameters for the stand-off distance. These parameters were chosen and varied by trial and error. Other spray parameters were selected

Parameter	Unit	Value
Traverse velocity	mm/s	1000
Gun shift	mm	2
Spray distance	mm	250
Initial preheating of the surface	°C	65
Air pressure	MPa	0.66
Propane pressure	MPa	0.55
Powder feed rate	g/min	3.5
Carrier gas N_2	SLPM	37.2
Coating deposition per pass	µm	25-50
Minimum surface temperature before pass	°C	65 - 90
Maximum surface temperature after pass	°C	130

Table 3.4: Parameters used for thermal spraying

from a previous study performed by Kermetico and were held constant for each run (table 3.4).

The robotic arm was programmed to spray the samples by moving with horizontal translations to achieve a consistent coating on all samples, up and down movements were made outside the sample spray range. To achieve 250 µm coatings a total of twenty runs were necessary, for 375 µm 30 runs and for 500 µm 50 runs. After every ten runs the samples were cooled with compressed air to rapidly lower the substrate surface temperature. After spraying the thickness of the coatings was measured using a micrometer screw gauge, the thickness of the first batch ranged from 262 to 280 µm, the second batch from 372 to 380 µ, the last batch ranged from 498 to 549 µm.

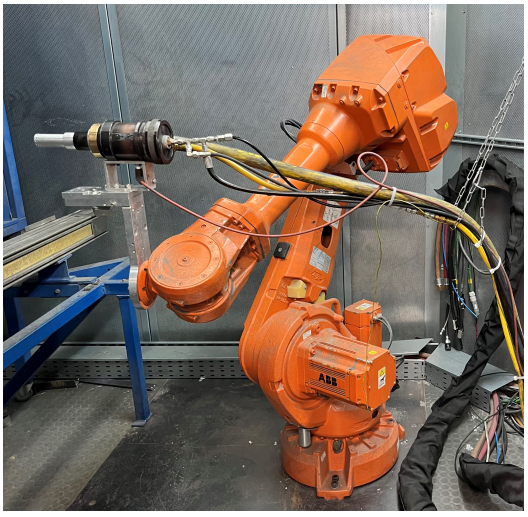

Figure 3.2: Kermetico AK-07 HVAF gun mounted on an ABB IRB4600 robotic arm

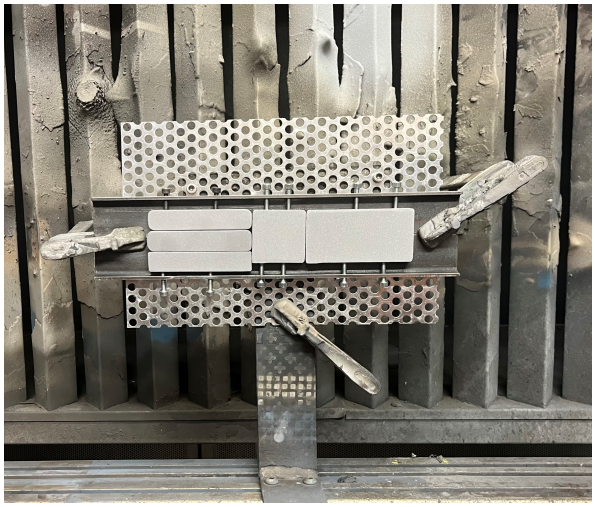

Figure 3.3: Sample holder for each batch of five samples secured with clamps

Properties	Amount	Masking	Coating thickness	Designation	Test type	Notes
Metallurgical properties	4	No	Without coating 250 µm 375 µm 500 µm	MP-0-X MP-250-X MP-375-X MP-500-X	OM / SEM	Analysis of MnS inclusions, Coating oxidation, porosity, and roughness
HIC susceptibility	4	Yes	Without coating 250 µm 375 µm 500 µm	HS-0-X HS-250-X HS-375-X HS-500-X	TM0284 immersion test	Calculation of CSR, CLR, and CTR on cross-section
Galvanic interaction	3	Yes	250 µm 375 µm 500 µm	GI-250-X GI-375-X GI-500-X	Immersion and analysis with SEM/OM	On cross-section straight through defect
OCP & PDP	4	No	Without coating 250 µm 375 µm 500 µm	OCP-0-X OCP-250-X OCP-375-X OCP-500-X	Electrochemical behavior	In 0.5 M H_2SO_4 and 5 g/L Thiourea
Cathodic charging	4	Yes	Without coating 250 µm 375 µm 500 µm	HI-0-X HI-250-X HI-375-X HI-500-X	Microhardness and analysis with SEM/OM	In 0.5 M H_2SO_4 and 5 g/L Thiourea
Microhardness	4	No	Without coating 250 µm 375 µm 500 µm	HV-0-X HV-250-X HV-375-X HV-500-X	Microhardness (on unimmersed samples)	Subsurface microhardness measurements

Table 3.5: Experimental tests which are conducted in this thesis

3.3 Characterisation of the substrate microstructure

Some information was already known from the inspection certificate of the metal, an additional microstructural analysis had to be performed on the metal S235JR+AR substrate to identify whether the material contained elongated MnS inclusions. Metal samples were cut with an automatic cutting machine (Struers Accutom-100) to obtain deformation-free cross-sections. A first cut was made perpendicular to the rolling direction (RD) after which sections were cut parallel to the rolling direction. Analysis was conducted on the rolling direction (RD) plane and normal direction (ND) plane, respectively A and B surfaces in figure 3.4. Two pieces with sides A and B were then hot mounted in a conductive resin which was required for scanning electron microscopy (SEM) and energy dispersive x-ray spectroscopy (EDS) analysis. Wet grinding was performed with sanding paper, starting with 320 and finishing with 4000 grit. The samples were then polished with disks of 3, 1 and 1/4 µm. A final etch for 10 seconds was performed in a Nital solution.

3.3.1 Optical Microscopy (OM) and SEM-EDS

A Keyence VHX digital microscope was used for a preliminary analysis of the microstructure. Magnifications of 100x, 200x and 300x were used to analyse existing cracks and defects in the material. A total of three samples for each plane were checked at random locations. A second analysis was then conducted with SEM-EDS, the instrument which was used is the JEOL JSM-IT100. With this machine, a better understanding could be obtained from the microstructure of the metal and the presence of MnS inclusions. SEM was used with different magnifications and EDS was used for elemental analysis of the inclusions in the metal.

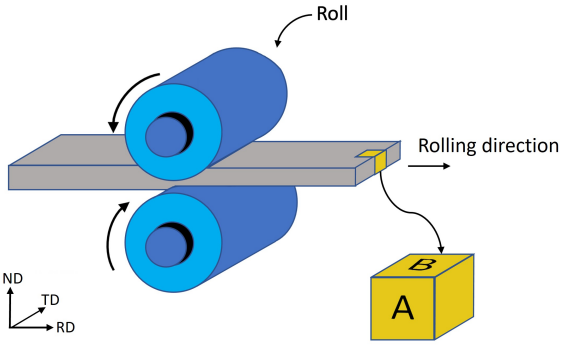

Figure 3.4: Rolling direction and inspected sample surfaces of the substrate

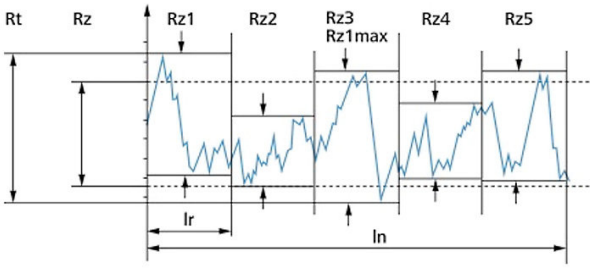

Figure 3.5: Surface roughness measurements according to ISO 4287 to obtain Rz of a surface

3.4 Characterisation of the coating microstructure

Properties of coatings are often defined by their composition, structure and thickness. With this microstructure analysis, it is possible to identify the relative differences between coatings with different thicknesses. Important properties that greatly influence corrosion resistance and mechanical properties are porosity content, oxidation, surface roughness, element distribution, microcracks and the quality between the substrate and the coating interface. Samples were sectioned and mounted in a conductive resin, wet grinding was performed with sanding paper, starting with 320 and finishing with 4000 grit. The samples were then polished with disks of 3, 1 and 1/4 µm. A total of three samples were made for each coating thickness.

Cross-sectional images were taken with SEM-EDS to analyze the coating, porosity was analysed according to the ASTM E2109-01 standard [187] for measuring porosity ratings on cross-sections of thermal sprayed coatings. A threshold was applied to differentiate between unmelted particles, oxidation and cracks. Additionally, a filter in ImageJ was used to remove speckles with pixel size below 2, and large oxide inclusions over 50 pixels in size. In order to exclude interfacial oxide scales, a final filter was selected to remove particles with a circularity below 0.20.

The roughness was calculated by deviation from a roughness profile using Python as outlined in ISO 4287, the code which was written can be found on Github [188]. The Rz, which is the average maximum surface height, was calculated from the average of the maximum peak-to-valley height (Rt) in five equal sampling lengths. The Ra was measured as the arithmetic average of the complete sampling length. An example of these measurements can be seen in figure 3.5. A total of ten micrographs were taken with optical microscopy (OM) at 300x magnification from three different samples, were analysed over a sampling length of 1 mm. The contour from the surface roughness could be obtained by using the threshold tool in ImageJ after porosity and outliers were removed with the binary tool.

Element distributions in the coatings were determined with the EDS element mapping tool. Fifteen different random areas were inspected at 700x magnification on three different samples. The mapping tool was used to obtain the percentage of oxidation in the coating and to identify whether there were any remarkable distributions of elements throughout the coating. The line tool was used in EDS mode to identify whether there were any

differences throughout the coating coating thickness. SEM was furthermore used to obtain information about the quality of the substrate and coating interface, and the potential presence of through coating defects exposing the substrate.

3.5 Microhardness Vickers test

Subsurface microhardness tests were performed to determine the variation in hardness of the substrate material and coating. The microhardness was analysed in this study to identify differences in residual stress from shot peening effects and cooling stresses as the coatings become thicker. Various studies have shown that differences in residual stress can be related to microhardness [189, 190]. Testing with normal hardness methods is unsuitable for cross-sections of thin coatings and thus requires a microhardness machine. The instrument which was used is the Struers DuraScan G5. Samples were prepared by cutting perpendicular to the RD, these smaller sections were then hot mounted in a non-conductive resin. Wet grinding and polishing were conducted with an automatic grinding and polishing machine using different sandpapers with grit sizes ranging from 320 to 4000 (wet) and finished by polishing with two steps up to 1 µm.

The test was carried out by applying a load with a diamond indenter (HV0.3) to obtain a mark on the material. The first measurement was taken at 40 µm from the free surface to eliminate any surface effects. Regular intervals of 40 µm were applied for hardness recordings until the interface was reached. Hereafter intervals of 80 µm were applied between each recording on the substrate. These larger intervals were necessary due to the lower hardness relative to the thermal sprayed coating.

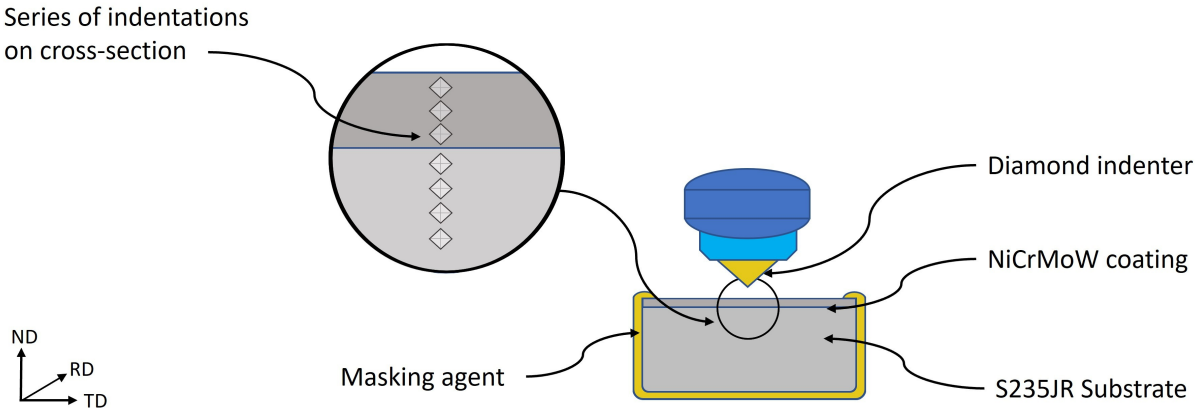

Figure 3.6: Series of microvickers hardness test with DuraScan test instrument

3.6 Electrochemical and corrosion experiments

A variety of electrochemical and corrosion tests were conducted to identify the behaviour and corrosion resistance. A fit-for-service test was performed with an adapted TM0284 [191] immersion test which is meant to reasonably simulate in-service exposure, immersion in H_2S for the qualitative tests was outsourced to an external laboratory (Element,

Amsterdam), while the analysis of the immersed samples and electrochemical tests were conducted at the Materials Science Engineering Laboratory at the TU Delft. This analysis included experiments to identify resistance to H_2S, HIC and the galvanic interaction between the coatings and the substrate. Further testing was conducted to compare relative electrochemical differences between the coatings. Instead of an H_2S solution, an alternative solution was used due to safety constraints. An acidic solution containing 0.5 M H_2SO_4 and 5 g/L thiourea was made as an alternative. Thiourea is a recombination poison such as H_2S [192], and was thus chosen as a substitute to inhibit hydrogen recombination. Electrochemical tests conducted in this solution were open circuit potential (OCP) measurements, potentiodynamic polarization (PDP) measurements and cathodic charging tests.

3.6.1 Immersion testing

NiCrMoW coatings were immersed in a H_2S solution to identify their barrier properties and corrosion resistance. Immersion was carried out according to NACE-TM0284 with adaptations, the TM0284 test is an industry standard for HIC resistance to identify whether a material is fit-for-use in sour environments. Besides identifying whether the coatings are fit-for-service, the immersed samples will be used to compare and determine the effectiveness of the NiCrMoW thermal sprayed coatings to enhance HIC resistance in carbon steels and to analyze the galvanic effect between the substrate and coating.

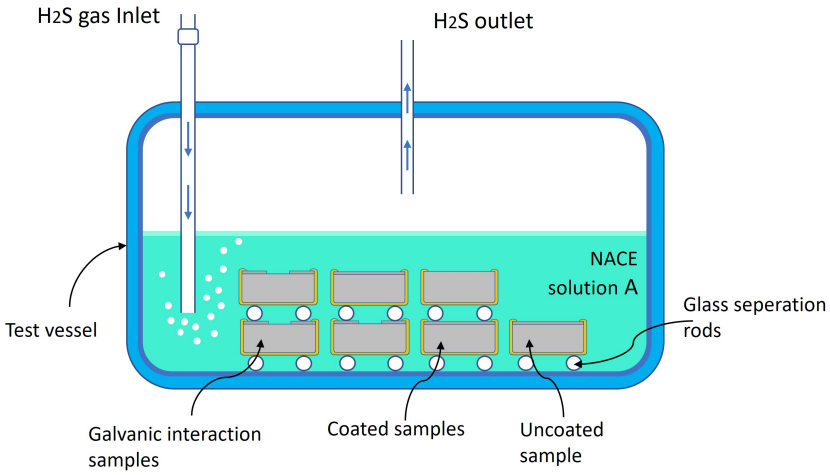

Figure 3.7: Orientation and stacking of the test samples for immersion testing according to TM0284 [191]

A standard TM0284 test is normally conducted by immersing metal samples for a period of 96 hours in distilled water, which is rich in H_2S, NaCl and CH_3COOH. In this study, the immersion test was performed at a temperature of 24.4 °C for a duration of 240 hours. An extended time was required as the sides and bottom of the samples were masked with polyglass, in a normal immersion test all sides are exposed. The specimens were stacked with the thermal sprayed coating facing up and were kept apart by nonmetallic or glass rods to prevent contact. The test setup of the adapted TM0284 test is schematically displayed in figure 3.7.

Masking is used to prevent hydrogen ingress and corrosion on the uncoated sides of the

carbon steel. Before the masking agent was applied, the surface of the carbon steel substrate was cleaned and roughened (before thermal spraying) to ensure proper mechanical interlocking between the substrate and the coating. The samples were grit blasted at the IOT Aachen with SiC particles of F-20 at all sides until grade Sa 2.5 according to ISO 8501 standard was obtained. The first layer was applied shortly after thermal spraying at Pakor in Ridderkerk, after 24 hours a second layer was applied. The total thickness of the coating was measured to be approximately between 1850 and 2000 µm.

The PAKOR-Polyglass VEF coating was selected due to its excellent corrosion resistance, especially in hydrogen sulfide environments. This specific type of coating (glass flake vinyl ester acrylic co-polymer) is frequently applied to prevent HIC in various susceptible vessels in the oil and gas industry. Additionally, it has a high resistance against CH_3COOH and NaCl which were both present in the immersion solution (NACE solution A) to which it was exposed to.

The reagents of the sour solution (Denoted as NACE solution A in TM0284) were H_2S gas, NaCl and CH_3COOH. The solution was prepared in a separate container other than the immersion vessel. First, a mixture was made consisting of 5 wt% NaCl, 0.5 wt% CH_3COOH and distilled water with an initial pH of 2.7 ∓ 0.1. The vessel was then immediately sealed and purged (near the bottom of the vessel) with nitrogen for one hour at a rate of 100 cm^3/min per litre of test solution. Thereafter, the solution was transferred to the test vessel (in which the test specimens are already placed) and again immediately purged (near the bottom of the vessel) with nitrogen at a rate of 100 cm^3/min per litre of test solution for 60 minutes. After purging, H_2S was introduced to the solution with an approximate rate of 200 cm^3/min per litre of test solution by bubbling for 60 minutes. Thereafter a positive pressure of H_2S was maintained with a constant gas flow rate to ensure that the solution remains saturated with H_2S. At the end of the test, iodometric titration and a pH measurement were performed to confirm that the concentration of H_2S was at least 2300 ppm and the pH lower than 4.0. The measured test conditions are displayed in table 3.6, and the report as received from Element is included in Appendix section C.

Test Conditions			
Solution type	NACE solution A	**Test duration (hr)**	241
Initial pH	2.73	**Temperature (°C)**	24.4
pH at start of test	2.87	**H_2S at start of test (mg/L)**	2939
pH at end of test	3.63	**H_2S at end of test (mg/L)**	2777
Oxygen	<5 ppb		

Table 3.6: Test conditions of the adapted TM0284 immersion test

A total of seven samples as displayed in figure 3.9, with size 100x20x10 mm were immersed to analyze corrosion effects. Three of the seven samples with coating thicknesses 250, 375 and 500 µm were immersed for determination of coating effectiveness, three samples with coating thicknesses 250, 375 and 500 µm and a holiday (figure 3.8) were immersed to study the galvanic interaction between the substrate and coating. The seventh sample was uncoated and used as a benchmark. The size of this holiday was milled with a 12 mm ⊘ milling bit, and the depth of the defect was 1 mm [193]. This resulted in a small difference

in the anode to cathode surface area for the three coatings which was incorporated in the calculation of the corrosion rate (CR).

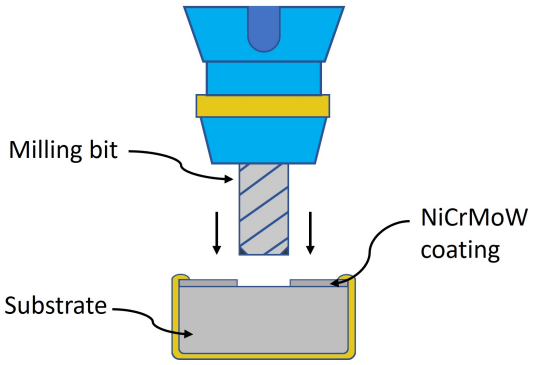

Figure 3.8: Milling of the samples through NiCrMoW coating for galvanic interaction analysis

All samples were masked with a masking agent before immersion testing. Masking is used to prevent corrosion and subsequent hydrogen ingress on exposed carbon steels on the uncoated sides of the metal. Before the masking agent was applied, the surface of the carbon steel substrate was cleaned and roughened (before thermal spraying) to ensure proper mechanical interlocking between the substrate and the coating. The samples were grit blasted with SiC particles of F-20 at all sides until grade Sa 2.5 according to ISO 8501 standard was obtained. The first layer was applied shortly after thermal spraying at Pakor in Ridderkerk, after 24 hours a second layer was applied. All layers were applied with a brush. The total thickness of the coating was measured to be approximately between 1850 and 2000 µm.

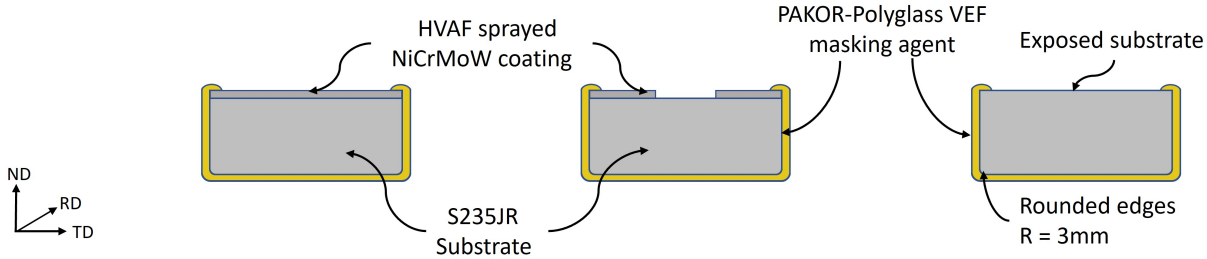

Figure 3.9: Three different series of immersion samples, with different coating thickness

3.6.2 Microscopy and EDS analysis

Before and after exposure, cross-sections of the samples were studied with OM and SEM-EDS. Analysis before immersion is performed in order to obtain information about existing defects in the material. It is important that defects such as inclusions, scratches and laminations can be distinguished from each other. Only defects which were visible with 100x magnification were included in the calculation to obtain reliable results. Susceptibility is calculated from the crack sensitivity ratio (CSR), crack length ratio (CLR) and crack

thickness ratio (CTR) as described in TM0284. The equations CSR, CLR and CTR are displayed in equations 3.1 to 3.3, where a is the crack length, b is the crack thickness, W is the sample width and T is the sample thickness. OM and SEM-EDS were also used to analyse the galvanic interaction between the substrate and the coating.

$$CSR = \frac{\sum(a \times b)}{W \times T} \times 100\% \tag{3.1}$$

$$CLR = \frac{\sum a}{W} \times 100\% \tag{3.2}$$

$$CTR = \frac{\sum b}{T} \times 100\% \tag{3.3}$$

Samples for optical microscopy and SEM-EDS were prepared by sectioning the sample into four even parts, as displayed in figure 3.10. For analysis of the galvanic interaction, the samples were prepared by sectioning through the milled hole. All samples were hot-mounted in a conducting resin and prepared with an automatic grinding and polishing machine (Struers Tegramin-30). For grinding, papers with different grit sizes ranging from 320 up to 4000 (wet) were used, subsequent polishing was conducted with cloths of size 3, 1 and 1/4 µm.

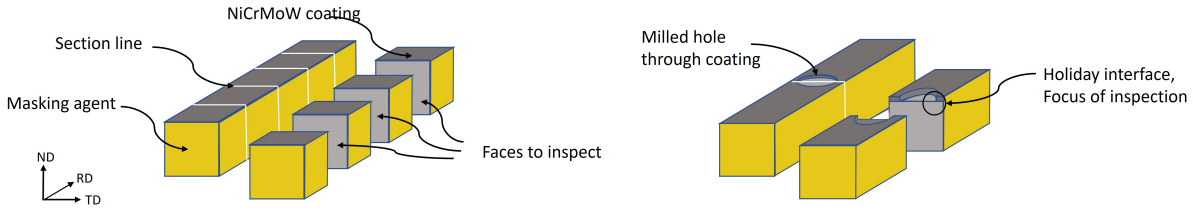

Figure 3.10: Sectioning of the samples and inspection faces

3.6.3 Open circuit potential (OCP) and potentiodynamic polarization (PDP)

An open circuit potential (OCP) test was carried out to identify the free potential between the working specimen and reference electrodes. After establishing the OCP, a potentiodynamic polarization (PDP) test was directly initiated. PDP were performed to compare the relative polarization resistance of the coatings.

Experimental set-up

The OCP and PDP measurements were performed in a three-electrode cell depicted in figure 3.11. The setup consisted of a platinum (Pt) counter electrode, $Ag/AgCl_{sat}$ reference electrode and the sample which functioned as a working electrode. The sample was clamped in a mount at the bottom of the cell with a fixed exposure area of 0.385 cm^2. The cell was connected to a VSP-300 Potentiostat, EC-lab software was used to run PDP test right after the OCP was finished. The electrolyte consisted of a 0.5 M H_2SO_4 electrolyte with 5

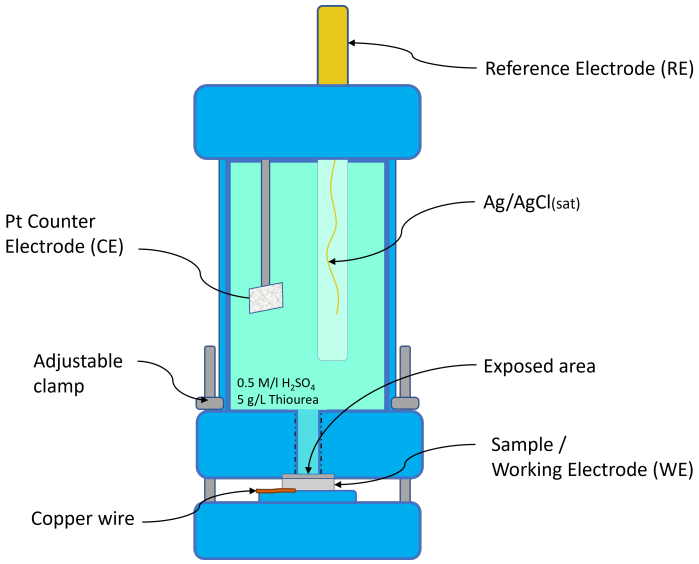

Figure 3.11: Experimental electrochemical cell set-up for conducting OCP and PDP measurements

Figure 3.12: Actual electrochemical cell setup

g/L thiourea (CH_4N_2S), tests were conducted at 20 °C and atmospheric pressure.

Settings which were used and duration are shown in table 3.7. Samples for this test were cut into squares of 25 x 25 mm, the coated samples were tested in the as-sprayed condition, while the carbon steel surface was prepared by wet grinding up to 320 grit. Samples were tested for both OCP and PDP in sets of three to assure data repeatability. After each test, the electrochemical cell was thoroughly cleaned and refilled with 70 ml of new solution.

Step	Electrolyte	Potential (V) $Ag/AgCl_{sat}$	Duration (min)	Scan rate (mV/s)
OCP	0.5 M H_2SO_4+ 5g/L thiourea	-	120	-
PDP	0.5 M H_2SO_4+ 5g/L thiourea	-1.25 to 1.25 V	-	0.500

Table 3.7: Settings for OCP and PDP test

3.6.4 Cathodic charging

Samples were cathodically charged in a 0.5 M H_2SO_4 electrolyte with 5 g/L thiourea at 20 °C and atmospheric pressure. Samples were sectioned to analyse the effect of hydrogen ingress and material loss. Charging was performed in a three-electrode cell such as used for the OCP and PDP test (figure 3.11). The setup consisted of a Pt counter electrode, an $Ag/AgCl_{sat}$ reference electrode and the sample as the working electrode. The sample was clamped in a mount at the bottom of the cell with a fixed exposure area of 2.53 cm^2, a larger fixture different from the OCP and PDP test to facilitate sectioning post charging. A current of 12.7 mA was passed to achieve a current density of 5 mA/cm^2, the charging experiments were conducted for a total of 16 hours.

Microhardness Vickers test

The effect of hydrogen diffusivity in the coating and underlying substrate was assessed by subsurface microhardness measurements. A high hardness measurement is indicative of a high concentration of hydrogen, by taking multiple measurements on cross-sections of the immersed samples the hydrogen diffusivity can be compared. The method which was used in this experiment is adapted from a study by P. Kumar et al. [194] and P. Escobar et al. [195].

Thirty minutes after extraction from the electrochemical cell, the samples were sectioned, ground and polished up to 1 µm. A series of measurements on the sample were taken approximately two hours after removal from the cell. Due to severe material loss in the charged samples, the first measurements were taken on 40 µm from the 'new' free surface. After measuring the microhardness on the NiCrMoW coating surface, a series of measurements were taken on the carbon steel substrate, starting just below the interface with intervals of 80 µm. Measurements were compared with the results of the microhardness measurements of the uncharged samples, which were obtained from the experiment in section 3.5.

4

Results and Discussion

4.1 Substrate characterisation

A preliminary characterisation of the substrate was performed in order to obtain information about its susceptibility to HIC, and its condition in terms of defects.

The top side and cross section (respectively sides A and B from figure 3.4) were inspected with OM. The microstructure was studied for defects, cracks and MnS inclusions. From the images in figures 4.1 and 4.2 a clear difference can be seen in terms of microstructure. Side B shows a uniform two-phase microstructure while side A shows an elongated two-phase microstructure. Both seem to contain a certain degree of contamination or inclusions but from the micrographs, their exact nature can't be established.

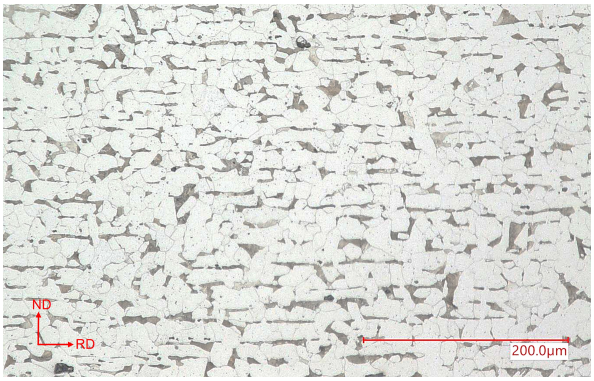

Figure 4.1: Optical microscopy image (500x) of substrate cross-section (A side)

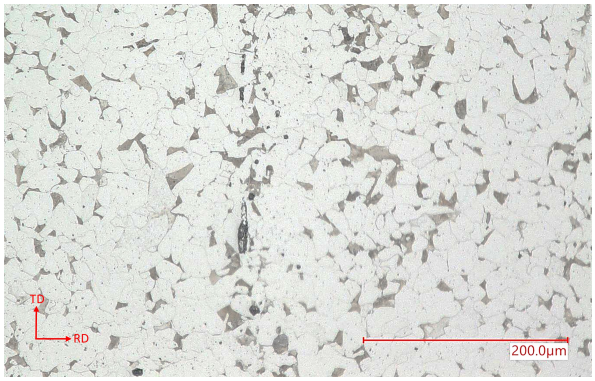

Figure 4.2: Optical microscopy image (500x) of substrate top section (B side)

From the images made with SEM a better understanding of the microstructures could be obtained, the rolling direction and normal direction plane in the microstructures which were established with OM are again clearly seen. In figure 4.3 pearlite grains can be seen, which can be identified by the layered structure. The second phase can be identified as ferrite as the steel only contains 0.152 wt% carbon, which is not enough for a combined pearlite and cementite microstructure.

In the SEM micrograph of side B in figure 4.4 a group of inclusions can be observed which are around 10 to 20 µm in size. On the A side, similar but elongated inclusions are

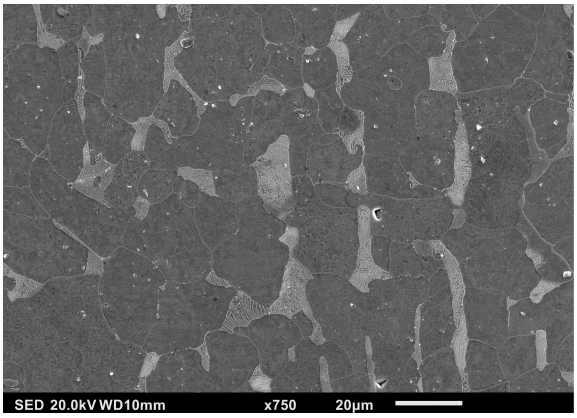

Figure 4.3: SEM micrograph (750x) of substrate cross-section A side

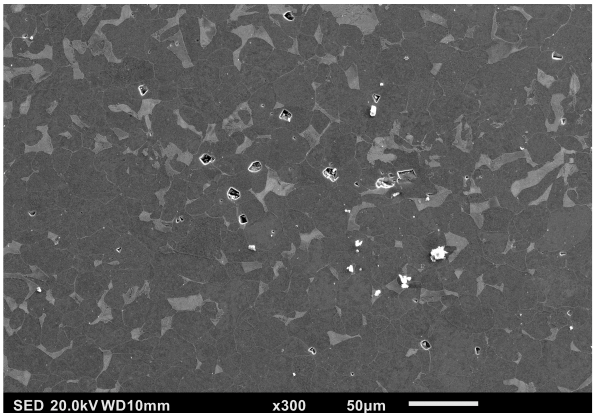

Figure 4.4: SEM micrograph (300x) of substrate top section B side

observed. SEM-EDS analysis which was conducted on the inclusions, revealed that these contain a high quantity of manganese and sulfide. The analysis with EDS was performed with an energy of 20 keV. Figure 4.5 shows the spectrum and SEM micrograph of one of the inclusions. Different mass % were found, 72.31 for Fe(K), 19.54 for Mn(K), 7.58 for S(K) and 0.58 for Ti(K). The MnS inclusions are primarily concentrated in the centre of the steel. This is a phenomenon caused by centreline segregation, which occurs during solidification and cooling of molten steel. During hot rolling the centre of the steel is the last part to solidify and thus MnS will preferentially segregate to the centre [196].

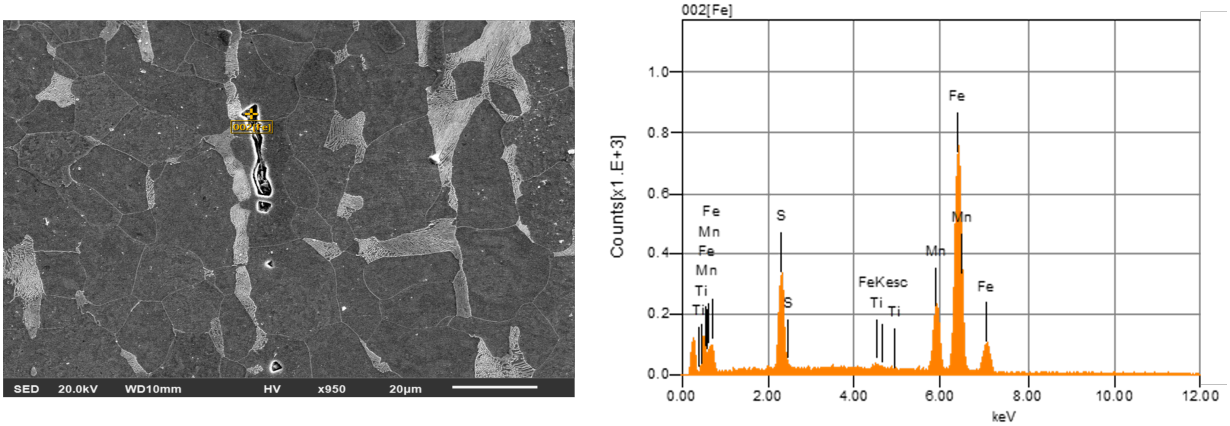

Figure 4.5: SEM-EDS (950x) of elongated MnS inclusion on cross-section (MD-01-A)

4.2 Characterisation of the coating microstructure

Figures 4.6, 4.7 and 4.8 show examples of the 250, 375 and 500 µm coatings. At first sight, the coatings look dense with some signs of porosity, unmelted particles, oxidation and microcracking. An overview of the defects is given in Appendix D. The interface between the substrate and coating is continuous without signs of cracking or delamination. There are some embedded grit particles from the grit blasting process, it is not expected that this has an influence on the performance of the coating.

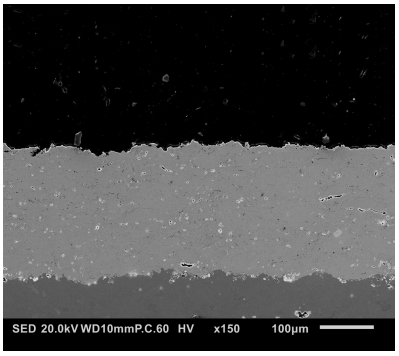

Figure 4.6: SEM micrograph taken at magnification 150x of 250 µm coating

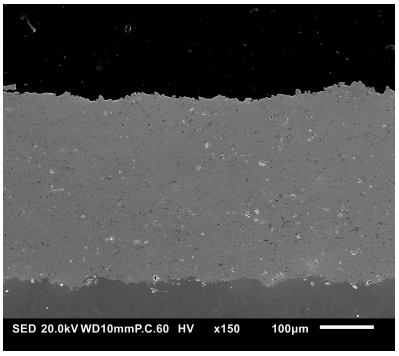

Figure 4.7: SEM micrograph taken at magnification 150x of 375 µm coating

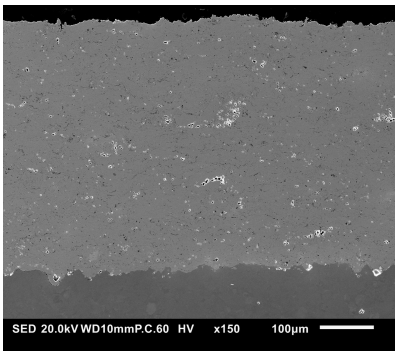

Figure 4.8: SEM micrograph taken at magnification 150x of 500 µm coating

4.2.1 Surface roughness with Python

The program which was written in Python to calculate the Ra, Rz and Rt allowed accurate profile plotting of the coating surface, an example for one of the 500 µm sections can be seen in figure 4.9. The blue line follows the surface profile while the white line depicts the mean value. The program returns the profile and Ra, Rz and Rt. The averaged results from the analysed samples are displayed in table 4.1. As is evident from the values, the coatings are moderately rough with only slight variations in Ra, Rt or Rz from each other. These values are similar to the roughness values found in literature [197, 198] for thermal sprayed coatings. From these results, it can be assumed that coating thickness does not influence surface roughness. The code which was written can be found on GitHub [188].

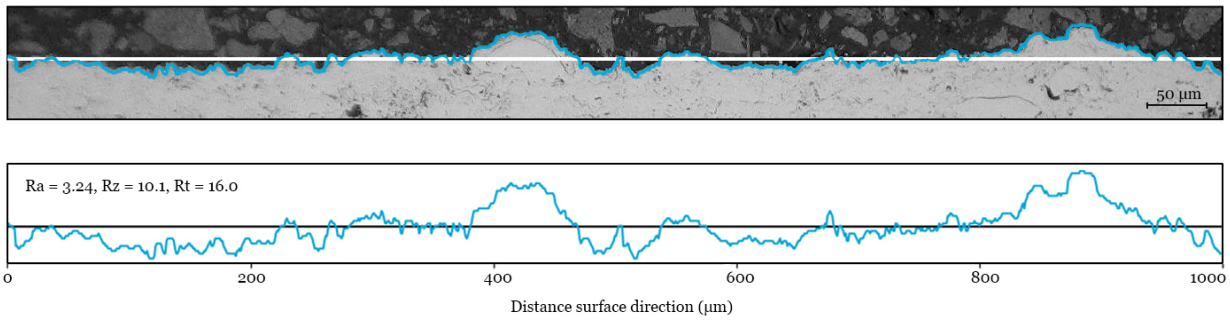

Figure 4.9: Optical microscopy detail of 500 µm coating surface roughness with example of Python output in the figure below

4.2.2 Porosity

From figures 4.6 to 4.8 it is clear that porosity is present in all coatings. The distribution is found to be uniform, meaning that there is no difference in porosity in the inner, centre or outer layers of the coating. The threshold which was used to differentiate between oxide inclusion was obtained by trial and error and kept constant for all samples. Some difficulties with obtaining the correct threshold were overcome with adjustments in the microscopy light setting to create a greater contrast difference between the oxides and pores. An example of a processed image with consecutive steps is seen in figure 4.10 to 4.12. The measured total porosity in volume fraction (denoted as Vol %) and the distribution of different pore sizes in terms of volume fraction can be seen in table 4.1. As is evident from the results, the total porosity decreases with increasing coating thickness. Furthermore, pore size larger than 1.0 μm^2 seems to be more prevalent as the coating thickness decreases while the opposite is true for pore sizes in the range 0.1 - 1.0 μm^2 and pores smaller than 0.1 μm^2.

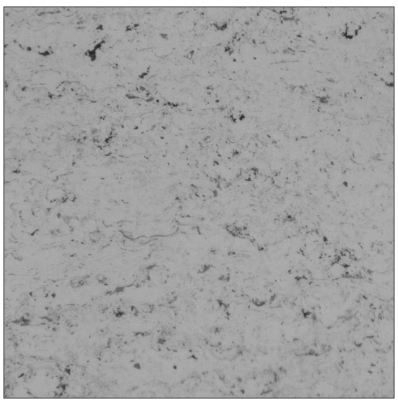

Figure 4.10: Optical microscopy micrograph with cross-section of TSC

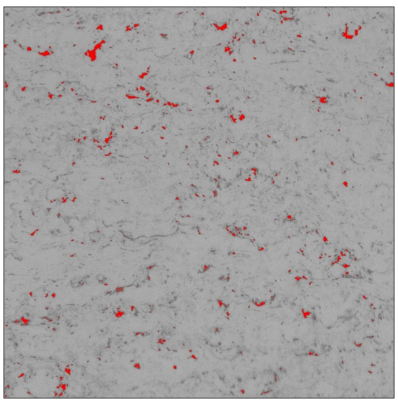

Figure 4.11: Varying threshold to differentiate porosity and oxidation

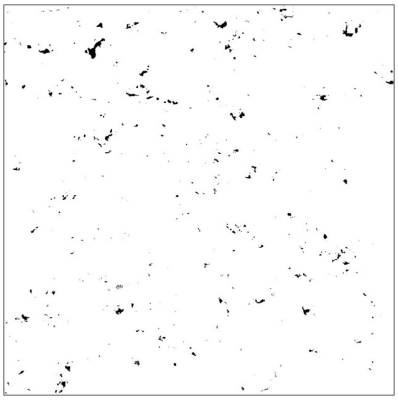

Figure 4.12: Threshold after filter including porosity and excluding oxidation

Microcracks were mainly found at unmelted particles (Appendix D) which were present in all coatings. The amount of these increased especially in the 500 µm coating. Similar observations have been made in previous studies and is commonly attributed to a build up of residual stresses [15, 199]. As explained in section 2.6.1 these residual stresses can increase with increasing coating thickness.

	Total porosity	Volume fraction of pore sizes(%)			Surface roughness (µm)		
	Vol %	*>1.0 μm^2*	*0.1 - 1.0 μm^2*	*<0.1 μm^2*	*Ra*	*Rz*	*Rt*
250 µm	0.78 ± 0.16	82.5 ± 3.3	16.1 ± 2.7	1.5 ± 0.3	3.2 ± 0.8	11.6 ± 2.2	19.2 ± 5.3
375 µm	0.68 ± 0.14	80.2 ± 3.3	17.5 ± 2.5	2.2 ± 0.4	3.1 ± 0.7	11.9 ± 1.4	19.4 ± 4.3
500 µm	0.62 ± 0.10	78.1 ± 3.0	19.3 ± 3.0	2.6 ± 0.1	3.1 ± 0.6	11.1 ± 1.5	19.5 ± 3.5

Table 4.1: Computed porosity, volume fractions of pore sizes and surface roughness for all coatings

While the thicker coatings have a more uniform distribution of smaller pores, this advantage could be outweighed by microcrack formation due to residual stresses. The exact effect on corrosion resistance through coating porosity or hydrogen diffusion is difficult to estimate from these results alone, the electrochemical tests will reveal the precise effects which take place.

4.2.3 Element distribution

Table 4.2 shows the average quantity of elements for the different coatings, as expected there is not much difference between the three coatings and results correspond to the manufacturer's specifications with an exception for carbon and oxygen. Oxidation seems to increase with thickness, most likely caused by an increase in coating temperature from longer heating during the process and the additional cooling passes which were necessary to reach optimal spraying temperatures. Measurements taken across the wall thickness of the sample showed that there was no difference in composition.

	Ni	Mo	Cr	Fe	W	Co	S	V	C	O
250 µm	57.10	14.61	14.16	5.86	3.62	1.34	0.32	0.017	2.00	1.04
375 µm	57.14	14.62	14.10	5.92	3.64	1.34	0.26	0.018	1.65	1.31
500 µm	57.18	14.53	14.10	5.96	3.63	1.37	0.29	0.018	1.76	1.40

Table 4.2: Distribution of elements in wt%, average from 15 areas measured with EDS at magnification 700x

The origin of the relatively high content of carbon in the coatings is however unknown. Carbonation during the thermal spraying process is unlikely due to the short exposure time, a more likely cause is contamination from the epoxy binder during polishing where carbon particles may get stuck in the porosities. This second hypothesis is also reinforced when the carbon content is compared to the volume fraction of porosity, as the relative quantities are comparable.

In figures 4.13 to 4.18 the distribution of Ni, Cr, Mo, W and O can be seen at magnification 700x in a 500 µm coating. Two areas of interest have been marked with yellow and blue squares on all figures. These two features were a reoccurring phenomenon in all EDS analyses performed on the different coatings. They show that areas with high oxidation go along areas with high counts of chrome, and a deficit of Ni and Mo, this can be particularly made clear from the yellow marked areas. Chrome is preferentially oxidized over the other elements, areas around the chromium oxide are depleted in chrome and show a higher count of Ni and Mo. This effect is caused by the higher affinity of oxygen for chromium than the other elements. These metal oxides have a negative effect on corrosion performance, studies found that preferential corrosion occurs in areas with high oxide content [200, 201]. Additionally, these metal oxides reduce adhesion and intersplat cohesion [99].

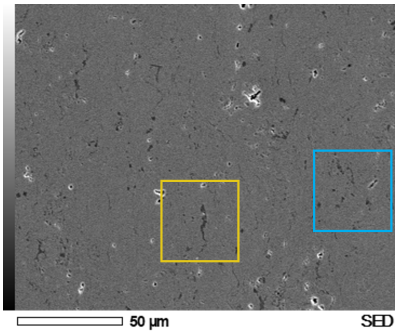

Figure 4.13: SEM micrograph at magnification 700x

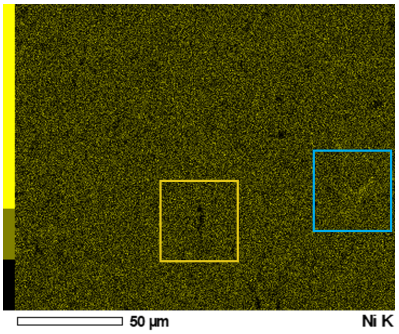

Figure 4.14: Elemental mapping of nickel from EDS

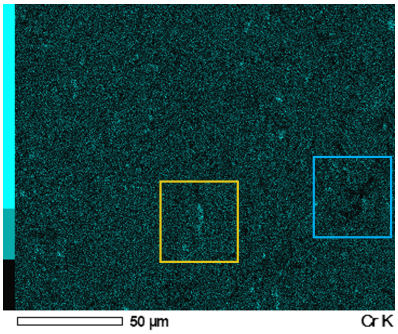

Figure 4.15: Elemental mapping of chrome from EDS

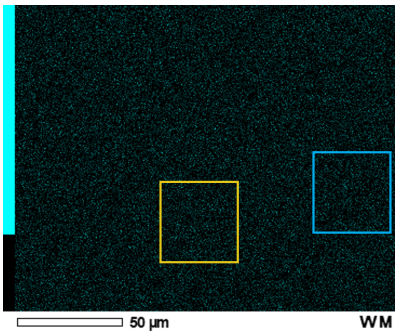

Figure 4.16: Elemental mapping of tungsten from EDS

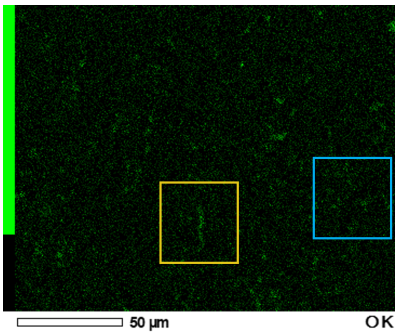

Figure 4.17: Elemental mapping of oxygen from EDS

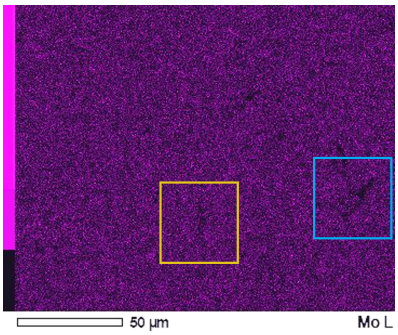

Figure 4.18: Elemental mapping of molybdenum from EDS

4.3 Subsurface microhardness measurements

A series of HV0.3 indents with a constant separation of 40 µm were set into the coating and substrate. Indentation started at approximately 40 µm from the free surface and ended 40 µm from the substrate interface. Another series of four indents was then set in the substrate, starting 40 µm from the interface with a separation of 80 µm. The results of these measurements on the coatings and substrates can be seen in figures 4.19 and 4.20, the line in these graphs are second-order polynomial trendline in order to correctly fit the measurements and reduce fluctuations.

The measured microhardness in the coatings increases as a function of distance from the free surface. An opposite trend is observed for the microhardness of the substrates, where the hardness decreases as a function of the coating substrate interface. These variations are the effect of residual stresses from different origins. As explained in section 2.6.1, the origin of residual stresses in thermal sprayed coatings are from shot peening effects and fast cooling. Furthermore, it was explained that tensile stresses arise from the cooling of individual splats, or quenching. Compressive stresses are the result of the impact of coating powder and in addition, residual stresses can arise from a difference in thermal expansion coefficient (CTE) between the coating and substrate. Respectively for the coating and substrate, these coefficients are around $6{\cdot}10^{-6}/_{\circ C}$ and $11{\cdot}10^{-6}/_{\circ C}$ [202]. The three different

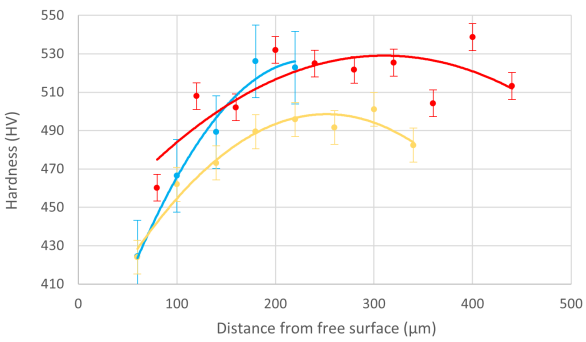

Figure 4.19: Microhardness measured on 250 µm, 375 µm and 500 µm thermal sprayed coatings

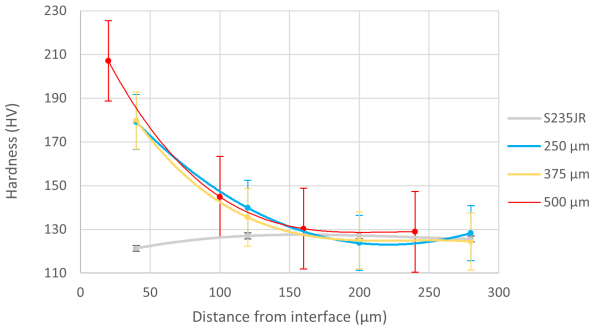

Figure 4.20: Microhardness measured across surface of unsprayed substrate, 250 µm, 375 µm and 500 µm thermal sprayed substrates

stresses are displayed in figure 4.21. If the CTE of the coating is lower than the substrate the stress in the coating will be tensile and visa versa. The microhardness increases from compressive residual stresses while is reduced from tensile stress [203–205].

Somewhat similar trends can be observed for all coatings, three regions are particularly of interest. In the first region, which consists of the first 200 µm, the microhardness rises from 430 to around 530 HV for the 250 and 500 µm coatings, and to 490 HV for the 375 µm coating. It is not exactly known why the 375 µm coating deviates from the other two, however, it is an indication of relatively lower compressive stress which may have an effect on corrosion resistance. In figure 4.19 this first zone is the initial steep rise. This region is a transitional region from tensile to compressive stresses due to the fact that the outer surface is not exposed to the same shot-peening intensity as the deeper layers. The second region starts right after the first region and ends 50 µm from the interface. This second region depends on the coating thickness, it is the most substantial in 500 µm coatings while it is non-existent in the 250 µm coating. In this zone the residual stress is constant. In the last region near the substrate and coating interface, a decline in hardness can be observed in all coatings. As explained, these are tensile stresses and the result of a mismatch in CTE between the substrate and coating [206].

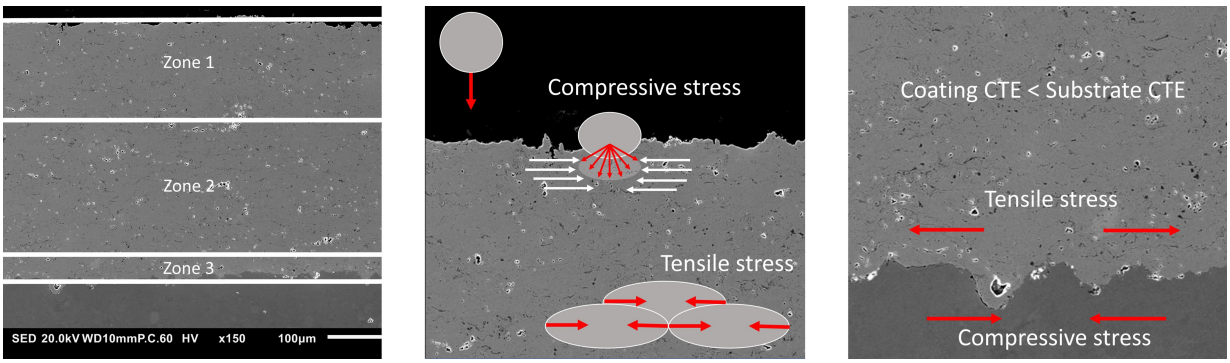

Figure 4.21: Residual stress zones and the presence of three different residual stresses in thermal sprayed coatings

The hardness of the thermal sprayed substrates is also increased near the interface. While it is certainly possible that the substrate hardness is affected by the thermal spraying process, it is more likely that the sharp increase is the result of compressive stresses from grit blasting [207]. There is only a small difference in hardness of the 500 µm coating, if the hardness primarily increased from the thermal input alone then a greater difference in hardness between the coatings would be expected.

4.4 Electrochemical and corrosion experiments

The first part of this section is focused on the results of the immersion test. The results of these tests include the impact of HIC susceptibility and galvanic interaction in H_2S and the effect of the H_2S solution on the coating microstructure. The second part of this section is focused on the electrochemical behaviour which was obtained with OCP and PDP measurements. At last the effect of cathodic charging is discussed on thickness reduction and hydrogen trapping of the material.

4.4.1 HIC susceptibility

The samples photographed after immersion are shown in figure 4.22. It is evident from this figure the surface of the uncoated sample shows hydrogen blistering. The coated samples are intact without visual evidence of blistering or discolouration. The black spots are found to be discolored residual glue from the masking tape which was used during grit blasting. The Pakor-Polyglass VEF sealant is found to be intact in all samples, with only slight discolouration.

Figure 4.22: Photographs of immersed samples, from left to right: without coating, 250, 375 and 500 µm

The sectioned coated samples are shown in figure 4.23. No evidence of corrosion could be found on the surface of the coatings through microscopy and SEM-EDS, which was expected due to the corrosion resistivity of the NiCrMoW. Additionally, the interface between the coating and substrate is intact in all inspected cross-sections, showing no signs of disbonding or corrosion.

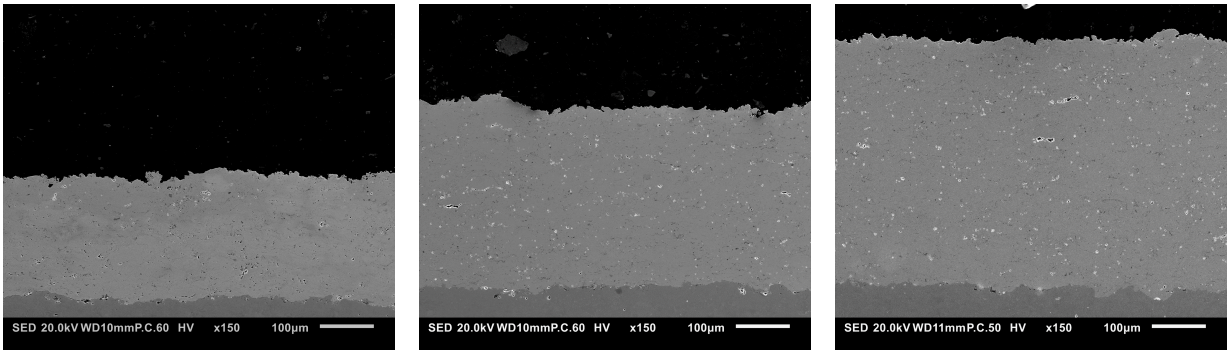

Figure 4.23: Cross-sections of 250, 375 and 500 µm coating after immersion at magnification 150

The cross-sections of the uncoated sample (figure 4.24 show clear hydrogen damage and FeS formation. Anlysis with SEM-EDS revealed that some of the blisters at the surface were filled with FeS, indicating that they had burst during immersion. Furthermore, larger cracks were found to be more concentrated near the surface, while the majority of thin cracks were found near the center of the cross-sections.

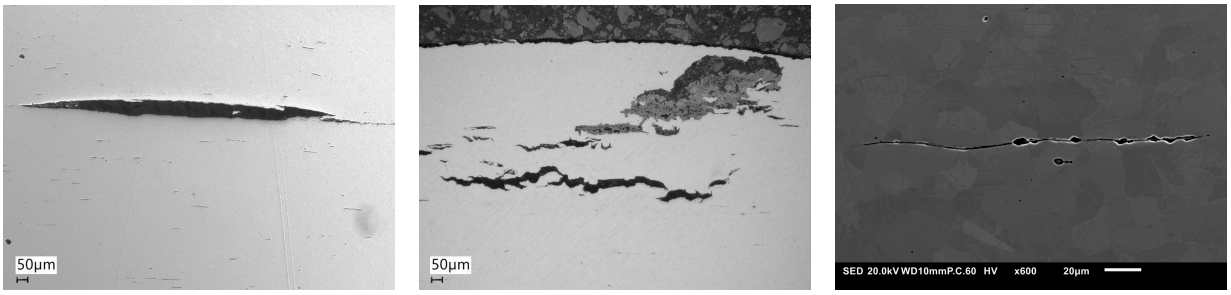

Figure 4.24: Cross-section of uncoated sample after immersion showing cracks and hydrogen blisters filled with FeS

Inspection of the Polyglass sealant in the cross-sections revealed that the solution had penetrated between the Polyglass and the thermal sprayed coating. In figure 4.25 it can be seen that the Polyglass sealant has slightly disbonded at the interface. Similar disbonding is observed in all thermal sprayed samples, but not in every cross-section. In the micrographs of figures 4.26 and 4.27 it can be seen that the H_2S solution has penetrated the Polyglass coating up to only 250 µm of the total 2000 µm thickness, this was expected as polymers are slightly permeable to H_2S and water [208]. The effect of disbonding might have influenced the test results as it seems from 4.25 that corrosion products have formed in between the coating and substrate. It can however be concluded that the Polyglass offered good protection in the areas where it was properly adhered to the substrate.

The difference in weight before and after immersion is presented in figure 4.3. The uncoated sample experienced a reduction in weight of 0.2395 grams, the coated samples increased in weight in varying amounts. As concluded, corrosion on or underneath the thermal sprayed coatings was not detected which corresponds to the absence of weight reduction. The weight increase can be explained by the previously discussed permeability of polymers to

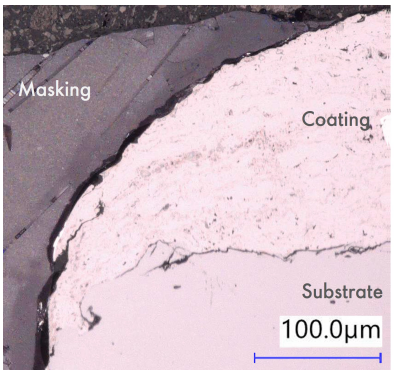

Figure 4.25: Disbonding at thermal sprayed coating and Polyglass interface

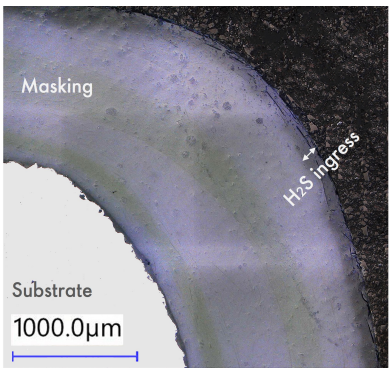

Figure 4.26: Micrograph showing the total H_2S ingress in the Polyglass coating

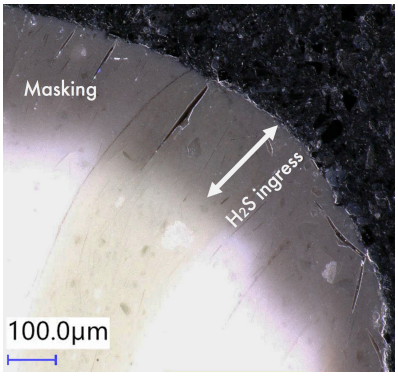

Figure 4.27: Discolored edge shows H_2S ingress and deteriorated part of the Polyglass coating

H_2S [208]. The differences in weight gain between the samples are most likely the result of fluctuations in the application process, surface irregularities or solution trapped in the disbonded areas between the Polyglass and thermal sprayed coating.

	HIC Test			Galvanic Test		
Sample	Weight BI (g)	Weight loss/gain (g)	CR (mmpy)	Weight BI (g)	Weight loss/gain (g)	CR (mmpy)
S235JR (uncoated)	163.9338	-0.2395	0.62	-	-	-
250 μm	164.9790	+0.0020	-	169.3953	-0.1047	1.01
375 μm	170.0206	+0.0085	-	168.0096	-0.1045	1.02
500 μm	173.3135	+0.0238	-	173.1292	-0.1078	1.06

Table 4.3: Weight gain and loss for HIC and galvanic samples, the table shows weight before immersion (BI), after immersion (AI) and the weight difference in grams

Effect of immersion on coating microstructure

The effect of immersion on the coating was inspected with SEM-EDS. Multiple areas in cross-sections and at the surface were inspected for corrosion products and/or degradation. No evidence of such could be found, which is in line with the absence of weight loss in the samples. While it is extremely likely that a passive chromium oxide layer can form on the outside of the coating which acts as a passive barrier it is not possible to detect this layer with SEM-EDS. These films are in the nanometer range and thus beyond the depth of field of SEM-EDS [209, 210]. In order to determine whether a passive layer has formed a technique such as X-ray photoelectron spectroscopy (XPS) is required, it is however not in the scope of this thesis.

Quantification of HIC

HIC susceptibility was determined from the ratios as described in TM0284 [191]. Detailed micrographs of the samples, stitched with Keyence software are provided in Appendix

D. The CSR, CLR and CTR for the samples are displayed in table 4.4, the final row depicts the acceptance criteria for which a material would be considered "fit-for-service". As expected from the internal cracks and blistering, the ratios for the uncoated S235JR carbon steel fall outside of this range. Especially the CLR has exceeded the limit, there are two possible explanations for this. (I) It is possible that the primary mode of cracking is the horizontal linkage of separate HIC cracks. This is influenced by the moderate properties of S235JR in terms of toughness and hardness. (II) Insights obtained from analysis of the S235JR's microstructure in section 4.1 showed that the microstructure consisted of a high concentration of MnS in the centre of the steel. Due to the high density of traps in this region, the hydrogen can distribute well and thus inhibit localized accumulation. It is possible that one of the mechanisms has had a more significant impact.

	CLR (%)	CTR (%)	CSR (%)
S235JR	77.3	8.4	2.8
$250\,\mu m$	4.2	8.0×10^{-2}	9.0×10^{-3}
$375\,\mu m$	3.9	0.2	9.0×10^{-3}
$500\,\mu m$	4.5	0.1	1.1×10^{-2}
Acceptance value [191]	< 15	< 5	< 2

Table 4.4: CLR, CTR and CSR after immersion in NACE solution A for 10 days

The ratios for the coated samples are well within the acceptance criteria. The CTR and CSR are especially low. No significant difference between the coatings in terms of the three ratios could be found. The CLR of all coated samples is measured between 3.9 and 4.5, which is in the acceptance range but higher than expected. The cracks which were found with SEM in these samples were small, microcracks could be distinguished from inclusions by the shape of the edge. These edges were sharp for microcracks and round for inclusion. It is possible, but unlikely, that these cracks have resulted from hydrogen diffusion through the coating. As concluded, there were no signs of corrosion on the coatings and blistering at the interface. It is more likely that corrosion at the interface due to disbonding of the Polyglass coating might have influenced the test results. The exact effect on CLR is therefore difficult to assess. Regardless, the main conclusion to be drawn is that the coating provides good protection in a sour environment.

4.4.2 Galvanic interaction

Figure 4.28 shows photographs of a sample before immersion and three samples after immersion. On the immersed sample the carbon steel in the holiday region is covered in corrosion products while the coatings itself does not show any signs of corrosion or discoloration. The weight loss for the galvanic samples is displayed in table 4.3. The samples have lost a similar amount of weight, which indicates that the coating thickness had an insignificant role in influencing galvanic interaction. Increasing the ratio of surface area between the anode and cathode increases the corrosion rate. However, this difference as the coating thickness increases is negligibly small. As explained in the previous section, the Polyglass coating may have absorbed a fraction of the H_2S or water, this effect will be

the same for the galvanic samples. Given the minimal gain in weight in the HIC samples, it is reasonable to assume that a similar amount is an increase in the galvanic samples. Even when this gain is considered, the differences between the galvanic samples remain modest. The corrosion rate slightly increases with coating thickness, however, these differences are minor. The corrosion rate of the galvanic samples compared to the uncoated substrate shows an increase of 66%. While it is difficult to precisely assess the increase in corrosion rate, it can be considered substantial. This result highlights the essence of a defect-free thermal sprayed coating which can remain intact during service.

Figure 4.28: Photographs of immersed galvanic corrosion samples, from left to right: 250 µm before immersion, 250, 375 and 500 µm

SEM-EDS inspection of the cross-sections proved that the scale which formed in the holiday consists of iron sulfide, an inspected area is shown in figures 4.29 and 4.30. The wt% found for Fe and S were respectively 62.9% Fe and 31.0% S, it is likely that this FeS compound is mackinawite ($Fe_{1+x}S$) due to the stoichiometric ratio and low oxygen and high H_2S environment in which it was formed. Corrosion seems to have accelerated near the substrate and coating interface (figure 4.31), which is apparent from undercutting. There are signs of disbonding close to this region, especially in the 375 µm coating. Likely reasons for disbonding are: (I) corrosion product pushing up the coating, or (II) relaxation of residual stresses in the coating [13].

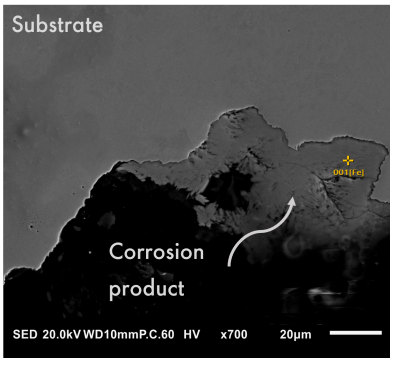

Figure 4.29: SEM-EDS point at corrosion scale taken at 700x magnification

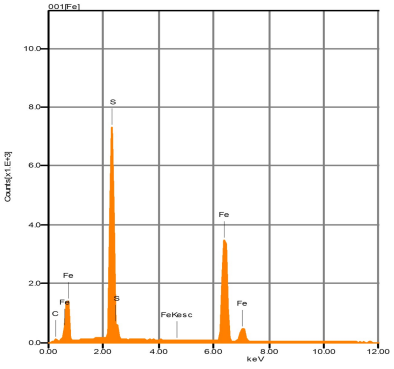

Figure 4.30: Spectrum of EDS point taken at corrosion scale

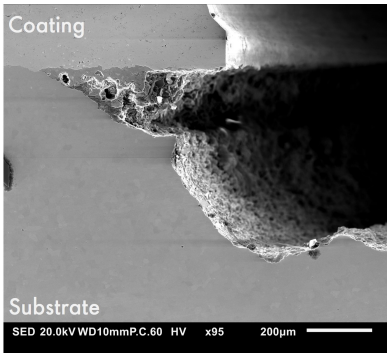

Figure 4.31: SEM micrograph taken at magnification 95x of coating and holiday region

Figure 4.32 shows cross-sectional images taken with optical microscopy from the three coated samples. These micrographs show similar undercutting near the substrate and coating interface for all three samples. The substrate at the bottom of the holiday region shows signs of pitting. Furthermore, inspection of underlying layers did not show any signs of HIC, this indicates that the surface area is not substantial enough to absorb sufficient amounts of hydrogen for HIC. The coating did not show evidence of corrosion, which is in line with what was found on the HIC samples. Damage to the edge of the 375 and 500 µm coatings in the holiday region was probably caused during the milling of the holidays. It is unlikely that this has significantly influenced the results of the test.

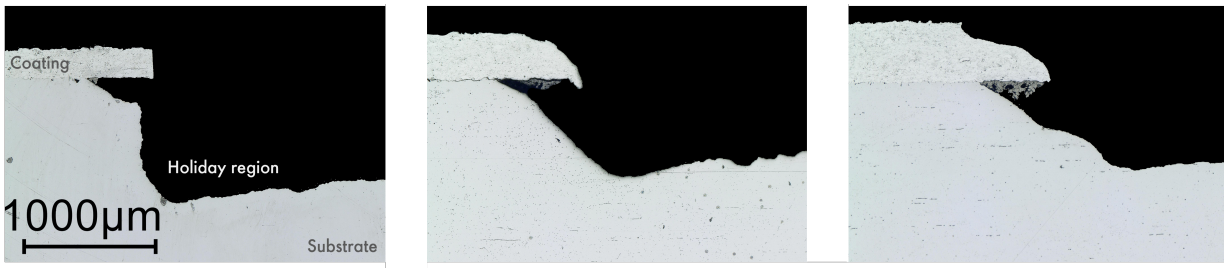

Figure 4.32: Cross-sections of immersed galvanic corrosion samples, from left to right: 250, 375 and 500 µm

4.4.3 Open circuit potential (OCP)

The corrosion behaviour of the coatings and substrate was recorded as a function of time and open circuit potential (OCP) as shown in figure 4.33.

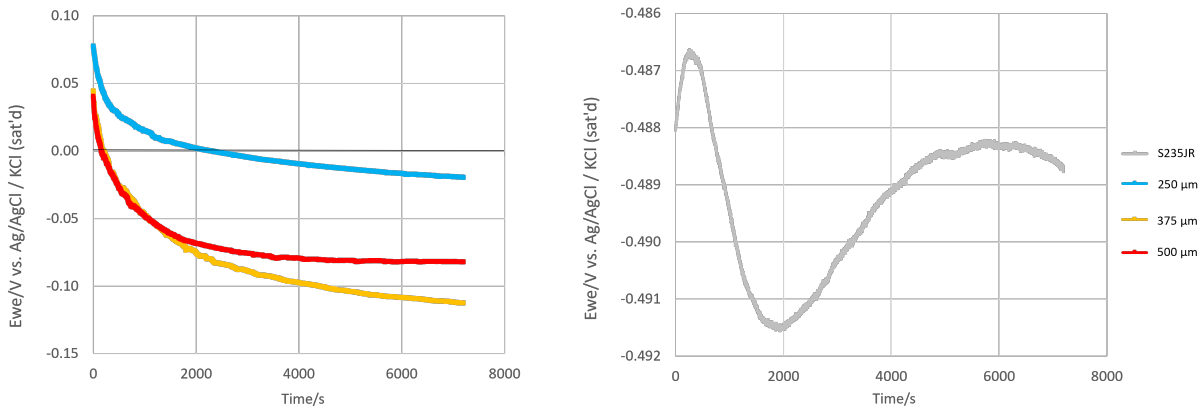

Figure 4.33: OCP for thermal sprayed coatings (250,375,500 µm and S235JR carbon steel in 0.5 M H_2SO_4 + 5g/L thiourea at room temperature

The coatings show similar trends with an initial positive OCP value at the start of the test which then quickly decreased within the first 30 minutes. The values then slowly continued to decrease until a quasi-steady state was achieved after 1.5 hours. As is evident from the graph, the 250 µm coating is more noble, followed by the 500 µm and 375 µm coatings. The 500 µm and 375 µm follow the same trend in the OCP test until around 2000 seconds,

at this point the 500 µm starts to stabilise while the 375 µm continues to decrease. The most probable reason for these differences in OCP is likely the result of variations in the microstructure which were discussed in section 4.2. The thicker coatings have a higher ability to close pore size, however, it is likely that this effect is overruled by the tensile residual stresses which are in turn more present in the thicker coatings and especially in the 375 µm coating. Furthermore, it was explained that oxidation has a negative influence on corrosion resistance which increases with coating thickness.

The response of the substrate was different, first displacing to a more negative value before rising and subsequently stabilizing at around -0.49 V, this response indicates an immediate attack of the surface followed by the formation of a protective film. The OCP of the carbon steel is lower than the recorded OCP of the thermal sprayed coatings.

4.4.4 Potentiodynamic polarization (PDP)

Potentiodynamic polarization (PDP) tests were performed to compare the electrochemical behaviour of the coatings and substrate in a corrosive environment. Results of these tests performed in 0.5 M H_2SO_4 and 5g/L Thiourea are displayed in figure 4.34, showing the cathodic and anodic branch of the S235JR substrate and three coatings. The corresponding values in terms of Ecorr, icorr and corrosion rate are displayed in table 4.5. Polarization curves for the 250, 375 and 500 µm coatings show a similar trend. What can be observed is that the curves shift to a higher current density as the coatings get thicker. The curves for the 375 and 500 µm coatings show more similarity compared to the 250 µm coating, which is consistent with observations from the OCP test. The coatings reach a potential range with a lower corrosion rate of around 0.25 V and enter the transpassive region at around 0.9 V. The 'critical current density' and 'passivation potential' are lower for the 250 µm indicating that it reduces the corrosion rate and performs slightly better than the other two coatings. The start of the trans-passive zone is comparable for all coatings, starting around 0.9 V.

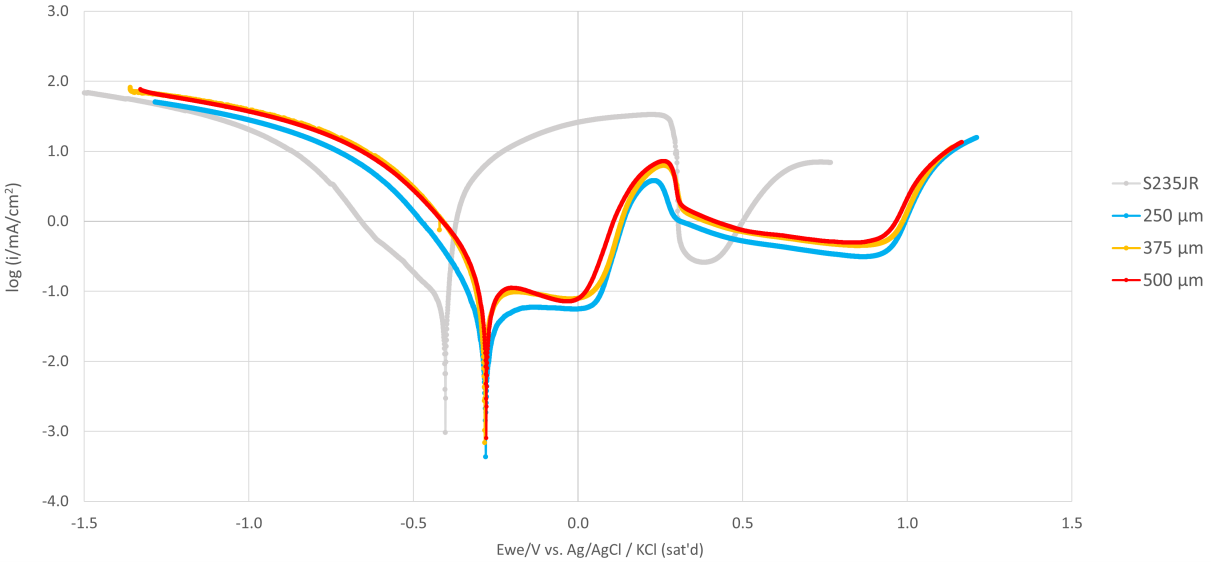

Figure 4.34: Potentiodynamic polarization diagrams of thermal sprayed coatings (250,375,500 µm and S235JR carbon steel in 0.5 M H_2SO_4 + 5g/L Thiourea

The curve of the S235JR carbon steel substrate is shifted to the upper left corner relative to the coatings, indicating that it has a higher tendency to corrode. The curve follows a gradual decrease in current density as the potential becomes more positive. The corrosion rate is reduced in the range of 0.2 to 0.3 V where the current density quickly drops and reaches a plateau, around 0.4 V the current density continues to rise where after it enters the transpassive region. The calculated potential values for Ecorr, respectively -282.4, -284.1

	Ecorr (mV)	icorr (µA/cm^2)	Corrosion rate (mmpy)
S235JR	-408 ± 3	33 ± 1	0.82 ± 0.03
250 µm	-282 ± 2	7 ± 1	0.05 ± 0.01
375 µm	-284 ± 2	20 ± 1	0.13 ± 0.01
500 µm	-279 ± 1	24 ± 3	0.15 ± 0.02

Table 4.5: Results of tafel plots with SD, in 0.5 M H_2SO_4 and 5g/L Thiourea

and -279.1 mV, reveal similarity in terms of corrosion potential. A significant difference can however be observed in current density. The plot for thicker coatings shifts to higher current densities, indicating that a lower thickness has a more favourable microstructure. Additionally, a conclusion which could be drawn is that microcracks and oxidation have a higher impact than porosity. The calculated icorr values for the coatings are found to be respectively 7.2, 20.1 and 23.5 µmA/cm^2, this result shows again that the 375 and 500 µm coatings have a more similar electrochemical behaviour than the 250 µm coating. The icorr for the substrate is substantially higher than for the coatings. The corrosion rate shows a similar trend as the icorr values.

4.4.5 Cathodic Charging

The coated samples with increasing thickness and S235JR carbon steel were cathodically charged for 16 hours in 0.5 M H_2SO_4 + 5g/L Thiourea. To prevent excessive hydrogen diffusion from the samples, samples were promptly sectioned, mounted and polished. Microhardness measurements were conducted after approximately 2 hours after the extraction from the cell. Subsequently, samples were analysed with OM and SEM-EDS to examine the microstructure and identify thickness reduction. Figure 4.35 and 4.36 show the results of microhardness measurements from section 4.3 compared with the microhardness of the samples after cathodic charging. The line in these graphs are second-order polynomial trendline in order to correctly fit the measurements and reduce fluctuations. Since part of the coating dissolved during the charging experiment, it was not possible to perform the same number of indentations.

The results show that there is not much difference between the uncharged and charged specimens in terms of microhardness. There is variation, but this can be attributed to the HV0.3 measurement error. For the coatings, it is remarkable that no difference after charging is detected since this method has been used in multiple studies with NiCrMoW bulk material in similar conditions [211–213]. The difference from these studies is that the NiCrMoW is applied by thermal spraying. It is likely that the microstructure of the thermal sprayed coatings has led to these deviating results. A hypothesis is that no difference could

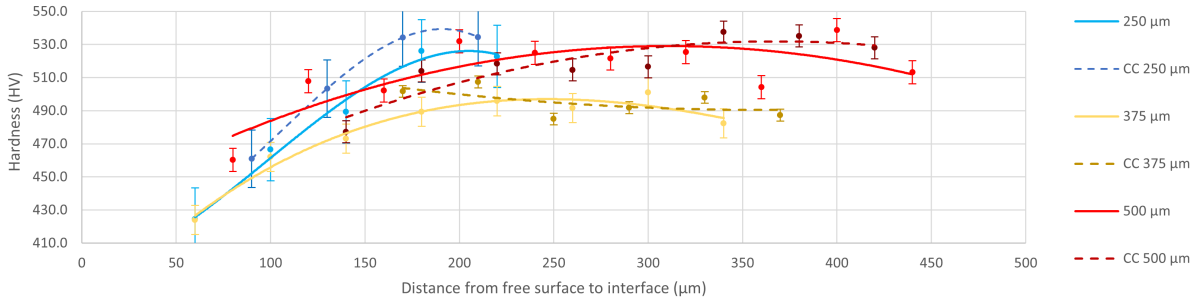

Figure 4.35: Coating microhardness after cathodic charging for 16 hours in 0.5 M H_2SO_4 + 5g/L Thiourea at room temperature

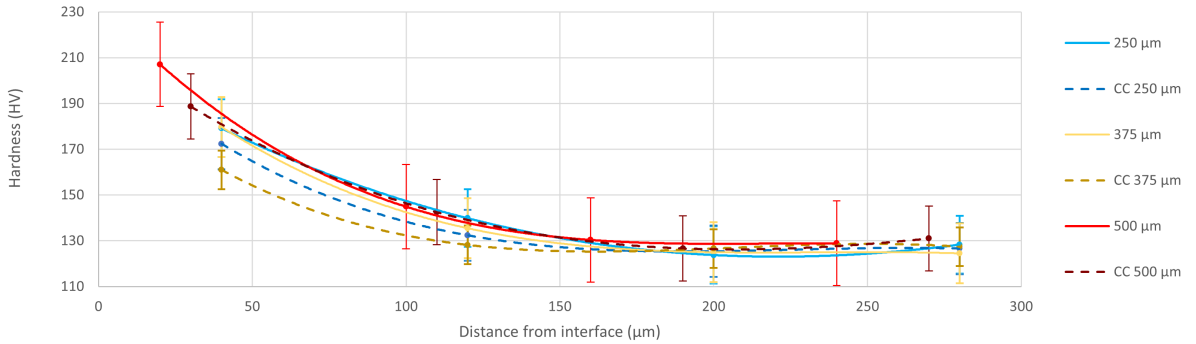

Figure 4.36: Substrate microhardness after cathodic charging for 16 hours in 0.5 M H_2SO_4 + 5g/L Thiourea at room temperature

be measured due to the nature of the microstructures of thermal sprayed coatings. As thoroughly explained, these microstructures consist of many splat boundaries, cracks and porosity which can act as high-diffusivity paths and hydrogen traps. Additionally, diffusion can be affected by oxide layers and residual stresses. A recent study [214] found that diffusion of hydrogen in thermal sprayed stainless steel is relatively high. Furthermore, recent studies [215–217] suggest that traps are found to suppress the accumulation of hydrogen necessary for hydrogen embrittlement. One study [148] found that 316L thermal sprayed coatings had 23 times more reversible traps than 'normal' ferritic steels due to the porous microstructure. A possible explanation could thus be that the coating, when charged with hydrogen, can more effectively trap hydrogen ultimately reducing hydrogen embrittlement. Additionally, the fast diffusion kinetics of the coating may play a role in relieving hydrogen embrittlement after charging. A second hypothesis is based on a study from Iost and Vogt [218]. It was found that hydrogen charged samples have an increase in compressive stresses in the γ-lattice which increased microhardness. Given that there is already a high presence of residual stress in the thermal sprayed coatings the effect of hydrogen charging could be suppressed.

The microhardness of the substrate before and after charging shows an identical initial decrease from 210 HV to 130 HV in the first 150 µm. As discussed in section 4.3, the

elevated surface hardness can be attributed to gritblasting, which induces compressive stresses through the effects of shot peening. Figure 4.36 indicates that the microhardness of the charged samples is reduced compared to the uncharged samples within this initial 150 µm. This outcome is unexpected, as the hardness is anticipated to increase after hydrogen charging. The error bars in the figure represent the standard deviation of the measurements. Despite this unexpected result and the observed deviations, it can be assumed that the decrease in hardness is not statistically significant. Based on this result, it can be concluded that the thermal sprayed coatings effectively protected the substrate from hydrogen embrittlement.

Figure 4.37 shows optical microscopy images of cross-sections of the three coatings after cathodic charging. As is evident all coatings show significant corrosion attack of the outer layer. The surface at higher magnification is depicted in figure 4.38, what is clearly visible is the attack by pitting corrosion on the surface. Furthermore, the unmelted particles close to the surface show disbonding from the coating microstructure. This may indicate that the interface of the particles serves as trap sites for hydrogen, which further strengthens the hypothesis that hydrogen is effectively trapped in the coating. Alternatively, these cracks may have formed due to penetration of the electrolyte. Unmelted particles located further from the surface show significantly less cracking.

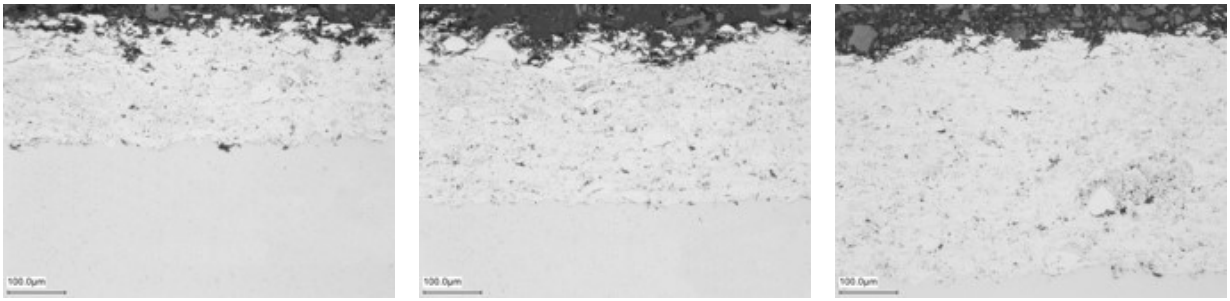

Figure 4.37: Cross-sections after cathodic charging for 16 hours in 0.5 M H_2SO_4 + 5g/L Thiourea at room temperature

Table 4.6 displays the total reduction of thickness and standard deviation. Overall, the reduction in all coatings is quite large. It is important to note that the corrosive environment used in this test is not a good reflection of the real environment for which the coatings are intended. However, it is an effective method to compare the effect of corrosion attack. It is clear that the largest reduction has occurred in the 375 µm coatings, followed by the 500 µm and 250 µm coatings. This is not surprising as these results show an identical hierarchy as in the previously discussed tests. This implies that the 250 µm coating shows the highest corrosion resistance, followed by the 500 µm and at last the 375 µm coating. A possible explanation could be that the higher residual stress in the 375 µm results in a higher corrosion rate. Furthermore, the higher degree of oxidation in the 375 µm and 500 µm coatings is likely to have resulted in higher corrosion rates.

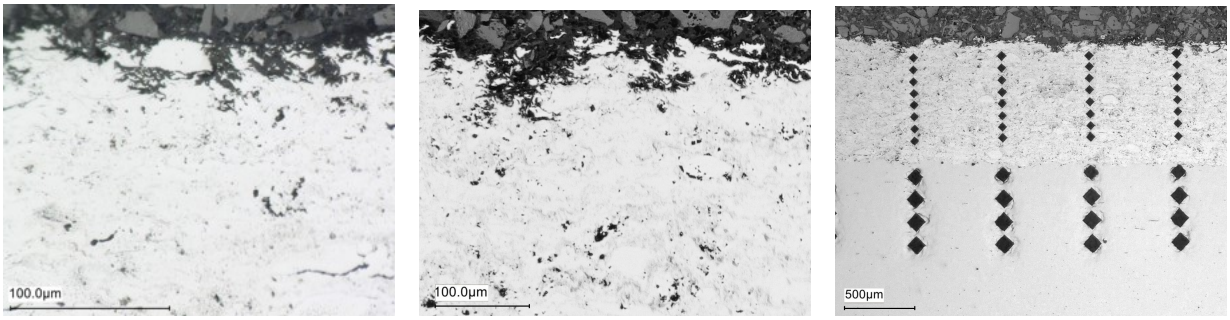

Figure 4.38: Cross-sections of two 500 µm coatings showing pitting of the surface and at last a cross-section with a set of indentations on coating and substrate

	Initial coating thickness (µm)	Thickness after charging (µm)	Difference (µm)
250 µm	250.7 ± 15.2	197.8 ± 19.4	52.9
375 µm	353.4 ± 14.8	271.4 ± 15.8	82.1
500 µm	440.7 ± 5.6	374.3 ± 11.3	66.4

Table 4.6: Thickness reduction and SD after cathodic charging in 0.5 M H_2SO_4 and 5g/L thiourea at 5 mA/ cm^2

5

Conclusions

This study investigated the impact of HVAF thermal sprayed NiCrMoW coatings and coating thickness on the HIC resistance of carbon steel in sour environment. The research is built upon a comprehensive literature review covering HE mechanisms, HIC, thermal sprayed coatings, HIC protection requirements, HVAF, and coating materials. Experiments were conducted to address four research questions which emerged from knowledge gaps in the literature. This chapter is dedicated to addressing these questions, which collectively form the thesis conclusions.

What impact does the thickness of HVAF thermal sprayed NiCrMoW coatings have on its microstructure, defects, and properties?

- The quality of all coatings was found to be excellent with none of the coatings exceeding a porosity volume fraction above 1%. With increasing coating thickness, the total volume fraction of porosity and pore size decreased, likely through the combined effect of longer heating and shot peening. Oxidation increased with coating thickness due to more frequent and longer cooling times. The surface roughness was found to be unaffected by coating thickness.
- Three zones with distinct residual stress characteristics could be identified in the coatings from subsurface microhardness measurements. (I) From the surface to 200 µm depth: Transition from tensile to compressive stresses, influenced by shot peening and quenching. (II) 200 µm depth and onward: Residual stress stabilized and a direct relationship with coating thickness; this zone was notably absent in the 250 µm coating, suggesting a unique behaviour in thicker coatings. (III) Last 50 µm up to substrate interface: Tensile stresses attributed to a mismatch in CTE.
- A remarkable unknown deviation in residual stress was found for the 375 µm coatings, suggesting an elevated amount of residual tensile stress.

Can HVAF thermal sprayed NiCrMoW coatings effectively protect carbon steel against HIC in sour environments?

- Hydrogen blisters were present on the surface of the uncoated samples, along with evidence of corrosion and HIC damage. In contrast, the coated samples did not show any damage.
- The CLR, CTR, and CSR for the uncoated carbon steel were significantly above the

acceptance range, while the ratios for the coated samples were well below this range. Due to the excellent corrosion resistance, uniformity, and absence of through-coating porosity in the microstructure, the thermal sprayed HVAF NiCrMoW coatings effectively protected carbon steel from HIC in sour environment.

- No significant difference was found between the 250, 375, 500 µm coatings in terms of CLR, CTR, and CSR. Demonstrating that varying the coating thickness had no impact in terms of protection against HIC.

What is the effect of coating thickness on the electrochemical behaviour of HVAF thermal sprayed NiCrMoW?

- Open circuit potential and potentiodynamic polarization measurements showed a higher resemblance in electrochemical behaviour between the 375 and 500 µm coatings than with the 250 µm coatings.
- No significant difference was recorded for the corrosion potential (Ecorr) in all coatings, which was expected for coatings of the same material. The icorr (corrosion current density) and corrosion rate both increased significantly with coating thickness, as a result from a higher level of residual stress and oxidation.
- Material loss in cathodic charging experiments revealed that the 250 µm coatings offered the highest corrosion resistance, followed by the 500 µm coatings, with the 375 µm coatings exhibiting the lowest resistance to corrosion. A complex relationship was found between microstructural differences, corrosion resistance, and electrochemical behaviour. The residual stress led to high corrosion rates while oxidation especially influenced electrochemical behavior.
- Subsurface microhardness measurements before and after cathodic charging revealed no perceivable difference. Two explanations are (I) the coating effectively traps hydrogen in porosities and splat boundaries during charging, reducing hydrogen embrittlement. (II) The presence of substantial pre-existing compressive residual stresses in the coatings suppresses the effect of embrittlement on hardness.

What is the impact of galvanic interaction between the NiCrMoW coating and the carbon steel substrate in a sour environment, and how is this influenced by coating thickness?

- No evidence of HIC could be found in the galvanic corrosion samples. Hydrogen absorption was limited due to the small surface area of the holiday region.
- The corrosion rate of carbon steel increased by 66% due to galvanic interactions with the NiCrMoW coatings.
- The effect of coating thickness on galvanic interaction is negligible, caused by their similar electrochemical properties and only minor variations in cathode-to-anode surface ratios.
- Given the elevated corrosion rate from galvanic interaction, it becomes critical to ensure that the coatings are free of through-coating defects and capable of withstanding holiday formation. Consequently, a thicker coating may offer more protection as it possesses a higher capacity to close pores and provides a substantially greater physical barrier.

6

Recommendations

With this study, the foundation of research on the use of HVAF thermal sprayed coatings for use in sour environments to prevent HIC in carbon steels was established. It was concluded that thermal sprayed NiCrMoW coatings have a high potential to be used in the oil and gas industry. It is important that further research is conducted in a number of areas before such coatings can be successfully implemented. The diagram in figure 6.1 displays recommended areas, this section will discuss and explain their importance.

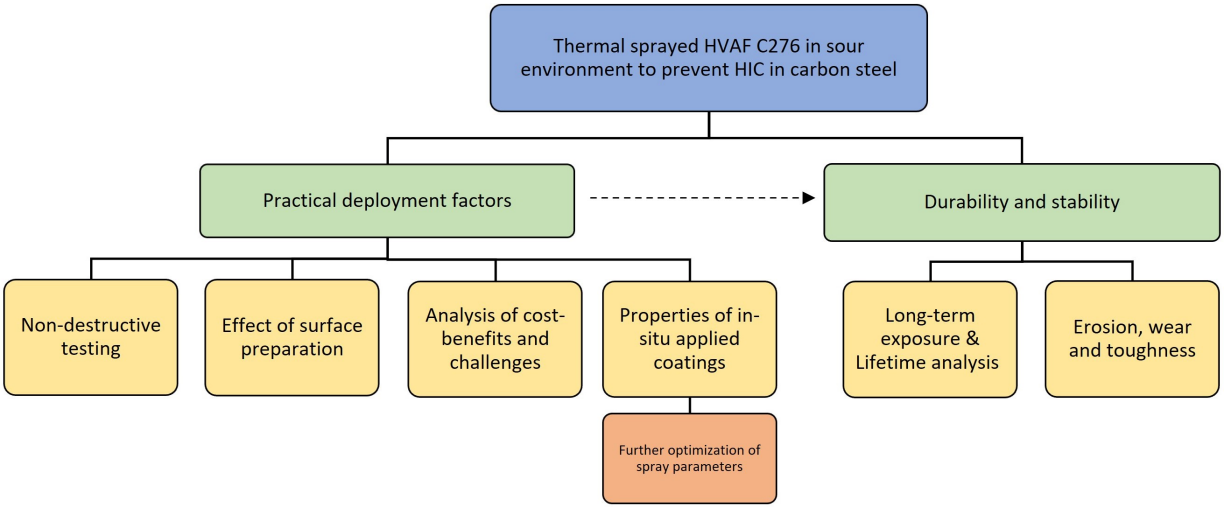

Figure 6.1: Directions for future work based on the findings of the theoretical background and experiments of this study

Practical deployment factors

Thermal sprayed coatings have proven their durability and performance in a substantial amount of literature. The successful implementation however depends on a versatile understanding of practical factors that influence effectiveness and reliability. These factors should be thoroughly explored for this type of coating to ensure that unexpected issues do not arise before, during or after deployment. Four critical research directions are discussed below.

Non-destructive testing and maintenance

It is necessary to identify the effects and consequences of thermal sprayed coatings on inspection. Periodic inspection is performed in the oil and gas industry to examine the condition of equipment and coatings. NDT is employed to identify risks from flaws, defects or excessive material loss. Due to the relatively porous nature of thermal sprayed coatings, these instruments may not provide reliable measurements. Research should be conducted on HVAF NiCrMoW test coupons and focus on:

- Testing the usability of current NDT techniques such as ultrasonic testing, eddy current testing, radiography and visual inspection.
- Identification of alternative techniques such as infrared flash thermography, pulsed eddy current testing and phased array ultrasonic testing [219].

Furthermore, coating maintenance should be explored: it is particularly important to develop strategies for maintaining or restoring coating integrity during extended service to enhance the overall longevity of the coatings. Examples are for instance:

- Use of organic sealants, such as epoxy, polyurethane, polyvinyl esters, polyester, phenolics or silicone-based sealants [16].
- Inorganic sealants, such as Sol-Gel method or thermal sprayed overlay. These offer higher resistance in high temperatures and better wear resistance than organic sealants, with the downside that these are more complex and have a higher cost [220].

Effect of surface preparation

In the theoretical background of this thesis, it was explained that an improperly prepared substrate has serious consequences on splat formation, which may result in unwanted coating properties such as excessive oxidation, porosity or delamination. The coatings will likely be applied on equipment which is affected by surface defects from HIC blistering, cracking or pitting. The following research directions should be explored:

- What is the effect on thermal sprayed coating properties (for example on microstructure and adhesion) when applied on carbon steel with surface irregularities and corrosion after sour service exposure?
- To what degree do surface pits and blisters have to be repaired or grinded before adequate adhesion can be guaranteed?

If the results indicate that coating performance is significantly reduced, further research should be focused on:

- Identification of adequate grit material and effect of grit size for the preparation of substrates with abrasive blasting to obtain a propper surface profile and cleanliness.
- The effect of cleaning methods such as solvent cleaning or abrasive cleaning to remove contaminants such as old coatings and oils.

Properties of in-situ applied coatings

The coatings in this study were fabricated in perfect conditions with fixed spray distance, angle and lateral movement. Poor spray conditions can affect the microstructure, proper-

ties and local differences in thickness. Some literature can already be found, however, a more thorough analysis of coherent effects is missing on the following topics

- Coatings should be applied in an in-situ environment to identify the effect on coating properties.
- Coatings in different conditions should be sprayed with deliberate defects which are associated with in-situ application, analyzed in a similar way as this study, and compared with the results from this study.
- Coating quality and residual stress depend on the preheating of the substrate surface. In this study, the substrate was kept at a minimal temperature of 65 - 90 °C before each pass and a maximum temperature of 130 °C. It might be more difficult to control this temperature when applying a coating in-situ and thus the effect or constraints should be identified.

Following the identification of the properties of in-situ applied coatings, it is essential to determine the most favourable spray parameters. To highlight the importance of this it was chosen to introduce a fourth layer within the diagram.

Analysis of cost-benefits and challenges

A comprehensive cost-benefit analysis should be performed which takes factors into account such as material costs, application time, labour time, equipment setup, and downtime from coating application and set them against the benefits of increased equipment lifespan and reduced maintenance costs. Furthermore, there may be challenges associated with the implementation of HVAF for example in terms of safety during application which should be thoroughly explored.

Durability and stability

This study explored whether the coatings are fit-for-service, an estimation of lifetime could not be made. Long-term exposure, environmental factors beyond sour service and mechanical behaviour are important aspects which should be investigated to a further extent. Figure 6.1 shows that practical deployment factors and durability and stability are connected. It is important that both research directions are associated with each other as they are closely linked.

Long-term exposure and lifetime analysis

Experiments should be conducted to determine the lifetime of the coatings and in what way long-term exposure affects coating performance. Current tests were relatively short but gave a solid understanding of resistance in a sour environment. Further research should focus on the following topics:

- A field test with the use of thermal sprayed corrosion coupons should be conducted in-situ to test coatings in a real-life environment.
- Long-term galvanic interaction should identify the enduring effects of galvanic interaction between coatings and substrate materials in corrosive sour environments.
- Consider how variations in environmental conditions such as temperature, humidity, and chemical exposure influence long-term coating performance.

Erosion, wear and toughness

The resistance of the coating to erosion and wear should be investigated. As explained in the conclusion it is extremely important that the coating does not develop defects from manufacturing or during service as this can cause galvanic corrosion. Since the thickness of the coating did not have a significant influence on HIC resistance, the required thickness will depend on other factors such as erosion and wear resistance and toughness. The following tests should be included on HVAF thermal sprayed NiCrMoW coatings with different thicknesses:

- Wet slurry abrasion test, such as ASTM G75 [221], to identify erosion behaviour.
- Identification of fracture toughness with Charpy impact testing (ISO 148-1 [222]) and inspection of the fracture surface with SEM.

References

[1] Roman Bender et al. "Corrosion challenges towards a sustainable society". In: *Materials and Corrosion* 73.11 (July 2022), pp. 1730–1751. DOI: 10.1002/maco.202213140.

[2] MB Kermani et al. "The impact of corrosion on the oil and gas industry". In: *SPE Production & Facilities* 11.03 (1996), pp. 186–190.

[3] Branko N. Popov et al. *Hydrogen permeation and hydrogen-induced cracking*. Elsevier Inc., June 2018, pp. 133–162. DOI: 10.1016/B978-0-323-52472-8.00007-1.

[4] Gyu Tae Park et al. "Effect of microstructure on the hydrogen trapping efficiency and hydrogen induced cracking of linepipe steel". In: *Corrosion Science* 50.7 (July 2008), pp. 1865–1871. DOI: 10.1016/j.corsci.2008.03.007.

[5] Roger A. King. "Sulfide stress cracking". In: *Trends in Oil and Gas Corrosion Research and Technologies*. Elsevier, 2017, pp. 271–294. DOI: 10.1016/b978-0-08-101105-8.00011-5.

[6] N Bailey et al. *Welding Steels Without Hydrogen Cracking*. Woodhead Publishing, Aug. 1993.

[7] Jonathan A Lee. "Hydrogen embrittlement". In: *National Aeronautics and Space Administration* (2016).

[8] Iain Hall et al. "Application of HVAS Cladding to mitigate Sulfide Stress Cracking and Hydrogen Induced Cracking in a De-ethanizer Column". In: *CORROSION 2015*. OnePetro. 2015.

[9] A. Verstak et al. "High Velocity Air-Fuel Spraying and Its Applications in Oil and Gas Industry". In: *International Thermal Spray Conference*. Ed. by R.S. Lima et al. ASM International, May 2012. DOI: 10.31399/asm.cp.itsc2012p0529.

[10] João CB Bertoncello et al. "Effects of thermal spray aluminium coating on SSC and HIC resistance of high strength steel in a sour environment". In: *Surface and Coatings Technology* 399 (2020), pp. 126–156.

[11] A Verstak et al. "Activated combustion HVAF coatings for protection against wear and high temperature corrosion". In: *Thermal Spray* 1 (2003), p. 58.

[12] S. Paul. "Mitigating Corrosion of Carbon Steel in Supercritical CO2 Environments Using HVOF Coatings". In: *International Thermal Spray Conference*. Ed. by A. Agarwal et al. ASM International, May 2015. DOI: 10.31399/asm.cp.itsc2015p1072.

[13] *Corrosion of Carbon Steel in Supercritical CO2/H_2S and Its Mitigation Using Coatings*. Vol. All Days. NACE CORROSION. NACE-2019-12768. Mar. 2019. eprint:

https://onepetro.org/NACECORR/proceedings-pdf/CORR19/All-CORR19/NACE-2019-12768/1134800/nace-2019-12768.pdf.

[14] Bruce D Craig et al. "Corrosion Resistant Alloys (CRAs) in the oil and gas industry". In: *Nickel Institute Technical Series* 1 (2011), p. 0073.

[15] D. J. Greving et al. "Effects of coating thickness and residual stresses on the bond strength of ASTM C633-79 thermal spray coating test specimens". In: *Journal of Thermal Spray Technology* 3.4 (Dec. 1994). DOI: 10.1007/bf02658982.

[16] Lech Pawlowski. *The science and engineering of thermal spray coatings*. John Wiley & Sons, 2008.

[17] Alec Groysman. "Corrosion Problems and Solutions at Oil Refinery and Petrochemical Units". In: *Topics in Safety, Risk, Reliability and Quality*. Springer International Publishing, Oct. 2016, pp. 37–99. DOI: 10.1007/978-3-319-45256-2_4.

[18] Teresa E. Perez. "Corrosion in the Oil and Gas Industry: An Increasing Challenge for Materials". In: *JOM* 65.8 (July 2013), pp. 1033–1042. DOI: 10.1007/s11837-013-0675-3.

[19] Sankara Papavinasam. *Corrosion control in the oil and gas industry*. Elsevier, 2013.

[20] Palash Kumar Bhowmik et al. "Corrosion and its control in crude oil refining process". In: *6th International Mechanical Engineering & 14th Conference Annual Paper Meet, Dhaka, Bangladesh*. 2012.

[21] Rolf Nyborg et al. "Understanding and prediction of mesa corrosion attack". In: (2003).

[22] D.A. Jones. *Principles and Prevention of Corrosion*. Prentice Hall, 1996.

[23] IEA. "World Energy Outlook 2022". In: (2022).

[24] Anupama R Prasad et al. "Corrosion inhibition in oil and gas industry: Economic considerations". In: *Corrosion inhibitors in the oil and gas industry* (2020), pp. 135–150.

[25] Jacqueline Michel et al. "Oil Spills: Causes, consequences, prevention, and countermeasures". In: *Fossil fuels: current status and future directions*. World Scientific, 2016, pp. 159–201.

[26] M. Iannuzzi et al. "The carbon footprint of steel corrosion". In: *npj Materials Degradation* 6.1 (Dec. 2022). DOI: 10.1038/s41529-022-00318-1.

[27] Sandeep Kumar Dwivedi et al. "Hydrogen embrittlement in different materials: A review". In: *International Journal of Hydrogen Energy* 43.46 (2018), pp. 21603–21616. DOI: 10.1016/j.ijhydene.2018.09.201.

[28] Stan Lynch. "Hydrogen embrittlement phenomena and mechanisms". In: *Corrosion reviews* 30.3-4 (2012), pp. 105–123.

[29] H.K. Birnbaum et al. "Hydrogen-enhanced localized plasticity—a mechanism for hydrogen-related fracture". In: *Materials Science and Engineering: A* 176.1-2 (Mar. 1994), pp. 191–202. DOI: 10.1016/0921-5093(94)90975-x.

[30] J Song et al. "Mechanisms of hydrogen-enhanced localized plasticity: an atomistic study using α-Fe as a model system". In: *Acta Materialia* 68 (2014), pp. 61–69.

[31] Michael Janssen et al. *Fracture Mechanics*. CRC Press, Aug. 2004. DOI: 10.1201/9781482265583.

[32] Alexander R. Troiano. "The Role of Hydrogen and Other Interstitials in the Mechanical Behavior of Metals". In: *Metallography, Microstructure, and Analysis* 5.6 (Nov. 2016), pp. 557–569. DOI: 10.1007/s13632-016-0319-4.

[33] SP Lynch. "Mechanisms of hydrogen assisted cracking–a review". In: *Hydrogen effects on material behaviour and corrosion deformation interactions* (2003), pp. 449–466.

[34] SP Lynch. "Metallographic contributions to understanding mechanisms of environmentally assisted cracking". In: *Metallography* 23.2 (1989), pp. 147–171.

[35] SP Lynch. "Progress towards understanding mechanisms of hydrogen embrittlement and stress corrosion cracking". In: *CORROSION 2007* (2007).

[36] Lynch S.P. et al. "Mechanisms of hydrogen assisted cracking - a review". In: *Hydrogen effects on materials behavior and corrosion deformation interactions* (2003), pp. 449–466.

[37] John W. Morse et al. "The chemistry of the hydrogen sulfide and iron sulfide systems in natural waters". In: *Earth-Science Reviews* 24.1 (1987), pp. 1–42. DOI: 10.1016/0012-8252(87)90046-8.

[38] M Miloshova et al. "New chalcogenide glass chemical sensors for S2-and dissolved H2S monitoring". In: *Water science and technology* 47.2 (2003), pp. 135–140.

[39] Stephen N Smith. "A proposed mechanism for corrosion in slightly sour oil and gas production". In: *12th international corrosion congress, Houston, TX*. 1993.

[40] Wei Sun et al. "Equilibrium Expressions Related to the Solubility of the Sour Corrosion Product Mackinawite". In: *Industrial &amp Engineering Chemistry Research* 47.5 (Feb. 2008), pp. 1738–1742. DOI: 10.1021/ie070750i.

[41] W Sun et al. "A mechanistic model of uniform hydrogen sulfide/carbon dioxide corrosion of mild steel". In: *Corrosion* 65.5 (2009), pp. 291–307.

[42] M Victoria Biezma. "The role of hydrogen in microbiologically influenced corrosion and stress corrosion cracking". In: *International Journal of Hydrogen Energy* 26.5 (2001), pp. 515–520.

[43] Mariano Iannuzzi. "Environmentally assisted cracking (EAC) in oil and gas production". In: *Stress corrosion cracking*. Elsevier, 2011, pp. 570–607.

[44] Russell D Kane et al. "Roles of H_2S in the behavior of engineering alloys: a review of literature and experience". In: *CORROSION 98* (1998).

[45] K. KIUCHI et al. "OVERVIEW NO. 27 - THE SOLUBILITY AND DIFFUSIVITY OF HYDROGEN IN WELL-ANNEALED AND DEFORMED IRON". In: *Perspectives in Hydrogen in Metals*. Ed. by M.F. ASHBY et al. Pergamon, 1986, pp. 29–52. DOI: 10.1016/B978-0-08-034813-1.50009-7.

[46] Andreas Drexler et al. "The role of hydrogen diffusion, trapping and desorption in dual phase steels". In: *Journal of Materials Science* 57.7 (Jan. 2022), pp. 4789–4805. DOI: 10.1007/s10853-021-06830-0.

[47] A McNabb et al. "A new analysis of diffusion of hydrogen in iron and ferritic steels". In: *Transactions of the Metallurgical Society of AIME* 227.3 (1963), p. 618.

[48] GM Pressouyre et al. "An example of the effect of hydrogen trapping on hydrogen embrittlement". In: *Metallurgical Transactions A* 12.5 (1981), pp. 835–844.

[49] Alfons HM Krom et al. "Hydrogen trapping models in steel". In: *Metallurgical and materials transactions B* 31.6 (2000), pp. 1475–1482.

[50] M Elboujdaini. *Corrosion and Corrosion Control Course, MAAE 4906C*. 2005.

[51] V.S. Raja et al. *Stress Corrosion Cracking*. Woodhead Publishing Series in Metals and Surface Engineering. Cambridge, England: Woodhead Publishing, 2016.

[52] K. O. Findley et al. "Critical Assessment 17: Mechanisms of hydrogen induced cracking in pipeline steels". In: *Materials Science and Technology* 31.14 (Nov. 2015), pp. 1673–1680. DOI: 10.1080/02670836.2015.1121017.

[53] N. Espallargas. *Introduction to thermal spray coatings*. Elsevier Inc., June 2015, pp. 1–13. DOI: 10.1016/B978-0-85709-769-9.00001-4.

[54] M. Elboujdaini et al. "Metallurgical factors in stress corrosion cracking (SCC) and hydrogen-induced cracking (HIC)". In: *Journal of Solid State Electrochemistry* 13.7 (Mar. 2009), pp. 1091–1099. DOI: 10.1007/s10008-009-0799-0.

[55] Damien Féron et al. *Corrosion issues in light Water reactors: stress corrosion cracking*. Vol. 51. Elsevier, 2007.

[56] Lei Fu et al. "Formation Criterion of Hydrogen-Induced Cracking in Steel Based on Fracture Mechanics". In: *Metals* 8.11 (Nov. 2018), p. 940. DOI: 10.3390/met8110940.

[57] Maria Jose Cancio et al. "Environmental and metallurgical parameters affecting sulfide stress cracking resistance of high strength steels". In: *CORROSION 2010*. OnePetro. 2010.

[58] Y. Kim et al. "On the Effect of Hydrogen on the Fracture Toughness of Steel". In: *International Journal of Fracture* 134.3-4 (Aug. 2005), pp. 339–347. DOI: 10.1007/s10704-005-1974-7.

[59] Jean-Gabriel Sezgin et al. "Simulation of the impact of internal pressure on the integrity of a hydrogen-charged Type-316L stainless steel during slow strain rate tensile test". In: *International Journal of Hydrogen Energy* 43.17 (2018), pp. 8558–8568. DOI: https://doi.org/10.1016/j.ijhydene.2018.03.125.

[60] Goutam Ghosh et al. "Hydrogen induced cracking of pipeline and pressure vessel steels: A review". In: *Engineering Fracture Mechanics* 199 (2018), pp. 609–618. DOI: 10.1016/j.engfracmech.2018.06.018.

[61] N. Nanninga et al. "Role of microstructure, composition and hardness in resisting hydrogen embrittlement of fastener grade steels". In: *Corrosion Science* 52.4 (2010), pp. 1237–1246. DOI: 10.1016/j.corsci.2009.12.020.

[62] D Pérez Escobar et al. "Combined thermal desorption spectroscopy, differential scanning calorimetry, scanning electron microscopy and X-ray diffraction study of hydrogen trapping in cold deformed TRIP steel". In: *Acta materialia* 60.6-7 (2012), pp. 2593–2605.

[63] Brandon Forero et al. "Susceptibility of pipeline girth welds to hydrogen embrittlement and sulphide stress cracking". In: *Materials and Corrosion* 65 (May 2014). DOI: 10.1002/maco.201206574.

[64] V. Venegas et al. "On the role of crystallographic texture in mitigating hydrogen-induced cracking in pipeline steels". In: *Corrosion Science* 53.12 (Dec. 2011), pp. 4204–4212. DOI: 10.1016/j.corsci.2011.08.031.

[65] M.A. Mohtadi-Bonab et al. "Texture, local misorientation, grain boundary and recrystallization fraction in pipeline steels related to hydrogen induced cracking". In: *Materials Science and Engineering: A* 620 (Jan. 2015), pp. 97–106. DOI: 10.1016/j.msea.2014.10.009.

[66] Mohammad Masoumi et al. "Effect of Grain Orientation and Boundary Distributions on Hydrogen-Induced Cracking in Low-Carbon-Content Steels". In: *JOM* 69.8 (Mar. 2017), pp. 1368–1374. DOI: 10.1007/s11837-017-2319-5.

[67] National Association of Corrosion Engineers. "Materials for use in H_2S-containing environments in oil and gas production". In: *NACE MR0175 ISO-15156-2 item 21306* (2015).

[68] National Association of Corrosion Engineers. "Metallic materials resistant to sulfide stress cracking in corrosive petroleum refining environments". In: *NACE MR0103-2012 item 21305* (2012).

[69] RP API. "Damage Mechanisms Affecting Fixed Equipment in the Refining Industry". In: *API 571, American Petroleum Institute* (2003), pp. 300–334.

[70] T Hara et al. *Conditions of Hydrogen-Induced Corrosion Occurrence of X65 Grade Line Pipe Steels in Sour Environments*. 2004, p. 1113.

[71] Jens Schröder et al. "Recent developments of sour service line pipe steels". In: 2006.

[72] J Kittel et al. "Hydrogen induced cracking (HIC) assessment of low alloy steel linepipe for sour service applications-Laboratory testing". In: *Eurocorr 2007*. 2007.

[73] Kris De Baere et al. "Study on alternative approaches to corrosion protection of ballast tanks using an economic model". In: *Marine Structures* 32 (2013), pp. 1–17.

[74] David A Osage. "API 579: A Comprehensive Fitness-for-Service Standard". In: *ASME Pressure Vessels and Piping Conference*. Vol. 41545. 2003, pp. 7-1 –7-22.

[75] Cornelius O. Emenike et al. "Optimisation of Carbon Steels for Sour Service". In: *All Days*. SPE, Oct. 2000. DOI: 10.2118/87261-ms.

[76] Liang Fan et al. "Corrosion Resistance of Transmission Pipeline Steel Coated with Five Types of Enamels". In: *Acta Metallurgica Sinica (English Letters)* 30.4 (Mar. 2017), pp. 390–398. DOI: 10.1007/s40195-017-0554-y.

[77] T. Valente. "Air plasma sprayed metallic coatings for sour environments". In: *British Corrosion Journal* 35.3 (Mar. 2000), pp. 189–194. DOI: 10.1179/000705900101501236.

[78] Faris M Alkordy. "Evaluation of Organic Protective Coatings as Corrosion Prevention for The Interior of Subsea Pipelines in Sour Gas Service". PhD thesis. DOI: 10.25148/etd.fidc000201.

[79] S. Chauhan et al. "Mechanical and Wear Characterization of GF Reinforced Vinyl Ester Resin Composites with Different Co-Monomers". In: *Journal of Reinforced Plastics and Composites* 28.21 (July 2008), pp. 2675–2684. DOI: 10.1177/0731684408093823.

[80] *Novel Internal Coating System for High Concentration H_2S Environments*. Vol. Day 2 Tue, February 22, 2022. IPTC International Petroleum Technology Conference. Feb. 2022. DOI: 10.2523/IPTC-22280-EA. eprint: https://onepetro.org/IPTCONF/proceedings-pdf/22IPTC/2-22IPTC/D021S041R004/2620424/iptc-22280-ea.pdf.

[81] Narayanan Rajagopalan et al. "Degradation mechanisms of amine-cured epoxy novolac and bisphenol F resins under conditions of high pressures and high temperatures". In: *Progress in Organic Coatings* 156 (2021), p. 106268. DOI: 10.1016/j.porgcoat.2021.106268.

[82] Salih Y Darweesh et al. "The effect of some physical and mechanical properties of cermet coating on petroleum pipes prepared by thermal spray method". In: *Journal of Failure Analysis and Prevention* 19.6 (2019), pp. 1726–1738.

[83] LN Moskowitz. "Application of HVOF thermal spraying to solve corrosion problems in the petroleum industry—an industrial note". In: *Journal of thermal spray technology* 2.1 (1993), pp. 21–29.

[84] Kalluri Anusha et al. "A Review on High-Velocity Oxy-Fuel (HVOF) Coating Technique". In: *Journal of The Institution of Engineers (India): Series D* (2023), pp. 1–18.

[85] Pierre Fauchais et al. "Thermal sprayed coatings used against corrosion and corrosive wear". In: *Advanced plasma spray applications* 10 (2012), p. 34448.

[86] Sadeghi Esmaeil et al. "Advances in Corrosion-Resistant Thermal Spray Coatings for Renewable Energy Power Plants. Part I: Effect of Composition and Microstructure". In: *Journal of Thermal Spray Technology* 28 (8 Dec. 2019), pp. 1749–1788. DOI: 10.1007/s11666-019-00938-1.

[87] "Chapter 4 - Thermal spray processes". In: *Engineering Coatings (Second Edition)*. Ed. by Stan Grainger et al. Second Edition. Woodhead Publishing Series in Metals and Surface Engineering. Woodhead Publishing, 1998, pp. 119–166. DOI: 10.1533/9781845698577.119.

[88] Ahsan Choudhuri et al. *Design Optimization of Liquid Fueled High Velocity Oxy-Fuel Thermal Spraying Technique for Durable Coating for Fossil Power Systems.* www.osti.gov, Nov. 2016. URL: https://www.osti.gov/servlets/purl/1356809 (visited on 01/27/2023).

[89] N. Bala et al. "Cold spray coating process for corrosion protection: a review". In: *Surface Engineering* 30.6 (2014), pp. 414–421. DOI: 10.1179/1743294413Y.0000000148.

[90] JA Browning. "Viewing the future of high-velocity oxyfuel (HVOF) and high-velocity air fuel (HVAF) thermal spraying". In: *Journal of Thermal Spray Technology* 8.3 (1999), p. 351.

[91] SL Liu et al. "Microstructure and properties of AC-HVAF sprayed Ni60/WC composite coating". In: *Journal of Alloys and Compounds* 480.2 (2009), pp. 254–258.

[92] A. Milanti et al. "Effect of spraying parameters on the microstructural and corrosion properties of HVAF-sprayed Fe–Cr–Ni–B–C coatings". In: *Surface and Coatings Technology* 277 (Sept. 2015), pp. 81–90. DOI: 10.1016/j.surfcoat.2015.07.018.

[93] Rajeev Dhiman et al. "Predicting splat morphology in a thermal spray process". In: *Surface and Coatings Technology* 201.18 (2007), pp. 7789–7801. DOI: 10.1016/j.surfcoat.2007.03.010.

[94] VV Sobolev et al. "Droplet-substrate impact interaction in thermal spraying". In: *Materials Letters* 28.4-6 (1996), pp. 331–335.

[95] CC Berndt. "Thermal spraying in japan". In: *Journal of Thermal Spray Technology* 5.3 (1996), pp. 352–367.

[96] Joseph R Davis et al. *Handbook of thermal spray technology.* ASM international, 2004, pp. 49–52.

[97] Jesper Carstensen et al. "Quality Control of Thermal Spray Coatings in Diesel Engines". In: *Practical Metallography* 50 (June 2013), pp. 369–390. DOI: 10.3139/147.110253.

[98] S Sampath et al. "Substrate temperature effects on splat formation, microstructure development and properties of plasma sprayed coatings Part I: Case study for partially stabilized zirconia". In: *Materials Science and Engineering: A* 272.1 (1999), pp. 181–188. DOI: 10.1016/S0921-5093(99)00459-1.

[99] Jo Ann Gan et al. "Review on the oxidation of metallic thermal sprayed coatings: A case study with reference to rare-earth permanent magnetic coatings". In: *Journal of thermal spray technology* 22 (2013), pp. 1069–1091.

[100] P Fauchais et al. "Knowledge concerning splat formation: an invited review". In: *Journal of thermal spray technology* 13.3 (2004), pp. 337–360.

[101] Rajeev Dhiman et al. "Predicting splat morphology in a thermal spray process". In: *Surface and Coatings Technology* 201.18 (June 2007), pp. 7789–7801. DOI: 10.1016/j.surfcoat.2007.03.010.

[102] D Zhang et al. “Microstructure formation and corrosion behaviour in HVOF-sprayed Inconel 625 coatings”. In: *Materials Science and Engineering: A* 344.1-2 (2003), pp. 45–56.

[103] S. Deshpande et al. “Mechanisms of oxidation and its role in microstructural evolution of metallic thermal spray coatings—Case study for Ni–Al”. In: *Surface and Coatings Technology* 200.18-19 (May 2006), pp. 5395–5406. DOI: 10.1016/j.surfcoat.2005.07.072.

[104] Yongang Zhang et al. “Effect of particle pre-oxidation on Ni and Ni20Cr splat formation during plasma spraying”. In: *Surface and Coatings Technology* 393 (July 2020), p. 125849. DOI: 10.1016/j.surfcoat.2020.125849.

[105] Jo Ann Gan et al. “Review on the Oxidation of Metallic Thermal Sprayed Coatings: A Case Study with Reference to Rare-Earth Permanent Magnetic Coatings”. In: *Journal of Thermal Spray Technology* 22.7 (July 2013), pp. 1069–1091. DOI: 10.1007/s11666-013-9955-2.

[106] S Matthews et al. “The effect of heat treatment on the oxidation mechanism of blended powder Cr3C2-NiCr coatings”. In: *Journal of thermal spray technology* 19.1 (2010), pp. 119–127.

[107] C-J Li et al. “Relationships between the microstructure and properties of thermally sprayed deposits”. In: *Journal of thermal spray technology* 11.3 (2002), pp. 365–374.

[108] M. Campo et al. “Corrosion resistance of thermally sprayed Al and Al/SiC coatings on Mg”. In: *Surface and Coatings Technology* 203.20 (2009), pp. 3224–3230. DOI: 10.1016/j.surfcoat.2009.03.057.

[109] S. Y. Tsai et al. *The use of thermal-spray coatings for preventing wet Hsub 2S cracking in HSLA steel plates*. 1997.

[110] TW Clyne et al. “Residual stresses in thermal spray coatings and their effect on interfacial adhesion: a review of recent work”. In: *Journal of thermal spray technology* 5 (1996), pp. 401–418.

[111] P. Araujo et al. “Residual stresses and adhesion of thermal spray coatings”. In: *Surface Engineering* 21.1 (Feb. 2005), pp. 35–40. DOI: 10.1179/174329405x30020.

[112] Florida State University. “Plasma Spray Process”. In: URL: https://eng-web1.eng.famu.fsu.edu/~shih/eml3016/lecture-notes/plasma%5C%20spray.ppt..

[113] Reeti Singh et al. “Influence of coating thickness on residual stress and adhesion-strength of cold-sprayed Inconel 718 coatings”. In: *Surface and coatings technology* 350 (2018), pp. 64–73.

[114] Gourhari Ghosh et al. “Understanding the role of surface roughness on the tribological performance and corrosion resistance of WC-Co coating”. In: *Surface and Coatings Technology* 378 (2019), p. 125080.

[115] Matteo Federici et al. “Effect of roughness on the wear behavior of HVOF coatings dry sliding against a friction material”. In: *Wear* 368 (2016), pp. 326–334.

[116] R.S.C. Paredes et al. “The effect of roughness and pre-heating of the substrate on the morphology of aluminium coatings deposited by thermal spraying”. In: *Surface*

and Coatings Technology 200.9 (2006), pp. 3049–3055. DOI: 10.1016/j.surfcoat.2005.02.200.

[117] MP Kanouff et al. "Surface roughness of thermal spray coatings made with off-normal spray angles". In: *Journal of thermal spray technology* 7.2 (1998), pp. 219–228.

[118] Tanya J. Levingstone et al. "Plasma sprayed hydroxyapatite coatings: Understanding process relationships using design of experiment analysis". In: *Surface and Coatings Technology* 283 (2015), pp. 29–36. DOI: 10.1016/j.surfcoat.2015.10.044.

[119] Xing Gao et al. "Effects of fuel types and process parameters on the performance of an activated combustion high velocity air-fuel (AC-HVAF) thermal spray system". In: *Journal of Thermal Spray Technology* (2021), pp. 1–16.

[120] Stephan Zimmermann et al. "Characterization of an Axial-Injection Plasma Spray Torch". In: *Journal of Thermal Spray Technology* 30.7 (July 2021), pp. 1724–1736. DOI: 10.1007/s11666-021-01235-6.

[121] Fuqiang Liu et al. "Numerical Analysis of the Activated Combustion High-Velocity Air-Fuel Spraying Process: A Three-Dimensional Simulation with Improved Gas Mixing and Combustion Mode". In: *Materials* 14.3 (Jan. 2021), p. 657. DOI: 10.3390/ma14030657.

[122] A. Allimant et al. "Progress in gas atomization of liquid metals by means of a De Laval nozzle". In: *Powder Technology* 190.1-2 (Mar. 2009), pp. 79–83. DOI: 10.1016/j.powtec.2008.04.071.

[123] Hao-Ran Jiang et al. "Numerical Investigation of In-Flight Behavior of Fe-Based Amorphous Alloy Particles in AC-HVAF Thermal Spray Process". In: *Journal of Thermal Spray Technology* 28.6 (July 2019), pp. 1146–1159. DOI: 10.1007/s11666-019-00889-7.

[124] Mehdi Jadidi et al. "A Comprehensive Review on Fluid Dynamics and Transport of Suspension/Liquid Droplets and Particles in High-Velocity Oxygen-Fuel (HVOF) Thermal Spray". In: *Coatings* 5.4 (Oct. 2015), pp. 576–645. DOI: 10.3390/coatings5040576.

[125] K. Bobzin et al. "Correlation Between Process Parameters and Particle In-flight Behavior in AC-HVAF". In: *Journal of Thermal Spray Technology* (Feb. 2023). DOI: 10.1007/s11666-023-01543-z.

[126] E. Sadeghimeresht et al. "A Comparative Study on Ni-Based Coatings Prepared by HVAF, HVOF, and APS Methods for Corrosion Protection Applications". In: *Journal of Thermal Spray Technology* 25.8 (Nov. 2016), pp. 1604–1616. DOI: 10.1007/s11666-016-0474-9.

[127] D Cheng et al. "The effect of particle size and morphology on the in-flight behavior of particles during high-velocity oxyfuel thermal spraying". In: *Metallurgical and Materials Transactions B* 32 (2001), pp. 525–535.

[128] Pierre L. Fauchais et al. *Thermal Spray Fundamentals*. Springer US, 2014. DOI: 10.1007/978-0-387-68991-3.

[129] D Cheng et al. “A numerical study of high-velocity oxygen fuel thermal spraying process. Part I: Gas phase dynamics”. In: *Metallurgical and Materials Transactions A* 32 (2001), pp. 1609–1620.

[130] Xing Gao et al. “Effects of Fuel Types and Process Parameters on the Performance of an Activated Combustion High Velocity Air-Fuel (AC-HVAF) Thermal Spray System”. In: *Journal of Thermal Spray Technology* 30.7 (Aug. 2021), pp. 1875–1890. DOI: 10.1007/s11666-021-01250-7.

[131] Alfredo Valarezo et al. “Effect of deposition rate and deposition temperature on residual stress of HVOF-sprayed coatings”. In: *Journal of Thermal Spray Technology* 29.6 (2020), pp. 1322–1338.

[132] Li Li et al. “Particle Characterization and Splat Formation of Plasma Sprayed Zirconia”. In: *Journal of Thermal Spray Technology* 15.1 (Mar. 2006), pp. 97–105. DOI: 10.1361/105996306x92668.

[133] Weiming Wang et al. “Numerical simulation of fluid flow and heat transfer in a plasma spray gun”. In: *The International Journal of Advanced Manufacturing Technology* 26.5-6 (Mar. 2005), pp. 537–543. DOI: 10.1007/s00170-004-2334-x.

[134] Zhenhua Cai et al. “The Effect of Spray Distance and Scanning Step on the Coating Thickness Uniformity in Cold Spray Process”. In: *Journal of Thermal Spray Technology* 23.3 (Oct. 2013), pp. 354–362. DOI: 10.1007/s11666-013-0002-0.

[135] Anita Hansbo et al. “Models for the simulation of spray deposition and robot motion optimization in thermal spraying of rotating objects”. In: *Surface and Coatings Technology* 122.2-3 (1999), pp. 191–201.

[136] S.H. Leigh et al. “Evaluation of off-angle thermal spray”. In: *Surface and Coatings Technology* 89.3 (1997), pp. 213–224. DOI: 10.1016/S0257-8972(96)02897-6.

[137] Sh. Khandanjou et al. “The detailed analysis of the spray time effects of the aluminium coating using self-generated atmospheric plasma spray system on the microstructure and corrosion behaviour”. In: *Results in Physics* 7 (2017), pp. 1440–1445. DOI: 10.1016/j.rinp.2017.04.014.

[138] Martha Ferrer et al. “EFFECT OF TEMPERATURE AND SUBSTRATE ROUGHNESS ON THE ADHESION OF COATINGS OF Ni ALLOY DEPOSITED BY FLAME SPRAY”. In: *La Revista Latinoamericana de Metalurgia y Materiales, RLMM* 37.2 (2017).

[139] Aeshah H. Alamri. “Localized corrosion and mitigation approach of steel materials used in oil and gas pipelines – An overview”. In: *Engineering Failure Analysis* 116 (Oct. 2020), p. 104735. DOI: 10.1016/j.engfailanal.2020.104735.

[140] Alireza Bahadori. “Chapter 2 - Engineering and Technical Guidelines for Painting”. In: *Essentials of Coating, Painting, and Lining for the Oil, Gas and Petrochemical Industries*. Ed. by Alireza Bahadori. Boston: Gulf Professional Publishing, 2015, pp. 107–156. DOI: 10.1016/B978-0-12-801407-3.00002-X.

[141] V. Sudarsan. "Chapter 4 - Materials for Hostile Chemical Environments". In: *Materials Under Extreme Conditions*. Ed. by A.K. Tyagi et al. Amsterdam: Elsevier, 2017, pp. 129–158. DOI: 10.1016/B978-0-12-801300-7.00004-8.

[142] Da Zhu et al. "Investigation of Electroless Nickel-Phosphorus Coating as an Alternative to Corrosion/Fouling Resistant Alloys in Downhole Service". In: *OTC Brasil*. OnePetro. 2017.

[143] S Duval et al. "Characterisation of organic coatings in sour media and influence of polymer structure on corrosion performance". In: *Progress in Organic Coatings* 39.1 (Aug. 2000), pp. 15–22. DOI: 10.1016/s0300-9440(00)00094-1.

[144] Pietro Pedeferri. "Corrosion Prevention by Coatings". In: *Corrosion Science and Engineering*. Springer International Publishing, 2018, pp. 327–361. DOI: 10.1007/978-3-319-97625-9_17.

[145] Paul Shewmon. "High Diffusivity Paths". In: *Diffusion in Solids*. Springer International Publishing, 2016, pp. 189–222. DOI: 10.1007/978-3-319-48206-4_6.

[146] James M Hill. "A random walk model for diffusion in the presence of high-diffusivity paths". In: *Advances in Molecular Relaxation and Interaction Processes* 19.4 (1981), pp. 261–284.

[147] Francis J. Norton. "Permeation of Gases through Solids". In: *Journal of Applied Physics* 28.1 (Jan. 1957), pp. 34–39. DOI: 10.1063/1.1722570.

[148] Mehrshad Moshref-javadi et al. "Diffusion behavior of hydrogen through thermally sprayed coating of 316L stainless steel". In: *International Journal of Hydrogen Energy* 42.9 (Mar. 2017), pp. 6409–6419. DOI: 10.1016/j.ijhydene.2016.11.026.

[149] Tomoyasu Tanaka et al. "Theory of Hydrogen Absorption in Metal Hydrides". In: *Electronic Structure and Properties of Hydrogen in Metals*. Springer US, 1983, pp. 79–84. DOI: 10.1007/978-1-4684-7630-9_10.

[150] Guiyang Wu et al. "The failure reason of epoxy-phenolic coating on the internal surface of BG90S steel tubing under sour gas environment". In: *Pigment & Resin Technology* ahead-of-print (Jan. 2020). DOI: 10.1108/PRT-08-2019-0069.

[151] H.S. Grewal et al. "Understanding Liquid Impingement erosion behaviour of nickel–alumina based thermal spray coatings". In: *Wear of Materials 2013* 301.1 (2013), pp. 424–433. DOI: 10.1016/j.wear.2013.01.063.

[152] "Drop impingement erosion of metals". In: *Proceedings of the Royal Society of London. A. Mathematical and Physical Sciences* 314.1519 (Jan. 1970), pp. 549–565. DOI: 10.1098/rspa.1970.0022.

[153] Boris Feliksovih Levin. *Effect of mechanical properties on erosion resistance of ductile materials*. Lehigh University, 1998.

[154] S. Hassani et al. "Predictive tools for the design of erosion resistant coatings". In: *Surface and Coatings Technology* 203.3-4 (Nov. 2008), pp. 204–210. DOI: 10.1016/j.surfcoat.2008.08.050.

[155] William T Becker et al. "ASM handbook". In: *Failure analysis and prevention* 11 (2002), p. 2166.

[156] Yüzüncü Yıl et al. "Wear and its Effects in Centrifugal Pumps". In: 29 (Sept. 2019), pp. 569–582. DOI: 10.29133/yyutbd.518139.

[157] K. Kishimoto et al. "8.07 - Case Studies of Electronic Packaging Failure". In: *Comprehensive Structural Integrity*. Ed. by I. Milne et al. Oxford: Pergamon, 2003, pp. 241–263. DOI: 10.1016/B0-08-043749-4/08046-0.

[158] E.M. Petrie. "Adhesive bonding of textiles: principles, types of adhesive and methods of use". In: *Joining Textiles*. Elsevier, 2013, pp. 225–274. DOI: 10.1533/9780857093967.2.225.

[159] M Dawood. "Durability of steel components strengthened with fiber-reinforced polymer (FRP) composites". In: *Rehabilitation of Metallic Civil Infrastructure Using Fiber Reinforced Polymer (FRP) Composites*. Elsevier, 2014, pp. 96–114.

[160] SpecialChem. "Adhesion in paints and coatings". In: *Adhesion in Paint and Coatings: Theories, Types and Test Methods* (). https://coatings.specialchem.com/coatings-properties/adhesion.

[161] Lutz-Michael Berger. "Application of hardmetals as thermal spray coatings". In: *International Journal of Refractory Metals and Hard Materials* 49 (2015). Special Issue: International Conference on the Science of Hard Materials – 10, pp. 350–364. DOI: https://doi.org/10.1016/j.ijrmhm.2014.09.029.

[162] V.M. Giese. "Adhäsive Kunststoff-Metall- und Kunststoff-Kunststoff-Verbindungen im Hinblick auf die Spritzgussverarbeitung". In: (1995). URL: https://books.google.nl/books?id=bH%5C_zMAAACAAJ.

[163] Olga Sedova et al. "The thermoelasticity problem for pressure vessels with protective coatings, operating under conditions of mechanochemical corrosion". In: *International Journal of Engineering Science* 170 (2022), p. 103589.

[164] S. A. Atashipour et al. "Elastic analysis of thick-walled pressurized spherical vessels coated with functionally graded materials". In: *Meccanica* 49.12 (Sept. 2014), pp. 2965–2978. DOI: 10.1007/s11012-014-0047-2.

[165] Zirui Zhao et al. "Improved thermal shock and corrosion resistance of -Al2O3/AlPO4 coating with PAA addition". In: *Surface and Coatings Technology* 414 (May 2021), p. 127115. DOI: 10.1016/j.surfcoat.2021.127115.

[166] Cheryl Pellerin et al. "Reflections on hexavalent chromium: health hazards of an industrial heavyweight." In: *Environmental health perspectives* 108.9 (2000), A402–A407.

[167] Mark A. Scharfenaker. "Chromium VI: a review of recent developments". In: *Journal - American Water Works Association* 93.11 (Nov. 2001), pp. 20–26. DOI: 10.1002/j.1551-8833.2001.tb09322.x.

[168] AH Roebuck et al. "Coating Economics". In: *Anti-Corrosion Methods and Materials* (1977).

[169] Peter M Schweizer. *Premetered Coating Methods: Attractiveness and Limitations*. Springer Nature, 2022, pp. 495–504. DOI: 10.1007/978-3-031-04180-8_1.

[170] M.P. Williams et al. *Decontamination and Cleaning Manual*. Shell Oil Company, 2006.

[171] John W Oldfield. *Electrochemical theory of galvanic corrosion*. ASTM International West Conshohocken, PA, 1988.

[172] XG Zhang. "Galvanic corrosion". In: *Uhlig's Corrosion Handbook* 51 (2011), pp. 123–130.

[173] Khlefa A Esaklul. "Hydrogen damage". In: *Trends in Oil and Gas Corrosion Research and Technologies* (2017), pp. 315–340.

[174] S. Khoma et al. "Influence of Hydrogen Sulfide on the Corrosion-Electrochemical Properties of 20 Steel with Coatings Based on Zinc and Aluminum". In: *Materials Science* 54.3 (Nov. 2018), pp. 438–443. DOI: 10.1007/s11003-018-0203-2.

[175] CV Franco et al. "Evaluation Of The Corrosion Resistance Of Thermal Sprayed Aluminium Coatings In Sulfidric Acid." In: *WIT Transactions on Engineering Sciences* 33 (2001).

[176] *Behavior of Thermal Spray Aluminum Coating in Wet H_2S Environments*. Vol. All Days. NACE CORROSION. Apr. 1999. eprint: https://onepetro.org/NACECORR/proceedings-pdf/CORR99/All-CORR99/NACE-99297/1916394/nace-99297.pdf.

[177] YL Chou et al. "The effect of molybdenum on the corrosion behaviour of the high-entropy alloys Co1. 5CrFeNi1. 5Ti0. 5Mox in aqueous environments". In: *Corrosion Science* 52.8 (2010), pp. 2571–2581.

[178] XH Zhao et al. "The experiment research of corrosion behaviour about Ni-based alloys in simulant solution containing H_2S/CO2". In: *Electrochimica Acta* 56.22 (2011), pp. 7725–7731.

[179] Yiyong Sui et al. "Stability of an Electrodeposited Nanocrystalline Ni-Based Alloy Coating in Oil and Gas Wells with the Coexistence of H_2S and CO2". In: *Materials* 10.6 (June 2017), p. 632. DOI: 10.3390/ma10060632.

[180] Jian-Bao Wang et al. "Microstructure and corrosion resistance to H_2S in the welded joints of X80 pipeline steel". In: *Metals* 9.12 (2019), p. 1325.

[181] M. Shah et al. "Comparative corrosion behaviour of austenitic 316L and duplex 2205 stainless steels: microstructure and property evolution at highly partial pressure of H_2S". In: *Corrosion Engineering, Science and Technology* 57.1 (2022), pp. 15–31. DOI: 10.1080/1478422X.2021.1980647.

[182] M.F.O. Schiefler et al. "Corrosion Behaviour of High Velocity Combustion Wire Sprayed Coatings". In: *International Thermal Spray Conference*. Ed. by C. C. Berndt et al. Verlag für Schweißen und verwandte Verfahren DVS-Verlag GmbH, Mar. 2002. DOI: 10.31399/asm.cp.itsc2002p0553.

[183] B.R. Marple et al. "Thermal spraying of nanostructured cermet coatings". In: *Journal of Materials Processing Technology* 117.3 (Nov. 2001), pp. 418–423. DOI: 10.1016/s0924-0136(01)00798-1.

[184] R. Schwetzke et al. "Microstructure and Properties of Tungsten Carbide Coatings Sprayed with Various High-Velocity Oxygen Fuel Spray Systems". In: *Jour-*

nal of Thermal Spray Technology 8.3 (Sept. 1999), pp. 433–439. DOI: 10.1361/105996399770350395.

[185] Robert J.K. Wood et al. "A critical review of the tribocorrosion of cemented and thermal sprayed tungsten carbide". In: *Tribology International* 119 (2018), pp. 491–509. DOI: 10.1016/j.triboint.2017.10.006.

[186] Zhen Li et al. "Cavitation erosion behavior of Hastelloy C-276 nickel-based alloy". In: *Journal of Alloys and Compounds* 619 (2015), pp. 754–759.

[187] ASTM International. "Test Methods for Determining Area Percentage Porosity in Thermal Sprayed Coatings". In: ASTM E2109-01 (2014). DOI: 10.1520/e2109-01r21.

[188] Koen Winters. "Measuring surface roughness of cross-sectional images with Python". In: (2023). DOI: 10.5281/ZENODO.8249891.

[189] M Anthony Xavior et al. "Experimental investigation of work hardening, residual stress and microstructure during machining Inconel 718". In: *Journal of Mechanical Science and Technology* 31 (2017), pp. 4789–4794.

[190] Zhaopeng Tong et al. "Microstructure, microhardness and residual stress of laser additive manufactured CoCrFeMnNi high-entropy alloy subjected to laser shock peening". In: *Journal of materials processing technology* 285 (2020), p. 116806.

[191] National Association of Corrosion Engineers. ""Standard Test Method – Evaluation of Pipeline and Pressure Vessel Steels for Resistance to Hydrogen Induced Cracking"". In: *NACE Standard TM0284-2016 Item No. 21215* (2016).

[192] D. Pérez Escobar et al. "Internal and surface damage of multiphase steels and pure iron after electrochemical hydrogen charging". In: *Corrosion Science* 53.10 (2011), pp. 3166–3176. DOI: https://doi.org/10.1016/j.corsci.2011.05.060.

[193] R. Grinon-Echaniz et al. "Study of cathodic reactions in defects of thermal spray aluminium coatings on steel in artificial seawater". In: *Corrosion Science* 187 (July 2021), p. 109514. DOI: 10.1016/j.corsci.2021.109514.

[194] Pravin Kumar et al. "Determination of hydrogen diffusivity in austenitic stainless steels by subscale microhardness profiling". In: *Journal of Alloys and Compounds* 255.1-2 (1997), pp. 130–134.

[195] Diana Maria Perez Escobar et al. "Hydrogen damage in multiphase steels after electrochemical charging". In: (2010), pp. 133–138.

[196] Virgínia Bertolo et al. "A comprehensive quantitative characterisation of the multiphase microstructure of a thick-section high strength steel". In: *Journal of Materials Science* 57.13 (Mar. 2022), pp. 7101–7126. DOI: 10.1007/s10853-022-07121-y.

[197] Davide Fantozzi et al. "Chlorine-induced high temperature corrosion of Inconel 625 sprayed coatings deposited with different thermal spray techniques". In: *Surface and Coatings Technology* 318 (2017), pp. 233–243.

[198] Monika Górnik et al. "The effect of spray distance on porosity, surface roughness and microhardness of WC-10Co-4Cr coatings deposited by HVOF". In: *Advances in Materials Science* 21.4 (2021), pp. 99–111.

[199] JM Guilemany et al. "Effects of thickness coating on the electrochemical behaviour of thermal spray Cr3C2–NiCr coatings". In: *Surface and coatings technology* 153.2-3 (2002), pp. 107–113.

[200] SJ Choi et al. "Corrosion behavior in a 3.5 wt% NaCl solution of amorphous coatings prepared through plasma-spray and cold-spray coating processes". In: *Metals and Materials International* 20 (2014), pp. 1053–1057.

[201] Jinran Lin et al. "Microstructure and cavitation erosion behavior of FeNiCrBSiNbW coating prepared by twin wires arc spraying process". In: *Surface and Coatings Technology* 240 (2014), pp. 432–436.

[202] Granta Design. *CES EduPack*. https://www.grantadesign.com/products/edupack/. 2023.

[203] W. Luo et al. "Effect of Residual Stress on the Wear Resistance of Thermal Spray Coatings". In: *Journal of Thermal Spray Technology* 25.1-2 (Sept. 2015), pp. 321–330. DOI: 10.1007/s11666-015-0309-0.

[204] Katsuji Tosha. "Influence of residual stresses on the hardness number in the affected layer produced by shot peening". In: *Asia-Pacific Forum on Precision Surface Finishing and Deburring Technology*. 2002, pp. 48–54.

[205] Pierre L. Fauchais et al. "Industrial Applications of Thermal Spraying Technology". In: *Thermal Spray Fundamentals: From Powder to Part*. Boston, MA: Springer US, 2014, pp. 1401–1566. DOI: 10.1007/978-0-387-68991-3_18.

[206] S. Takeuchi et al. "Modelling of residual stress in plasma-sprayed coatings: Effect of substrate temperature". In: *Surface and Coatings Technology* 43-44 (Dec. 1990), pp. 426–435. DOI: 10.1016/0257-8972(90)90094-s.

[207] Tina Ghara et al. "Effect of Grit Blasting Parameters on Surface and Near-Surface Properties of Different Metal Alloys". In: *Journal of Thermal Spray Technology* 30.1-2 (Nov. 2020), pp. 251–269. DOI: 10.1007/s11666-020-01127-1.

[208] William Heilman et al. "Permeability of polymer films to hydrogen sulfide gas". In: *Industrial & Engineering Chemistry* 48.4 (1956), pp. 821–824.

[209] Mingtao Wang et al. "Understanding the passivation behavior and film chemistry of four corrosion-resistant alloys in the simulated flue gas condensates". In: *Materials Today Communications* 31 (2022), p. 103567.

[210] Amy C Lloyd et al. "Cr, Mo and W alloying additions in Ni and their effect on passivity". In: *Electrochimica Acta* 49.17-18 (July 2004), pp. 3015–3027. DOI: 10.1016/j.electacta.2004.01.061.

[211] RJ Coyle et al. "The effect of aging on hydrogen embrittlement of a nickel alloy". In: *Metallurgical Transactions A* 12 (1981), pp. 653–658.

[212] Ellina Lunarska-Borowiecka et al. "Hydride formation in a Ni-base superalloy". In: *Metallurgical Transactions A* 12.1 (Jan. 1981), pp. 101–107. DOI: 10.1007/bf02648514.

[213] B. J. Berkowitz et al. "The effect of ordering on the hydrogen embrittlement susceptibility of Ni2Cr". In: *Metallurgical Transactions A* 11.11 (Nov. 1980), pp. 1877–1881. DOI: 10.1007/bf02655104.

[214] Mehrshad Moshref-Javadi et al. "Evaluation of hydrogen permeation through standalone thermally sprayed coatings of AISI 316L stainless steel". In: *International Journal of Hydrogen Energy* 43.9 (Mar. 2018), pp. 4657–4670. DOI: 10.1016/j.ijhydene.2018.01.021.

[215] ZAHRA S Hosseini et al. "Trapping against hydrogen embrittlement". In: *Proceedings of the 2016 International Hydrogen Conference: Materials Performance in Hydrogen Environments, ASME Press, New York, NY*. 2017, pp. 71–80.

[216] M. Dadfarnia et al. "Hydrogen interaction with multiple traps: Can it be used to mitigate embrittlement?" In: *International Journal of Hydrogen Energy* 36.16 (Aug. 2011), pp. 10141–10148. DOI: 10.1016/j.ijhydene.2011.05.027.

[217] Zhen Wang et al. "Hydrogen Diffusion and Its Effect on Hydrogen Embrittlement in DP Steels With Different Martensite Content". In: *Frontiers in Materials* 7 (Dec. 2020). DOI: 10.3389/fmats.2020.620000.

[218] A Iost et al. "Hardness variation in a cathodic hydrogen-charged austenitic stainless steel". In: *Scripta materialia* 37.10 (1997).

[219] R Rachidi et al. "Effectiveness of phased array focused ultrasound and active infrared thermography methods as a nondestructive testing of Ni-WC coating adhesion". In: *Nondestructive Testing and Evaluation* 34.2 (2019), pp. 205–220. DOI: 10.1080/10589759.2019.1566905.

[220] Xia Liu et al. "Improvement in High-Velocity Air-Fuel-Sprayed Cr3C2-NiCr/(NiAl, NiCr) Composite Coatings by Annealing Heat Treatment". In: *Journal of Materials Engineering and Performance* 32.1 (Nov. 2022), pp. 199–210. DOI: 10.1007/s11665-022-06938-7.

[221] ASTM International. "ASTM G75-03(2020)". In: (2020). Accessed: 2023-09-15. URL: https://www.astm.org/Standards/G75.htm.

[222] International Organization for Standardization (ISO). "ISO 148-1:2016". In: (2016). Accessed: 2023-09-15. URL: https://www.iso.org/standard/65704.html.

A

Schematic diagram of HIC mechanism

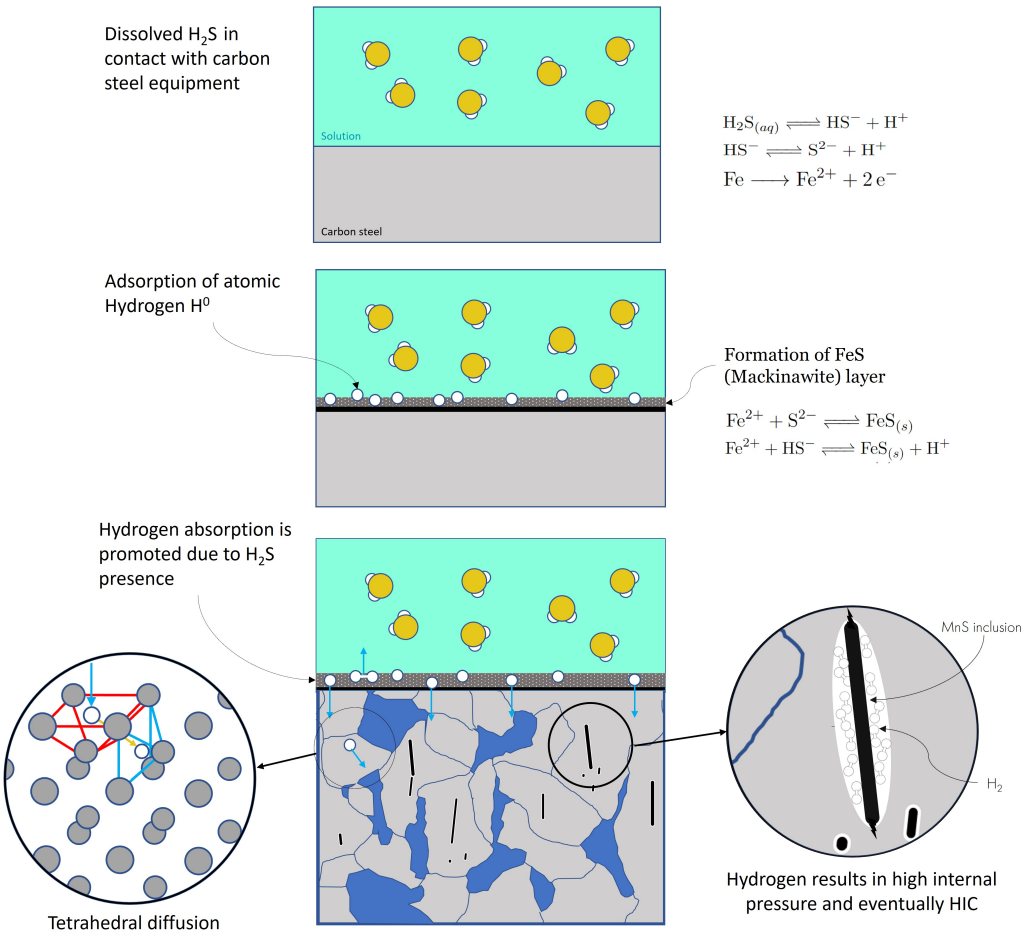

B

Material certificate S235JR

NLMK Clabecq

TO WHOM IT MAY CONCERN

Clabecq, 22/11/22

Declaration of Performance
Construction Product - EC Regulation N°305/2011

DoP - No. 20221122-00006

1. Unique identification code of the product-type: S235 JR+AR
2. Type, batch or serial number or any other element allowing identification of the construction product as required pursuant to Article 11(4): UST10273
3. Intended use or uses of the construction product, in accordance with the applicable harmonized technical specification, as foreseen by the manufacturer: **construction**
4. Name, registered trade name or registered trade mark and contact address of the manufacturer as required pursuant to Article 11(5): **NLMK Clabecq SA, 101 rue de Clabecq 1460 ITTRE (Belgium)**
5. Where applicable, name and contact address of the authorized representative whose mandate covers the tasks specified in Article 12(2): Not applicable
6. System or systems of assessment and verification of constancy of performance of the construction product as set out in Annex V: System 2+
7. In case of the declaration of performance concerning a construction product covered by a harmonised standard:
   AFNOR Certification S.A.S.U. - Identification number 0333 - performed:
   (i) initial inspection of the manufacturing plant and of factory production control;
   (ii) continuous surveillance, assessment and evaluation of factory production control. under system 2+ and issued the certificate of constancy of performance, certificate of conformity of the factory production control, test/calculation reports according to harmonized European Norm EN 10025
8. Not applicable
9. Declared performance
   See attached Material Test Certificate N°: 03693
10. The performance of the product identified in points 1 and 2 is in conformity with the declared performance in point 9.
    This declaration of performance is issued under the sole responsibility of the manufacturer identified in point 4.
    Signed electronically for and on behalf of the manufacturer by:
    Mr. Philippe HERNAUT Quality and Metallurgy Manager

afaq ISO 9001

NLMK CLABECQ
Rue de Clabecq 101
1460 ITTRE (BELGIUM)

INSPECTION CERTIFICATE 3.2 by LLOYD'S REGISTER MARITIEM BELGIE BV as per EN 10204 (2004)

N°3692 — N°PAGE 1/1 — BLATT NR — PAGE No

PLAQUES-BLECHE-PLATES

SIGLE PRODUCTEUR — HERSTELLERZEICHEN — TRADE MARK: NO

(E.L) : Etat de Livraison - (L)ieferzustand - (S.D) State of Delivery
AR : As Rolled

Poinçon organisme et / ou service de contrôle — Stempel des Abnahmebeauftragten — Stamp of the Inspection representative

CLIENT / DESTINATAIRE - BESTELLESR / EMPFANGER - CUSTOMER / CONSIGNEE
DE JONG & LAVINO BV
DEILSEWEG 13
NL-4191 NX NX GELDERMALSEN

N°COMMANDE COURTIER/CLIENT - MAKLER/KUNDENBESTEL LNUMMER — BROKER/PURCHASER'S ORDER NUMBER
21-1873 from 13.10.22
21-1873

N°Commande usine — Werks Nr. — Works order No
10273

NUANCE ET SPECIFICATIONS TECHNIQUES / PRUF-UND WERKSTOFFGRUNDLAGEN / QUALITY AND SPECIFICATIONS
'GRADE A
LLOYD'S REGISTER CHAP.3 SCT.2/07-2022

APPROVED MATERIALS QUALITY SCHEME

C03692_2_10273_51002680.CRPDF

IDENTIFICATION DU PRODUIT — ERZEUGNIS BENENNUNG – PRODUCT ID				DIMENSIONS – ABMESSUNGEN – DIMENSIONS					TRACTION – ZUGVERSUCH – TENSILE TEST					RESILIENCE – KERBSCHLAGZÄHIGKEIT – IMPACT TEST					
No Référence / Referenz. Nr / Reference No	No Coulée / Schmelze Nr / Heat No	Brame / Bramme / Slab	N°Pst / Post Nr / Item Nr	Nbre de Plaques / Stückzahl / Nbr of pieces	Epaisseur / Dicke / Thickness (mm)	Largeur / Breite / Width (mm)	Longueur / Lange / Length (mm)	Masse Théorique / Theoretische Masse / Theoretical Mass (Kg)	(E.L) (L) (S.D)	Place (2)	Sens / Rtr (3)	REH / YS (MPa)	Rm / Ts (MPa)	A%(1) / E%(1)	Temp °C	T.S.L (3)	Valeurs Individuelles / Einzelwerte / Individual Values (Joules)		Moy / Mitw / Avrg
3093	834604 D1		6	2	10.00	2500	12000	4710	AR	3	T	300	465	32.7*	20	VL7	149	145	143	146
	834604 E1		6	3	10.00	2500	12000	7065	AR										
				5				11775											
3100	834817	E3	5	3	10.00	2500	10000	5889	AR	3	T	305	470	33.4*	20	VL7	169	173	170	171
3100	834818	E3	5	3	10.00	2500	10000	5889	AR	3	T	305	470	33.4*	20	VL7	169	173	170	171
3095	834847	C1	6	3	10.00	2500	12000	7065	AR	3	T	324	479	30.4*	20	VL7	163	160	169	164
				14				30618											

ANALYSE COULEE - SCHMELZEANALYSE - HEAT ANALYSIS
(*) = ANALYSE PRODUIT - STUCKANALYSE - PRODUCT ANALYSIS
(1) (*) Lo = 5,65 VS mm – (#) Lo = 50 mm – (+) Lo = 200 mm

(5)	No COULEE SCHMELZE Nr HEAT No	Mn %	P%	S%	C%	Si%	Al%	Cu%	Nb%	Ni%	Cr%	V%	Mo%	Ti%	N%	Ceq
# CC	834604	1.082	0.008	0.006	0.152	0.176	0.043	0.031	0.002	0.020	0.034	0.001	0.002	0.001	0.0040	0.343
# CC	834817	1.088	0.007	0.001	0.150	0.193	0.041	0.036	0.003	0.013	0.020	0.001	0.001	0.001	0.0033	0.339
# CC	834818	1.088	0.007	0.001	0.150	0.193	0.041	0.036	0.003	0.013	0.020	0.001	0.001	0.001	0.0033	0.339
# CC	834847	1.095	0.011	0.003	0.155	0.190	0.046	0.034	0.003	0.019	0.027	0.001	0.001	0.001	0.0035	0.347

Surface control as per EN 10163-2, CL. B (S.-CL.3)
Fully killed and fine grain practice

N° article client – Artikel Nr des Kunden – Customer article No
P 6:21-1873
P 5:21-1873

This certificate is issued under the arrangements authorised by Lloyd's Register in accordance with the requirements of the Materials Quality Scheme and certificate number MQS 016.

Contrôle de marquage d'aspect et de dimensions : Satisfaisants
Kennzeichnung, Besichtigung und Ausmessung : Ohne Beanstandung
Marking, inspection and measurement : Without objection

LR A S235 JR+AR
EN 10029/2010 CL. B / N (L)

ITTRE le 22/11/22
FAIENZA Savino
Certificate editor

(3) Type : V : ISO V (KV8) ; N : ASTM Charpy V (KCV)
Sens : L : Long – Längs – Length T : Travers – Quer – Transverse
Localisation : 1 : Peau – Oberfläche – Rolled surface (10*10 mm)
2 : 1/2 Epaisseur – 1/2 Dicke – 1/2 Thickness (10*10 mm)
4 : 1/4 Epaisseur – 1/4 Dicke – 1/4 Thickness (10*10 mm)
6 : 5*10 mm 7 : 7,5*10 mm 8 : 6,7*10 mm

(2) Location – Probelage T : Tete – Kopf - Top
2 : Milieu – Mitte – Middle
3 : Pied – Fuss – Bottom
Impact test machines max. energy
ISO 148 : 450J
ASTM/ASME A/SA 370: 750J

(5) # : Oxygène pur – Sauerstoff – Oxygen + : EAF
CC : Coulée continue - Kontinuierliches Giesson
Continuous casting

Nous certifions que les produits énumérés ci-dessus sont conformes aux prescriptions de la commande.
Wir bestätigen hiermit, dass die obengenannten Erzeugnisse den Bestellungsvorschriften entsprechen.
We certify hereby that the above mentioned products are consistent with the order prescriptions.

150667

NLMK CLABECQ
Rue de Clabecq 101
1460 ITTRE (BELGIUM)

INSPECTION CERTIFICATE 3.1 as per EN 10204 (2004)

N°3693 — N°PAGE 1/1 / BLATT NR / PAGE No

PLAQUES-BLECHE-PLATES

22-0333-CPR-138001 0086-CPR-757321

SIGLE PRODUCTEUR / HERSTELLERZEICHEN / TRADE MARK

(E.L) : Etat de Livraison - (L)ieferzustand - (S.D) State of Delivery
AR : As Rolled

Poinçon organisme et / ou service de contrôle / Stempel des Abnahmebeauftragten / Stamp of the Inspection representative

CLIENT / DESTINATAIRE - BESTELLESR / EMPFANGER - CUSTOMER - CONSIGNEE

DE JONG & LAVINO BV
DEILSEWEG 13
NL-4191 NX NX GELDERMALSEN

N°COMMANDE COURTIER/CLIENT - MAKLER/KUNDENBESTEL LNUMMER - BROKER/PURCHASER'S ORDER NUMBER

21-1873 from 13.10.22
21-1873

N°Commande usine / Werks Nr. / Works order No

10273

NUANCE ET SPECIFICATIONS TECHNIQUES / PRÜF-UND WERKSTOFFGRUNDLAGEN / QUALITY AND SPECIFICATIONS

'S235 JR + AR
EN 10025-2 /19

IDENTIFICATION DU PRODUIT / ERZEUGNIS BENENNUNG – PRODUCT ID				DIMENSIONS – ABMESSUNGEN – DIMENSIONS						TRACTION – ZUGVERSUCH – TENSILE TEST					RESILIENCE – KERBSCHLAGZÄHIGKEIT – IMPACT TEST					
No Référence / Referenz. Nr / Reference No	No Coulée / Schmelze Nr / Heat No	Brame / Bramme / Slab	N°Pst / Post Nr / Item Nr	Nbre de Plaques / Stückzahl / Nbr of pieces	Epaisseur / Dicke / Thickness	Largeur / Breite / Width	Longueur / Lange / Length	Masse Théorique / Theoretische Masse / Theoretical Mass	(E.L) / (L) / (S.D)	Place (2)	Sens Dir (3)	REH / YS	Rm / Ts	A%(1) / E%(1)	Temp °C	T.S.L (3)	Valeurs Individuelles / Einzelwerte / Individual Values			Moy / Mitw / Avrg
					(m m)	(m m)	(m m)	(K g)				(MPa)	(MPa)				(Joules)			
3093	834604 D1		6	2	10.00	2500	12000	4710	AR	3	T	300	465	32.7*	20	VL7	149	145	143	146
	834604 E1		6	3	10.00	2500	12000	7065	AR											
				5				11775												
3100	834817 E3		5	3	10.00	2500	10000	5889	AR	3	T	305	470	33.4*	20	VL7	169	173	170	171
3100	834818 E3		5	3	10.00	2500	10000	5889	AR	3	T	305	470	33.4*	20	VL7	169	173	170	171
3095	834847 C1		6	3	10.00	2500	12000	7065	AR	3	T	324	479	30.4*	20	VL7	163	160	169	164
				14				30618												

ANALYSE COULEE - SCHMELZEANALYSE - HEAT ANALYSIS
(*) = ANALYSE PRODUIT - STUCKANALYSE - PRODUCT ANALYSIS
(1) (*) Lo = 5,65 VS mm – (#) Lo = 50 mm – (+) Lo = 200 mm

(5)	No COULEE / SCHMELZE Nr / HEAT No	Mn %	P%	S%	C%	Si%	Al%	Cu%	Nb%	Ni%	Cr%	V%	Mo%	Ti%	N%	Ceq
# CC	834604	1.082	0.008	0.006	0.152	0.176	0.043	0.031	0.002	0.020	0.034	0.001	0.002	0.001	0.0040	0.343
# CC	834817	1.088	0.007	0.001	0.150	0.193	0.041	0.036	0.003	0.013	0.020	0.001	0.001	0.001	0.0033	0.339
# CC	834818	1.088	0.007	0.001	0.150	0.193	0.041	0.036	0.003	0.013	0.020	0.001	0.001	0.001	0.0033	0.339
# CC	834847	1.095	0.011	0.003	0.155	0.190	0.046	0.034	0.003	0.019	0.027	0.001	0.001	0.001	0.0035	0.347

Surface control as per EN 10163-2, CL. B (S.-CL.3)
Fully killed and fine grain practice

N°article client – Artikel Nr des Kunden – Customer article No
P 6:21-1873
P 5:21-1873

Contrôle de marquage d'aspect et de dimensions : Satisfaisants
Kennzeichnung, Besichtigung und Ausmessung : Ohne Beanstandung
Marking, inspection and measurement : Without objection

LR A S235 JR+AR
EN 10029/2010 CL. B / N (L)

ITTRE le 22/11/22
FAIENZA Savino
Certificate editor

(3) Type : V : ISO V (KV8) ; N : ASTM Charpy V (KCV)
Sens : L : Long – Längs – Length T : Travers – Quer – Transverse
Localisation : 1 : Peau – Oberfläche – Rolled surface (10*10 mm)
2 : 1/2 Epaisseur – 1/2 Dicke – 1/2 Thickness (10*10 mm)
4 : 1/4 Epaisseur – 1/4 Dicke – 1/4 Thickness (10*10 mm)
6 : 5*10 mm 7 : 7.5*10 mm 8 : 6.7*10 mm

(2) Location – Probelage 1 : Tête – Kopf - Top
2 : Milieu – Mitte – Middle
3 : Pied – Fuss – Bottom
Impact test machines max. energy
ISO 148 : 450J
ASTM/ASME A/SA 370: 750J

(5) # : Oxygène pur – Sauerstoff – Oxygen + : EAF
CC : Coulée continue - Kontinuierliches Giessen
Continuous casting

Nous certifions que les produits énumérés ci-dessus sont conformes aux prescriptions de la commande.
Wir bestätigen hiermit, dass die obengenannten Erzeugnisse den Bestellungsvorschriften entsprechen.
We certify hereby that the above mentioned products are consistent with the order prescriptions.

C

Element immersion report

Item list

Item list	
Sample nr:.	Shell description
1	HIC-250µm
2	HIC-375µm
3	HIC-500µm
4	GV-250µm
5	GV-375µm
6	GV-500µm
7	S235-Ref

HIC TEST ACC. TO NACE TM0284-2016 / EN 10229-1998

Test conditions			
Solution type	NACE TM0284 solution A	*Test duration (hr)*	241
Initial pH	2.73	*Temperature (°C)*	24.4
pH at start of test	2.87	*[H2S] at start of test (mg/L)*	2939
pH at end of test	3.63	*[H2S] at end of test (mg/L)*	2777
Oxygen	<5 ppb		

Samples during exposition

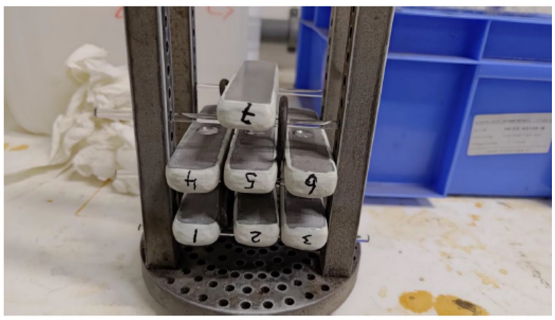

Samples before exposition

D

Defect overview

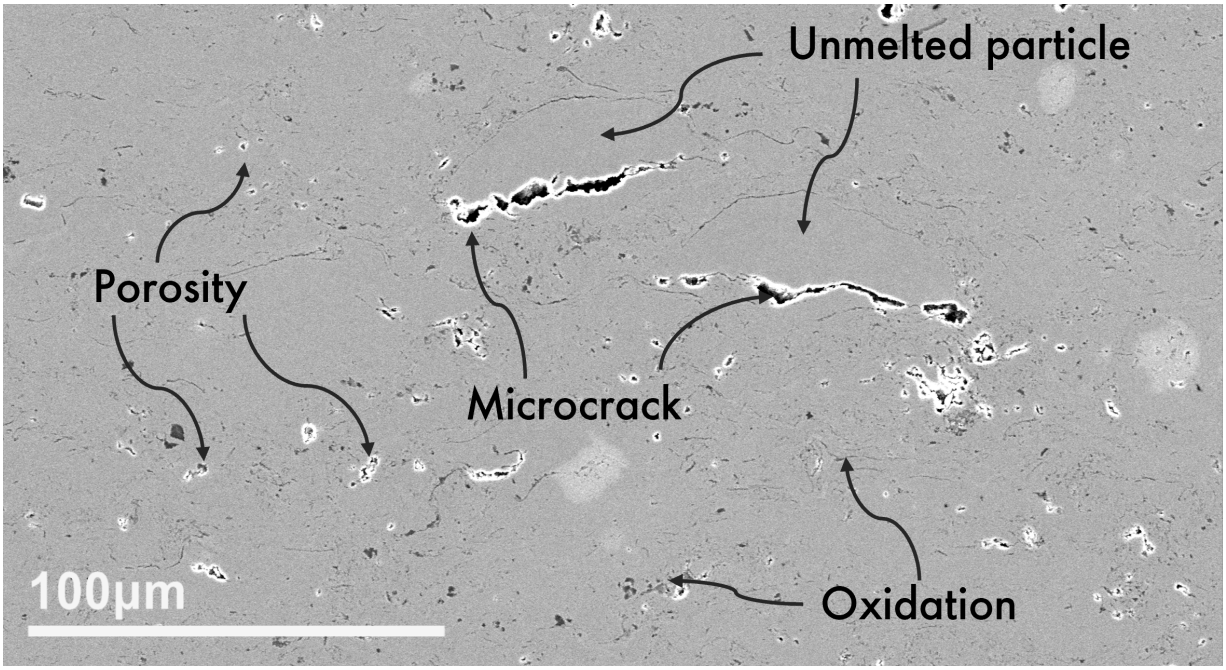

Stitched microscopy images

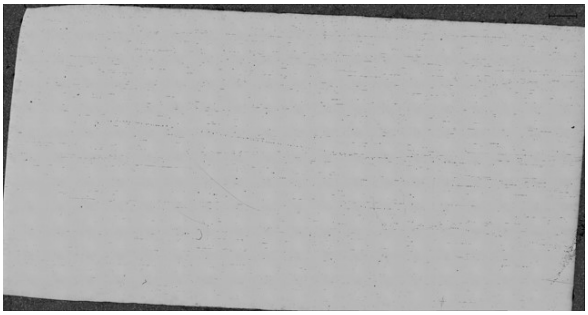

Figure D.1: Stitched micrograph of unimmersed sample without coating

Figure D.2: Stitched micrograph of immersed sample without coating

Figure D.3: Stitched micrograph of immersed sample without coating

Figure D.4: Stitched micrograph of immersed sample without coating

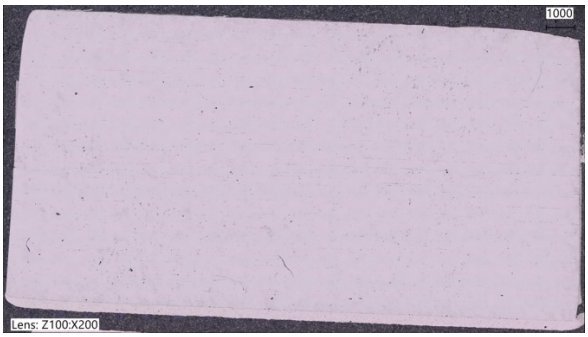

Figure D.5: Stitched micrograph of unimmersed sample with 250 µm coating

Figure D.6: Stitched micrograph of immersed sample with 250 µm coating

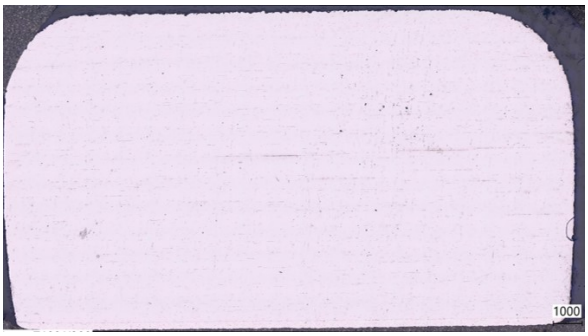

Figure D.7: Stitched micrograph of immersed sample with 250 µm coating

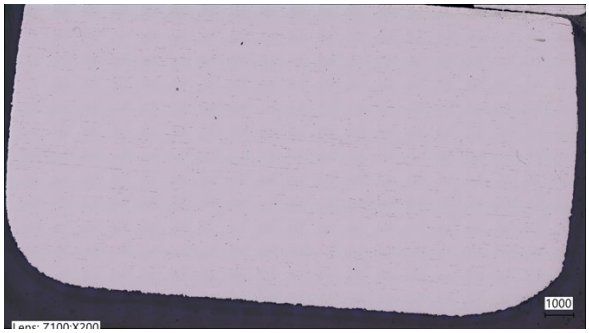

Figure D.8: Stitched micrograph of immersed sample with 250 µm coating

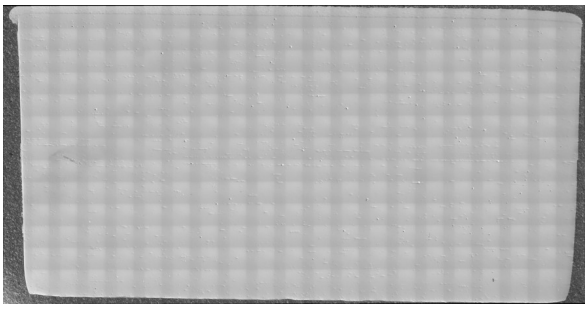

Figure D.9: Stitched micrograph of unimmersed sample with 375 µm coating

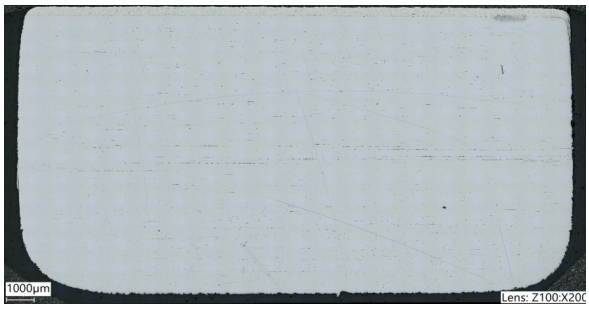

Figure D.10: Stitched micrograph of immersed sample with 375 µm coating

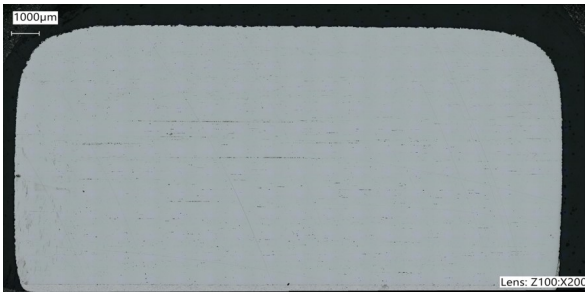

Figure D.11: Stitched micrograph of immersed sample with 375 µm coating

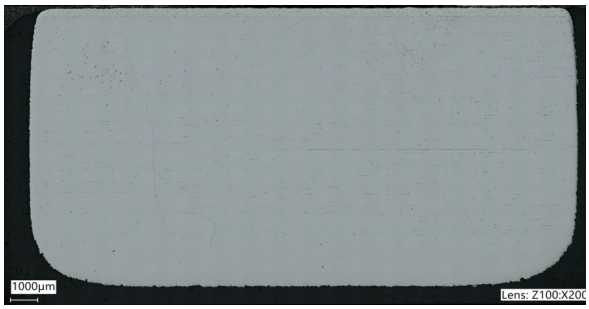

Figure D.12: Stitched micrograph of immersed sample with 375 µm coating

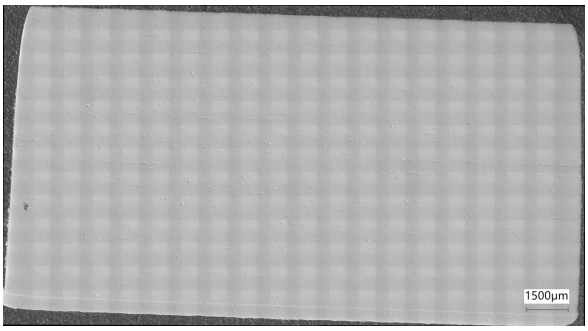

Figure D.13: Stitched micrograph of unimmersed sample with 500 µm coating

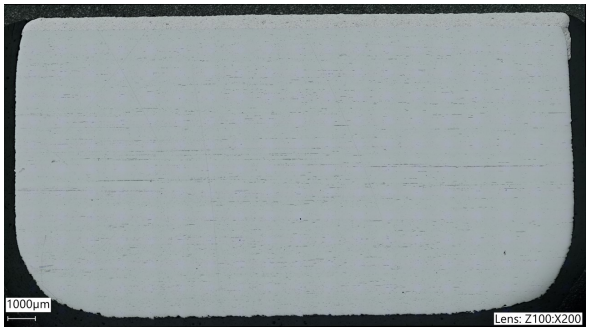

Figure D.14: Stitched micrograph of immersed sample with 500 µm coating

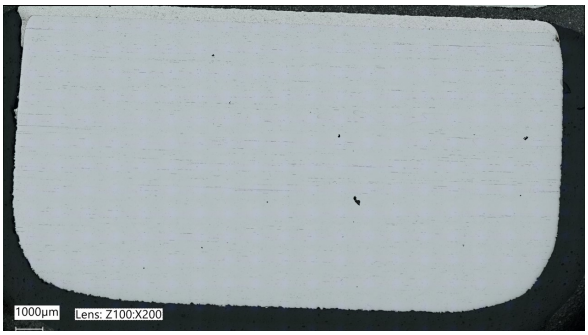

Figure D.15: Stitched micrograph of immersed sample with 500 µm coating

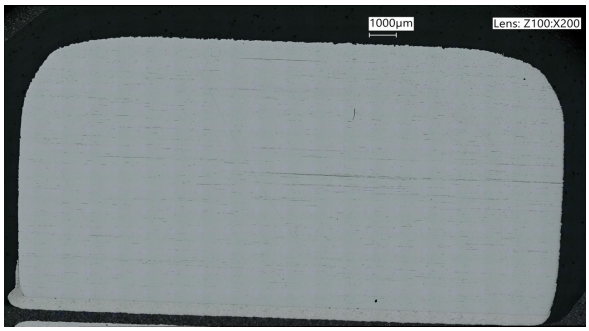

Figure D.16: Stitched micrograph of immersed sample with 500 µm coating